GL01190

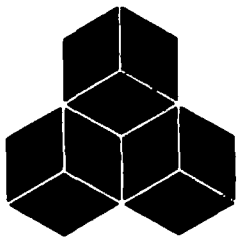

SYSTEMS, SCIENCE AND SOFTWARE

SSS-R-78-3639

GEOPRESSURED GEOTHERMAL RESERVOIR AND WELLBORE SIMULATION

S. K. GARG
J. W. PRITCHETT
D. H. BROWNELL, JR.
T. D. RINEY

FINAL REPORT (YEAR 2)

WORK PERFORMED FOR THE
UNIVERSITY OF TEXAS AT AUSTIN
UNDER
U.S. DEPARTMENT OF ENERGY
CONTRACT EY-76-C-5040-1S

MAY 1978

P.O. BOX 1620, LA JOLLA, CALIFORNIA 92038 TELEPHONE (714) 453-0060

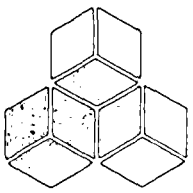

SYSTEMS, SCIENCE AND SOFTWARE

SSS-R-78-3639

GEOPRESSURED GEOTHERMAL RESERVOIR AND WELLBORE SIMULATION

S. K. GARG
J. W. PRITCHETT
D. H. BROWNELL, JR.
T. D. RINEY

FINAL REPORT (YEAR 2)

WORK PERFORMED FOR THE
UNIVERSITY OF TEXAS AT AUSTIN
UNDER
U.S. DEPARTMENT OF ENERGY
CONTRACT EY-76-C-5040-1S

MAY 1978

P. O. BOX 1620, LA JOLLA, CALIFORNIA 92038, TELEPHONE (714) 453-0060
3398 CARMEL MOUNTAIN ROAD, SAN DIEGO, CALIFORNIA 92121

TABLE OF CONTENTS

FOREWORD

This report describes work performed by Systems, Science and Software (S^3) in support of the parallel reservoir modeling activities by the University of Texas at Austin (UTA). It represents the final technical report for Year 2 of this joint effort to develop and apply techniques for predicting the performance of geopressured geothermal reservoir systems. Close liaison was maintained between the UTA and S^3 teams to ensure that the work performed at the two locations was complementary and consistent. The research effort was performed for the Division of Geothermal Energy of the U. S. Department of Energy (DOE) under Contract EY-76-C-5040-1S. Mr. Keith Westhuesing was the cognizant DOE Program Manager for the work reported here. Dr. Roy M. Knapp of UTA was the overall Principal Investigator for the contract. Dr. Sabodh K. Garg led the S^3 subcontract work reported herein.

ABSTRACT

During Year 1 of this effort, a rather general and flexible computer program (MUSHRM) was developed for simulating the transport of two-phase fluid (water with dissolved methane/methane gas) and heat in a geopressured geothermal reservoir. Mass sources or sinks in the corresponding finite-difference blocks of MUSHRM may be prescribed to represent the effects of production and injection wells, respectively, which are perforated within the volume of space represented by the block. A substantial part of the effort during Year 2 was concerned with the development of computational techniques for treating local two-phase flow within a well-block to obtain sandface conditions at well-bottom, and for treating two-phase flow in the wellbore to obtain well-head conditions. Coupled reservoir/wellbore calculations are presented to illustrate the effects on production of reservoir permeability and compressibility, well-bottom depth and fluid pressure, reservoir temperature, and dissolved methane content of the reservoir fluids. A series of calculations simulating well pumping tests are presented to determine the effects of formation compaction (and associated reduction of absolute permeability) and methane saturation; it is shown that conventional well test analysis should yield reliable permeability data even when compaction occurs and methane evolves out of solution, but storativity estimates will be unreliable. Preliminary calculations are presented for production behavior of the Brazoria County, Texas prospect to variations in shale distribution, compressibility and permeability; potential land surface movement is also computed.

I. INTRODUCTION AND BACKGROUND

The goal of this work is to develop the computer simulation techniques which, when backed by adequate field information (geologic, geophysical, well test and fluid flow data) for a given geopressured geothermal reservoir system, can be used to estimate its probable size, deliverability, lifetime and other long-term performance characteristics in advance of large scale commitment. The simulation techniques are to be applied to a specific geothermal system, selected by the contractor (University of Texas at Austin) and the Department of Energy, in order to assist in the interpretation of the data from exploratory wells and assess the potential long-term performance of the system under alternate exploitation strategies. Computer techniques have been developed for modeling the transport of liquid water/methane mixtures within a three-dimensional heterogeneous reservoir, calculation of sand-face pressure/enthalpy values from the corresponding well-block variables, and flow of water/methane mixtures within wellbores. Since no fluid flow information for a geopressured geothermal field is yet available, however, the simulation capabilities to date have been used for parametric studies of hypothetical systems.

The project has been underway since February 1, 1976. The work accomplished during the first year was reported earlier [Garg, et al., 1977]. The work accomplished in the second year is documented in this report.

1.1 PREVIOUS WORK (YEAR 1)

During the first year, the following was accomplished:

1. Developed the basic theoretical formulations for the important thermomechanical processes operative in a geopressured geothermal reservoir.

2. Designed and developed a rather general and flexible geopressured geothermal reservoir simulator based on the theoretical formulation.

3. Developed comprehensive constitutive packages for water/methane mixtures and fluid saturated rocks and incorporated them into the reservoir simulator.

4. Applied the reservoir simulator to examine the sensitivity of the performance of a representative geopressured geothermal system to variations in the parameters governing formation compaction, thermal interactions during reinjection, methane saturation and relative permeability.

Basically, a rather general reservoir simulator for treating the important mechanisms in geopressured geothermal reservoir systems was developed and used for preliminary reservoir response calculations. The work performed in Year 1 was documented in a detailed final report [Garg, et al., 1977]. The principal results of the first year were also presented at technical meetings and published in conference proceedings (Pritchett, et al. [1977]; Garg and Pritchett [1977a]; Knapp, et al. [1977]).

1.2 WORK ACCOMPLISHED IN YEAR 2

This report describes the work performed during the second year. The following tasks were accomplished:

1. Developed a model for the two-phase (free methane gas and liquid water with dissolved methane) flow of water/methane mixtures within a wellbore.

2. Coupled the wellbore model with a simplified model for single-phase (water with dissolved methane) radial flow in a geopressured geothermal

aquifer. The coupled model was used in a series of calculations to illustrate the effects on production of reservoir permeability and compressibility, well-bottom depth and fluid pressure, reservoir temperature, and dissolved methane content of the reservoir fluids.

3. Developed mathematical techniques for treating local radial two-phase flow within a computational zone of the reservoir simulator when a wellbore is completed within that zone. The mathematical model is required to compute the sandface conditions from the grid-block values given by the reservoir simulator.

4. Performed a series of calculations simulating well pumping tests to assess the effects of formation compaction (and the associated reduction of absolute permeability) and methane saturation. It was found that conventional well test analysis may be expected to yield reliable formation permeability data even when compaction occurs and methane evolves out of solution, but storativity estimates will be unreliable. Drawdown and buildup test data together can be used to diagnose irreversible compaction characteristics of the formation.

5. Performed axisymmetric calculations to make a preliminary investigation of the production behavior of the Brazoria County, Texas prospect (Zone E) to variations in shale distribution, compressibility and permeability. The land surface movement, both vertical (subsidence) and horizontal, associated with fluid production has also been computed. It should be emphasized here that all of these preliminary Brazoria County calculations are, of necessity,

based on conjectured reservoir properties (results from the General Crude/DOE 1 Martin Ranch well will not be available until late summer of 1978).

It is appropriate to briefly describe here the contents of the rest of this technical report. The wellbore model coupled with a simplified model for single-phase radial flow in a geopressured geothermal aquifer is described in Section II; this work has been presented at a technical meeting and will be published as a journal article [Garg and Pritchett, 1977b]. Section III presents the calculations simulating well pumping tests; we also briefly discuss here the relationship between the calculated well-block pressures and the actual flowing pressures due to a well in the grid block. The mathematical model for treating local radial two-phase flow in the well-block is described in Section IV. Preliminary calculations for the Brazoria County (Texas) prospect are discussed in Section V. Finally, future plans are outlined in Section VI.

II. TWO-PHASE FLOW IN GEOPRESSURED GEOTHERMAL WELLS

2.1 INTRODUCTION

An ability to predict both the quantity of fluid that can be produced and its thermodynamic state (pressure, temperature, enthalpy, methane mass fraction, etc.) is essential in order to estimate the total usable energy of a geopressured geothermal resource. Computer models or analytical techniques can be utilized to calculate the thermodynamic state of the fluid at the well bottom (i.e., the depth at which the fluid enters the wellbore from the reservoir); a wellbore simulator is required to compute the well-head fluid properties from a given well-bottom state.

The reservoir mechanics of a geopressured system have previously been discussed by Pritchett, et al., [1977] and by Garg, et al. [1977]. There are four driving mechanisms which tend to expel fluid from a geopressured stratum (water compressibility, pore collapse, evolution of methane gas, and clay dehydration or shale dewatering), and two which tend to impede fluid flow (decrease in permeability which accompanies pore collapse; relative permeability effect due to evolution of gas). Garg, et al., [1977] and Knapp, et al., [1977] describe two and three-dimensional multiphase (liquid water with dissolved methane ⇄ methane gas) computer programs for solving the system of equations which govern mass and heat flow in a geopressured geothermal reservoir; these computer models include the effects of all the major reservoir drive mechanisms. While computer models are essential for detailed simulations of geopressured reservoirs, simple analytical models may be sufficient for treating certain practical problems (e.g., well testing). In this section, fluid flow in the aquifer is treated using single-phase (liquid water with dissolved methane) unsteady radial Darcian flow; no evolution of free methane is allowed in the pores of the reservoir rock and the two-phase

regime (if any) is assumed to occur only in the cased part of the production hole. Other assumptions invoked in the analysis are (1) constant permeability (no change in permeability due to pore collapse), (2) constant rock compressibility (no nonlinear behavior), (3) constant fluid compressibility and (4) isothermal fluid flow (no change in the temperature of the reservoir fluids due to production). It is clear that these assumptions seriously restrict the applicability of the model (see Garg, et al. [1977] for a detailed discussion of this question); nevertheless, the model is quite useful in studying the production characteristics of geopressured reservoirs.

The fluid flow in the wellbore is at present not amenable to strict analytical treatment. Depending upon the relative amounts of gas and liquid, a variety of flow patterns can occur in the pipe. At small gas loadings, bubble flow takes place. This situation is the most likely for geopressured systems since the amounts of free methane gas are generally a small fraction of the produced fluids. An increase in gas flow rate can result in slug, churn or annular flow. Existing techniques for treating two-phase flow in the pipe require use of empirical correlations for liquid hold-up (liquid volume fraction) and friction factor. There exist in the literature numerous such correlations (e.g., Ros [1961], Orkiszewski [1967], Hagedorn and Brown [1964, 1965], Hughmark and Pressubrg [1961], Hughmark [1962], Dukler, et al. [1964]); most of these correlations are based on flow in two-phase petroleum (oil/gas) wells. Utilization of different correlations often yields widely differing results; at present, there does not exist a sufficient basis for selecting one or another of these correlations. A comprehensive investigation is now underway to compare the various correlations, and to identify those most suited for geothermal wells (Coury [1977]). In this study, we use the liquid hold-up correlation of Hughmark [1962] and the frictional pressure drop correlation of

of Dukler, et al. [1964]; it should be, however, emphasized that the mathematical model discussed herein is sufficiently flexible to allow the use of any of the other correlations.

2.2 FLUID FLOW IN THE AQUIFER

We shall restrict this discussion to the isothermal flow of fluids of small and constant compressibility. Assuming that (1) the pressure gradients are small, (2) the fluid has constant viscosity and (3) the reservoir rocks have constant compressibility and isotropic permeability, the governing equation for radial Darcian flow can be written as follows [Matthews and Russell, 1967]:

$$\frac{\partial^2 p}{\partial r^2} + \frac{1}{r}\frac{\partial p}{\partial r} = \frac{\phi\mu}{k} C_T \frac{\partial p}{\partial t} \qquad (2.1)$$

where

C_f ~ fluid compressibility (cm^2/dynes)

C_m ~ formation compressibility (cm^2/dynes)

C_T ~ total compressibility ($=(1-\phi/\phi)C_m + C_f$)

k ~ permeability (cm^2)

p ~ pressure (dynes/cm^2)

r ~ radius (cm)

t ~ time (sec)

ϕ ~ porosity

μ ~ fluid viscosity (poise).

We are interested in the solution of Eq. (2.1) for the case of flow into a fully penetrating centrally located well at a constant volumetric rate of production $q(cm^3/sec)$. The basic solutions for constant rate in conjunction with the principle of superposition can be made to yield solutions for arbitrary rate histories.

We consider a bounded cylindrical reservoir of radial extent R. In this case, the solution for the well-bottom pressure (p_w) at an instant of time t after the start of the production at constant rate q can be expressed with sufficient accuracy as follows [Matthews and Russell, 1967]:

$$p_w = p_i - \frac{q\mu}{4\pi kh}\,\bar{p}(t) \qquad (2.2)$$

where

h = thickness of the aquifer

p_i = initial reservoir pressure,

and

$$p(t) = 2\,\ell n\,\frac{R}{r_w} - \ell n\,1.78 + \ell n\,\frac{4kt}{\phi\mu C_T R^2} \qquad \text{for } \frac{kt}{\phi C_T R^2 \mu} < 0.1$$

$$= \frac{4kt}{\phi\mu C_T R^2} + 2\,\ell n\left(\frac{R}{r_w} - 0.75\right) - 1.68\,\exp\left(-\frac{14.6819\,kt}{\phi C_T\,R^2\,\mu}\right)$$

$$\text{for } 0.1 \le \frac{kt}{\phi C_T R^2 \mu} < 0.3$$

$$= \frac{4kt}{\phi\mu C_T R^2} + 2\,\ell n\left(\frac{R}{r_w} - 0.75\right) \qquad \text{for } \frac{kt}{\phi C_T R^2 \mu} \ge 0.3$$

Let us now consider a reservoir subjected to a variable production history (q_1 for $t \le t_1$; q_2 for $t_1 \le t \le t_2$; q_3 for $t_2 \le t \le t_3$; ...; q_n for $t_{n-1} \le t \le t_n$).

The principle of superposition together with the constant production rate solution now yields the following result for p_w:

$$p_i - p_w = \frac{\mu}{4\pi kh} [q_1 \bar{p}(t) + (q_2-q_1) \bar{p}(t-t_1) + (q_3-q_2) \bar{p}(t-t_2) + \ldots + (q_n-q_{n-1}) \bar{p}(t-t_{n-1})] \quad (2.3)$$

The principle of superposition can also be written in a continuous form as opposed to the discrete form, Eq. (2.3); we shall not, however, require the continuous form.

2.3 TWO-PHASE FLOW IN WELL-PIPE

In this section, we shall present the governing equations for two-phase (liquid water with dissolved methane and free methane) non-isothermal steady flow in a vertical pipe. The assumption of steady flow implies that the mass flux (G) is constant along the length of the pipe

$$G = \rho v = \text{constant} \quad (2.4)$$

where

ρ (mixture density) = $R_\ell \rho_\ell + R_g \rho_g$

v (mixture velocity) = $(R_\ell \rho_\ell v_\ell + R_g \rho_g v_g)/\rho$

$v_\ell (v_g)$ = liquid (gas) velocity

$R_\ell (R_g)$ = liquid (gas) volume fraction

$\rho_\ell (\rho_g)$ = liquid (gas) density.

The pressure drop due to fluid flowing in a vertical pipe represents the combined effects of friction, acceleration, and the loss of elevation.

$$-\frac{dp}{dZ} = \rho g - \frac{d\bar{p}_f}{dZ} - G^2 \frac{d}{dZ}\left[\frac{(1-x)^2}{\rho_\ell R_\ell} + \frac{x^2}{\rho_g R_g}\right] \qquad (2.5)$$

loss of elevation — frictional gradient — acceleration gradient

where

g = absolute value of acceleration due to gravity

x = flowing gas quality = $\rho_g R_g v_g / G$

Z = elevation above well-bottom (Z = 0).

The frictional pressure gradient $d\bar{p}_f/dZ$ is specified by empirical correlations; one such correlation is due to Dukler, et al. [1964]. According to Dukler, et al., $d\bar{p}_f/dZ$ can be written as follows:

$$\frac{d\bar{p}_f}{dZ} = \frac{2G^2 f_0}{\rho_{NS} d} A(\lambda)\ \beta \qquad (2.6)$$

where

d = pipe diameter (cm)

$$\lambda = \frac{R_\ell v_\ell}{R_\ell v_\ell + R_g v_g} = \frac{1}{1 + \frac{x}{1-x}\frac{\rho_\ell}{\rho_g}}$$

$$\rho_{NS} = \rho_\ell \lambda + \rho_g (1-\lambda) \quad (gm/cm^3)$$

$$\mu_{NS} = \mu_\ell \lambda + \mu_g (1-\lambda) \quad (poise)$$

$$\beta = (\rho_\ell/\rho_{NS})\ \lambda^2/R_\ell + (\rho_g/\rho_{NS})(1-\lambda)^2/R_g$$

$$R_e = Gd\beta/\mu_{NS}$$

$$f_0 = 0.00140 + 0.125/(R_e)^{0.32}$$

and

$$A(\lambda)=1.0+\frac{-\ell n\lambda}{1.281-0.478(-\ell n\lambda)+0.444(-\ell n\lambda)^2-0.094(-\ell n\lambda)^3+0.00843(-\ell n\lambda)^4}$$

The mixture (liquid with dissolved methane and free methane) energy balance for two-phase flow in the pipe yields:

$$\frac{d}{dZ}\left[h_\ell + x\, h_{fg}\right] = -\frac{G^2}{2}\frac{d}{dZ}\left[\frac{(1-x)^3}{R_\ell^2\ \rho_\ell^2} + \frac{x^3}{R_g^2\ \rho_g^2}\right] - g - \frac{\bar{Q}}{G} \qquad (2.7)$$

where

$h_\ell (h_g)$ = liquid (gas) enthalpy

h_{fg} = $h_g - h_\ell$

$\bar{Q}$ = heat loss to the formation.

The average heat loss to the surrounding formation $\bar{Q}$ can be approximated by

$$\bar{Q} = \frac{4U}{d}(T - T_R) \qquad (2.8)$$

where U is the overall heat transfer coefficient and T and T_R are the average temperatures of the mixture and the formation, respectively. Note that U will, in general, have different values in single- and two-phase regions.

In addition to the mixture mass, momentum and energy balance relations discussed above, we require a mass balance relation for methane (both dissolved in liquid and free gas). Introducing

α = mass fraction of total methane in mixture
$= (R_\ell \rho_\ell m_d + R_g \rho_g)/\rho$

m_d = mass fraction of dissolved methane in liquid

Q = quality $= R_g \rho_g / \rho$,

the mass balance for methane can be written as follows:

$$\frac{d}{dZ}\left[\frac{\alpha(1-x) + x - Q}{1-Q}\right] = 0 \qquad \text{for } m_d > 0$$

and (2.9)

$$\frac{d}{dZ}[x] = 0 \qquad \text{for } m_d = 0.$$

The flowing gas quality x is generally different from the quality Q; this is due to slip between the gas and the liquid (in the event there is no slip, we have $v_\ell = v_g$ and $x = Q$). To determine the relationship between x and Q (or R_ℓ) in slip flow, it is necessary to resort to empirical correlations. As mentioned earlier, many such correlations can be found in the literature; at present, there exists little rational basis for choosing one correlation over another. In the present work, for purposes of illustration only, we will employ the correlation of Hughmark [1962]. According to Hughmark, the flowing quality x is given by the relation

$$\frac{1}{x} = 1 - \frac{\rho_\ell}{\rho_g}\left(1 - \frac{K}{R_g}\right) \qquad (2.10)$$

where

$$K \equiv K(z) \text{ (see below)}$$

$$z = (N_{Re})^{1/6} (N_{Fr})^{1/8} / (y_\ell)^{1/4}$$

$$N_{Re} = Gd/\mu_m$$

$$\mu_m = R_\ell \mu_\ell + R_g \mu_g$$

$$N_{Fr} = v^2/gd$$

$$y_\ell = 1/[1 + x\rho_\ell/(1-x)\rho_g]$$

$$K(z) = 0.1363\ z^{1.165} \qquad \text{for } z \leq 3$$

$$= 0.1363\ z^{1.165} + (z-3)^2\ [-0.080613 + 0.012858\ (z-3)] \qquad \text{for } 3 < z < 5$$

$$= 1 - 0.8529/z^{0.58848} \qquad \text{for } z \geq 5.$$

We note that the system of governing equations discussed in the foregoing contains liquid and gas viscosities, enthalpies (or equivalently internal energies since $E = h - p/\rho$) and densities in addition to pressure, temperature, relative gas volume and the mass fraction of methane. An equation-of-state package for a water-methane mixture with p, E ($=\rho_\ell R_\ell E_\ell + \rho_g R_g E_g)/\rho$), and α as the calling arguments, valid in the temperature range from 0°C to 300°C, was developed during the first year of this effort (see Garg, et al.[1977]). Given pressure, p, mixture internal energy, E, and the methane mass fraction, α, the equation-of-state package returns values for mixture density ρ, temperature T, partial derivatives of pressure and temperature with respect to the calling arguments, the volume fractions of the liquid and gaseous phases, the energy fractions of each component in the liquid and gaseous phases, and the internal energies and viscosities of the liquid and gaseous phases. If necessary, the equation-of-state

package can also be called by either (P,T,α) or (ρ,E,α) as the independent arguments.

Given the total mass flux G and the thermodynamic state of the fluid (ρ_ℓ, ρ_g, R_ℓ, R_g, Q, x, α, p, T, E_ℓ, E_g, etc.) at some datum Z_1, the fluid state at another datum Z_2 is calculated using the following iterative procedure:

Step 1

Assign provisional values for the various thermodynamic variables at Z_2 (p, T, R_g, R_ℓ, ρ_ℓ, ρ_g, x, Q, E_ℓ, E_g, μ_ℓ, μ_g, α). During the first pass, it is convenient to assume that the value of a variable at Z_2 is equal to its value at Z_1.

Step 2

Solve Eq. (2.10) for x at Z_2.

Step 3

Solve Eq. (2.5) for the pressure drop in the interval (Z_2-Z_1); update pressure at Z_2.

Step 4

Solve Eq. (2.7) for h at Z_2. Update E_ℓ at Z_2 ($E_\ell = h_\ell - p/\rho_\ell$). Compute E ($= E_\ell + Q\,(E_g - E_\ell)$) at Z_2.

Step 5

Solve Eq. (2.9) for α at Z_2.

Step 6

Call the equation-of-state package with updated values of p, E and α as the calling arguments, and update the thermodynamic variables (ρ_ℓ, ρ_g, E_ℓ, E_g, R_ℓ, R_g, μ_ℓ, μ_g, T, Q) at Z_2.

Step 7

Test for convergence. If the change in pressure during the present iteration is below some specified level, then we can proceed to the calculation of flow properties at the next datum z_3. Otherwise, return to Step 2.

The above iterative procedure is quite efficient, and convergence is usually obtained in 3-4 passes. The present method has the additional advantage that it can treat both single and two-phase regions; this approach may be contrasted with that of several previous authors (e.g., Coury [1977]) who found it necessary to utilize separate computational procedures in the single- and two-phase regions.

2.4 COUPLED AQUIFER - WELLBORE MODEL

In order to study the production behavior of a geopressured well, it is necessary to couple the aquifer response to the fluid flow in the well-pipe. A typical production calculation proceeds in the following steps.

Step 1

Specify reservoir diameter and thickness, porosity, permeability and compressibility; initial reservoir fluid state (p, T, α); well-pipe diameter (d) and well-head pressure (p_{top}), heat loss coefficient (U) and formation temperature (T_R); initial reservoir volume production rate (q_1 cm^3/sec); time step Δt and maximum time (t_{max}).

Since no flashing of water to steam is allowed for in the model, p_{top} must be above the flashing pressure. Figure 2.1 shows the flashing pressure for water as a function of temperature. We also do not allow the evolution of free methane in the rock pores; this of necessity implies that the acquifer properties, initial fluid state and the rate of production must be selected so as to preclude well-bottom pressures

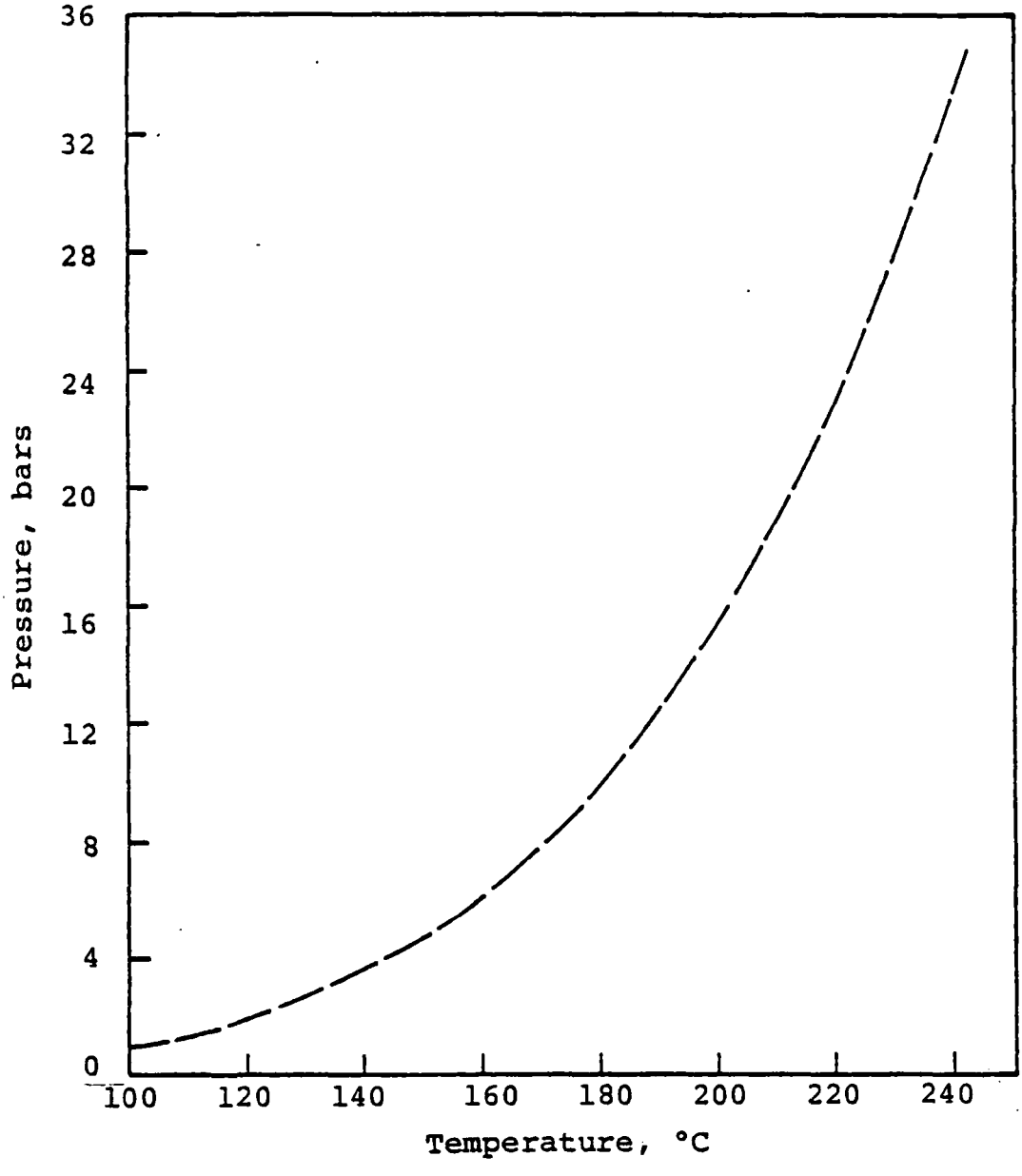

Figure 2.1. Flashing pressure for liquid water to steam as a function of temperature.

(p_w) below the pressures at which free-methane can evolve from the solution. Figure 2.2 gives the pressure for the incipient release of methane from the liquid as a function of reservoir temperature T and methane mass fraction α.

Step 2

For a given time step Δt, use Eq. (2.3) to calculate the well-bottom pressure p_w. The state of the fluid entering the cased part of the production hole is specified by p_w, initial reservoir temperature, T, and initial methane mass fraction α in the reservoir fluid.

Step 3

Utilize the two-phase fluid flow model to calculate the conditions at the well-head. If the calculated pressure is greater than p_{top}, then proceed to the next time step. In case $p_{calculated} < p_{top}$, reduce the flow-rate q by a specified amount (usually 1 percent) and return to Step 2.

Step 4

The calculation is stopped when either t_{max} is reached or the fluid production rate, q, falls below some specified value.

2.5 NUMERICAL RESULTS

In this section, we will utilize the mathematical model outlined in the preceding sections to analyze the production behavior of a hypothetical geopressured geothermal reservoir. More specifically, we will examine the effects on production of aquifer permeability and compressibility, depth of the geopressured reservoir, reservoir temperature, and the dissolved methane content of the reservoir fluids. For this series of parametric calculations, it is convenient to consider a standard base case and to vary the parameters of interest around the values assumed in the base case. Parameters

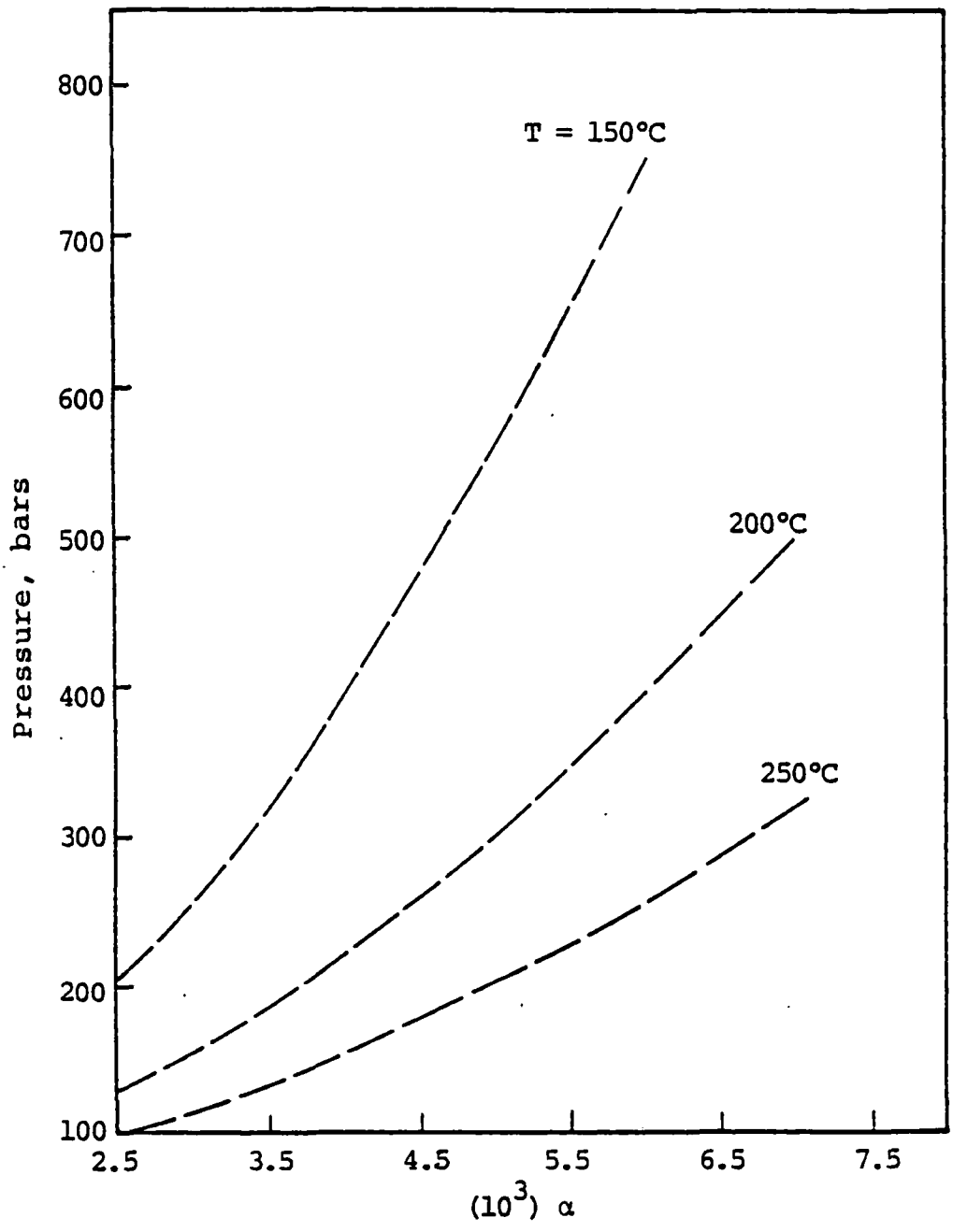

Figure 2.2. Boundary of two-phase region for water-methane mixture. Single phase region lies above the appropriate temperature curve.

for the base case (roughly based on the Kenedy County, Texas prospect. See Knapp and Isokrari [1976]) are listed in Table 2.1. All the calculations reported hereunder were done either for a production period of 30 years, or until the mass production rate fell below a specified rate.

Figure 2.3 illustrates the effects of aquifer permeability on well-head pressure and the fluid production rate. For both the base (k = 20 md) and the high permeability (k = 30 md) cases, the reservoir can be produced at a constant rate (note that constant q implies slightly declining mass flow rate $\dot{m}$) for 30 or more years; the principal effect of increasing permeability is to raise the well-head pressures and thus to prolong the producing life of the well. For k = 10 md, the reservoir cannot be produced at a constant rate; as a matter of fact, mass production rate drops from a high of 66.4 kg/sec to a low of 48.1 kg/sec in 30 years.

As discussed elsewhere in this section, formation compressibility provides one of the major drive mechanisms in geopressured reservoirs; this effect is illustrated in Figure 2.4. Higher formation compressibility helps to maintain the reservoir (and hence well-head) pressures and high production rates (see curves labeled $C_m = 0.175\ 10^{-9}$ cm^2/dynes and $C_m = 0.875\ 10^{-10}$ cm^2/dynes). If the compressibility to too low (see, e.g., $C_m = 0.175\ 10^{-10}$ cm^2/dynes curves), it may be necessary to reduce the mass production rate to maintain a specified well-head pressure.

The pressure drop in the well-pipe represents the combined effects of friction, acceleration, and the loss of elevation; of the three pressure drop mechanisms, the loss of elevation is the most important. Figure 2.5 shows the effects of the depth of geopressured reservoir H on the well-head pressure and the fluid production rate. Increasing H results in lower values for well-head pressures; if H is sufficiently great, it may become necessary to reduce the fluid mass production rate.

TABLE 2.1

RESERVOIR AND WELLBORE PARAMETERS FOR THE BASE CASE

A. Reservoir Properties

Porosity $\phi = 0.2$

Permeability $k = 0.2\ 10^{-9}$ cm^2 ($\sim$ 20 md)

Reservoir Radius $R = 0.6\ 10^{6}$ cm

Reservoir Thickness $h = 0.5\ 10^{4}$ cm

Formation Compressibility $C_m = 0.175\ 10^{-9}$ cm^2/dynes

B. Initial Fluid Properties

Pressure, $p_i = 750$ bars

Temperature, $T = 150°C$

Mass Fraction of Dissolved Methane, $\alpha = 0.0025$

C. Well-Data

Well Radius, r_w (=d/2) = 10 cm

Minimum Well-Head Pressure, $p_{top} = 35$ bars

Well-Head Datum $H = 0.35\ 10^{6}$ cm

Heat Loss Coefficient, $U = 0$ cal/sec cm^2°C

Initial Reservoir Volume Production $q = 0.75\ 10^{5}$ cm^3/sec

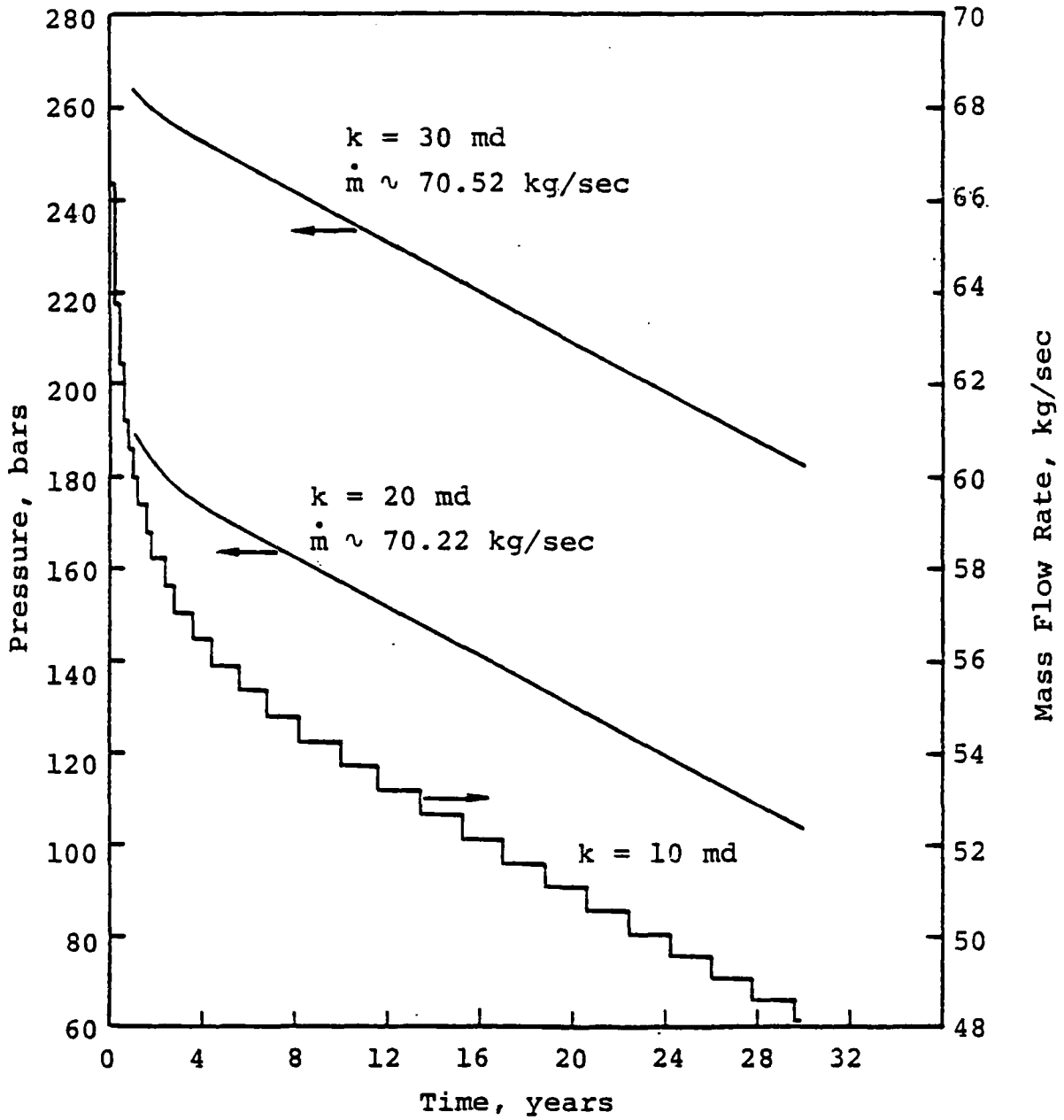

Figure 2.3. Effect of aquifer permeability on fluid production. For k = 10 md, it is not possible to maintain a constant production rate.

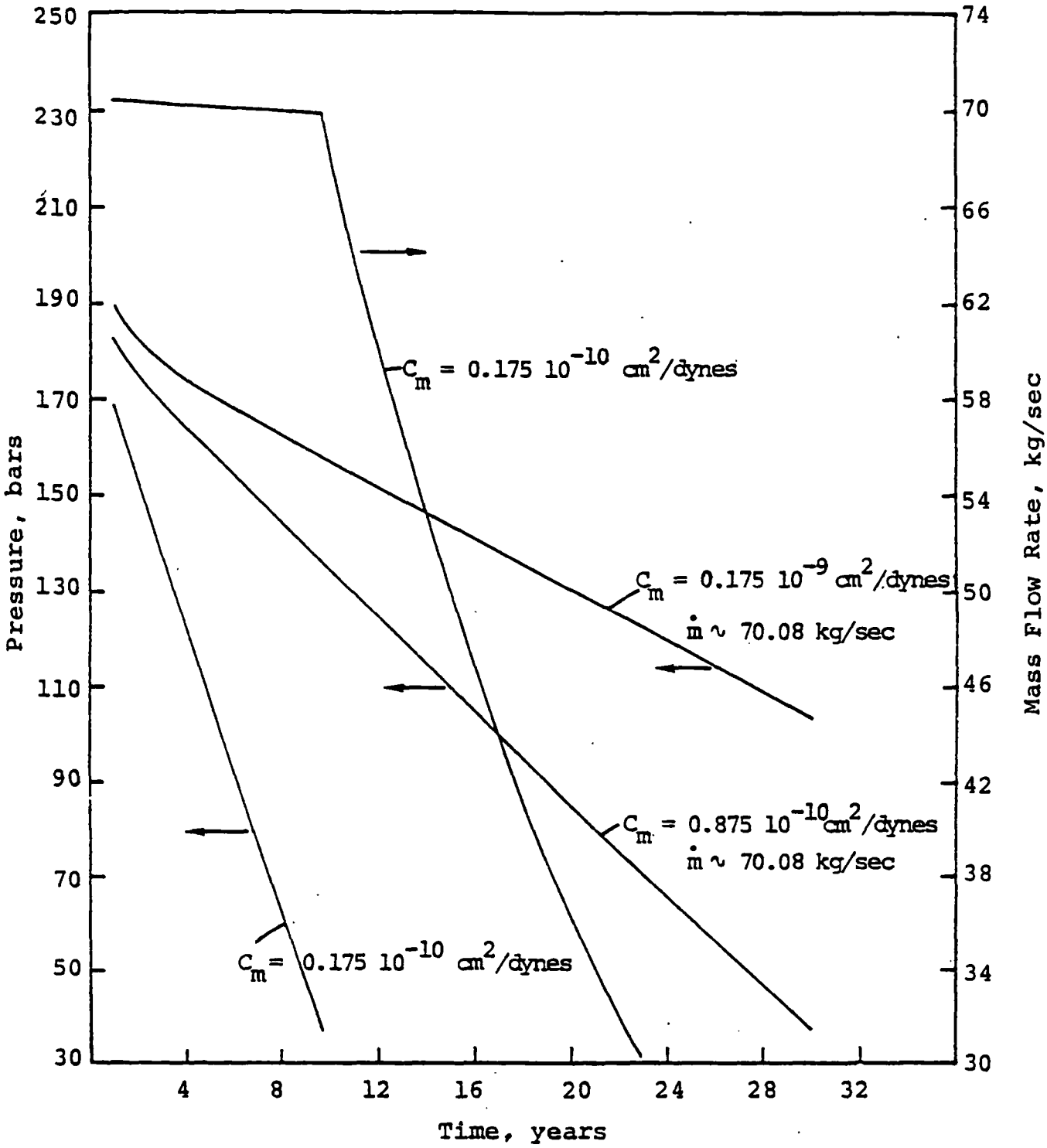

Figure 2.4. Effect of formation compressibility on well-head pressure and mass production rate.

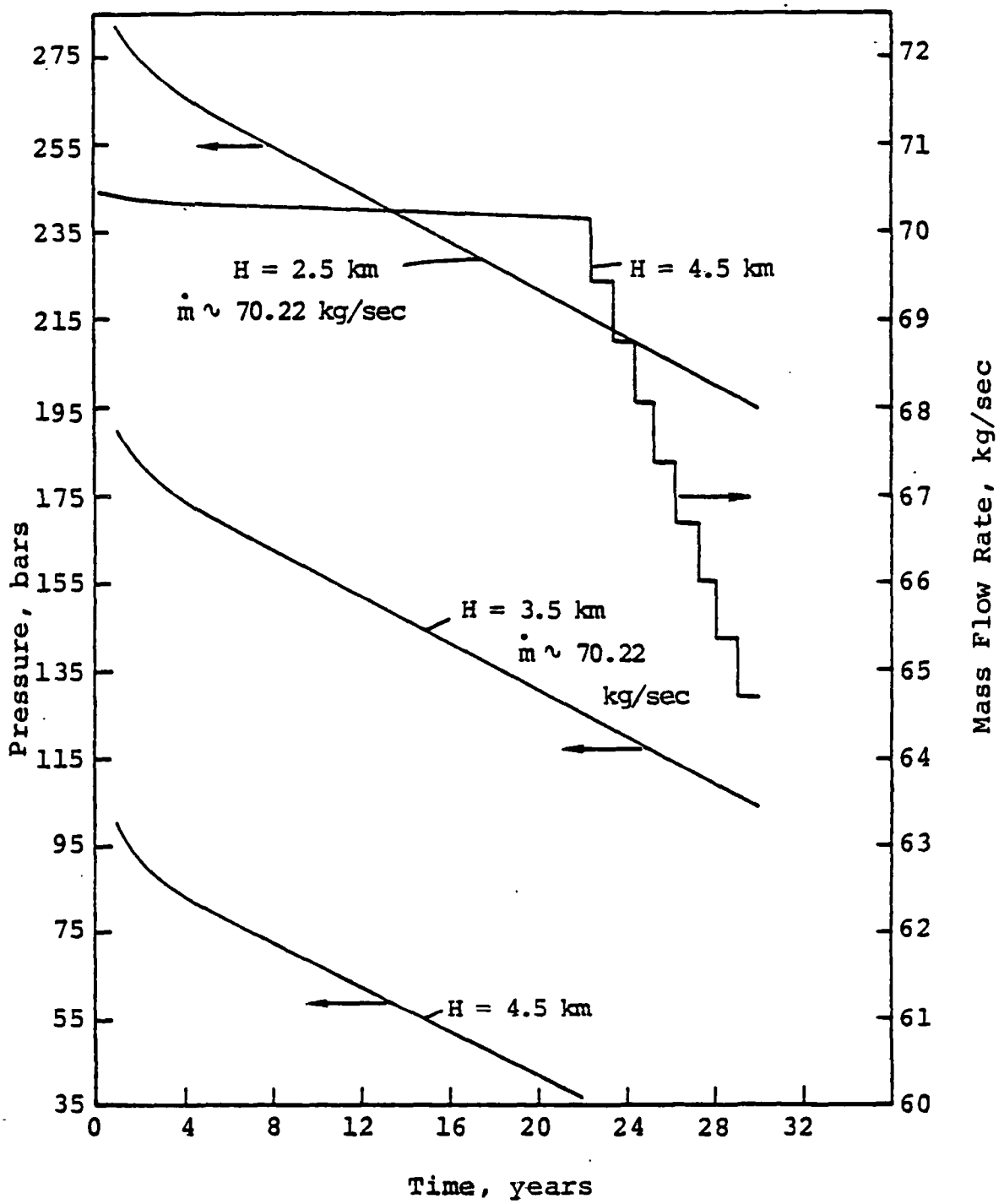

Figure 2.5. Effect of depth of geopressured reservoir on well-head pressure and fluid production rate.

An increase in fluid temperature (at constant pressure is accompanied by decreases in viscosity (and hence increased mobility in the aquifer) and fluid density (and therefore a reduction in mass flow rate at a specified volume flow rate). Figure 2.6 demonstrates the effects of the temperature of reservoir fluids on the well-head pressures and the mass production rates. An increase in fluid temperature leads to higher well-head pressures; the reduction in mass flow rate with increases in temperature is a consequence of maintaining a specified volume flow rate and is thus not indicative of a loss of mass production capability.

Figure 2.7 shows the effect of the methane mass fraction α on the well-head pressure; increasing α results in slightly higher well-head pressures. The latter effect arises from the nature of the fluid flow (single-phase for $\alpha = 0$ versus two-phase for $\alpha = 0.0025$) in the well-pipe. It should be noted here that α can have a more significant effect on reservoir production characteristics if the pressure drop is such that two-phase flow (see Figure 2.1) occurs in the aquifer (see, e.g., Garg, et al. [1977]).

2.6 CONCLUDING REMARKS

The coupled aquifer-wellbore model presented in the preceding can be used for assessing the production characteristics of a geopressured geothermal reservoir provided the fluid flow in the reservoir is single-phase and isothermal. In order to treat two-phase and variable property (viscosity, compressibility, etc.) non-isothermal flow in the aquifer, it is necessary to couple the wellbore model to the computer models for the aquifer referred to in Section 2.1. In numerical simulation of reservoir behavior, it is often necessary to utilize well-blocks (i.e., a grid block containing a well) with dimensions much larger than the well radius; naturally, the calculated grid block pressure will be different from the actual flowing bottom-hole pressure. In Section IV, we

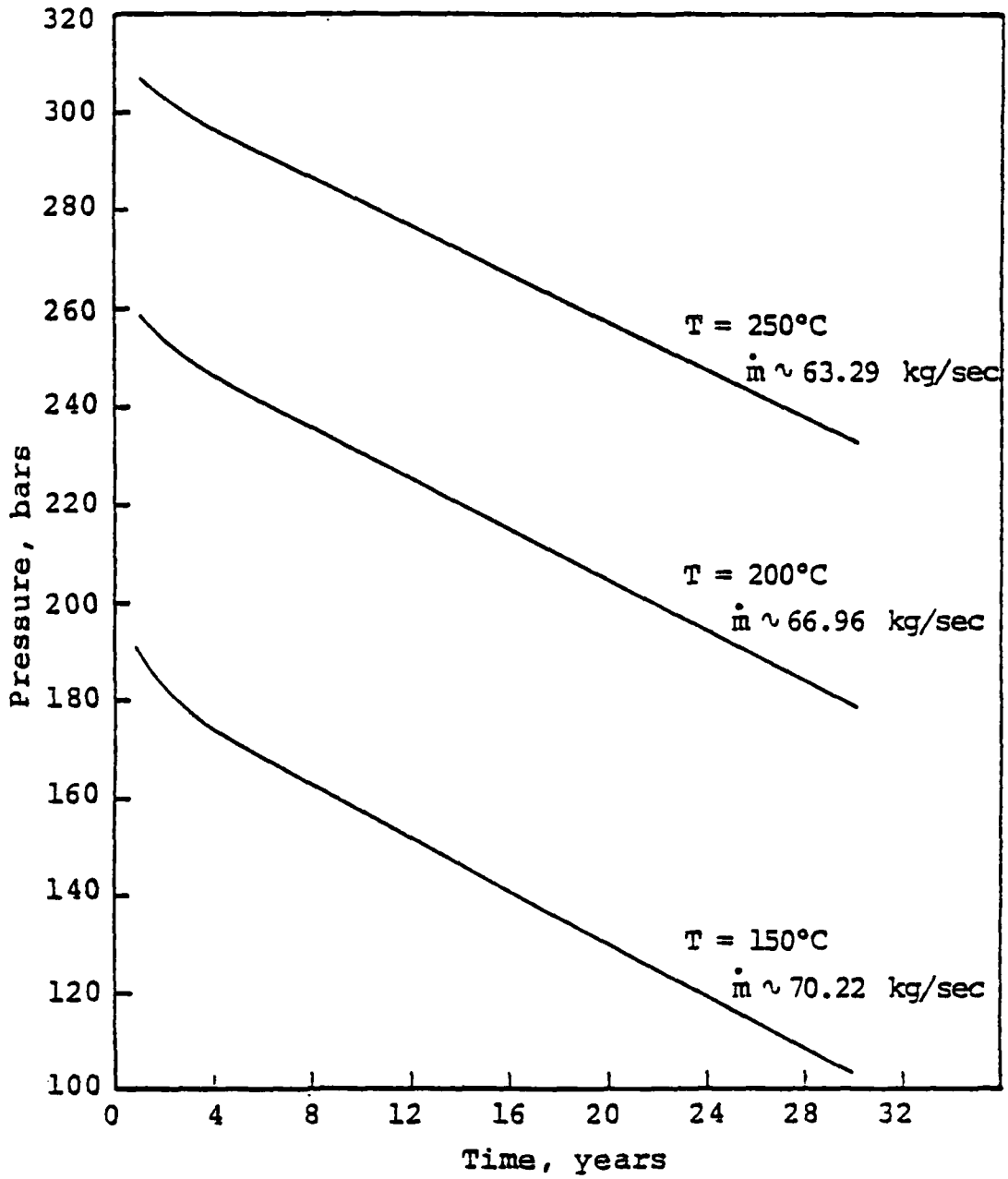

Figure 2.6. Effect of reservoir fluid temperature on well-head pressure and mass production rate.

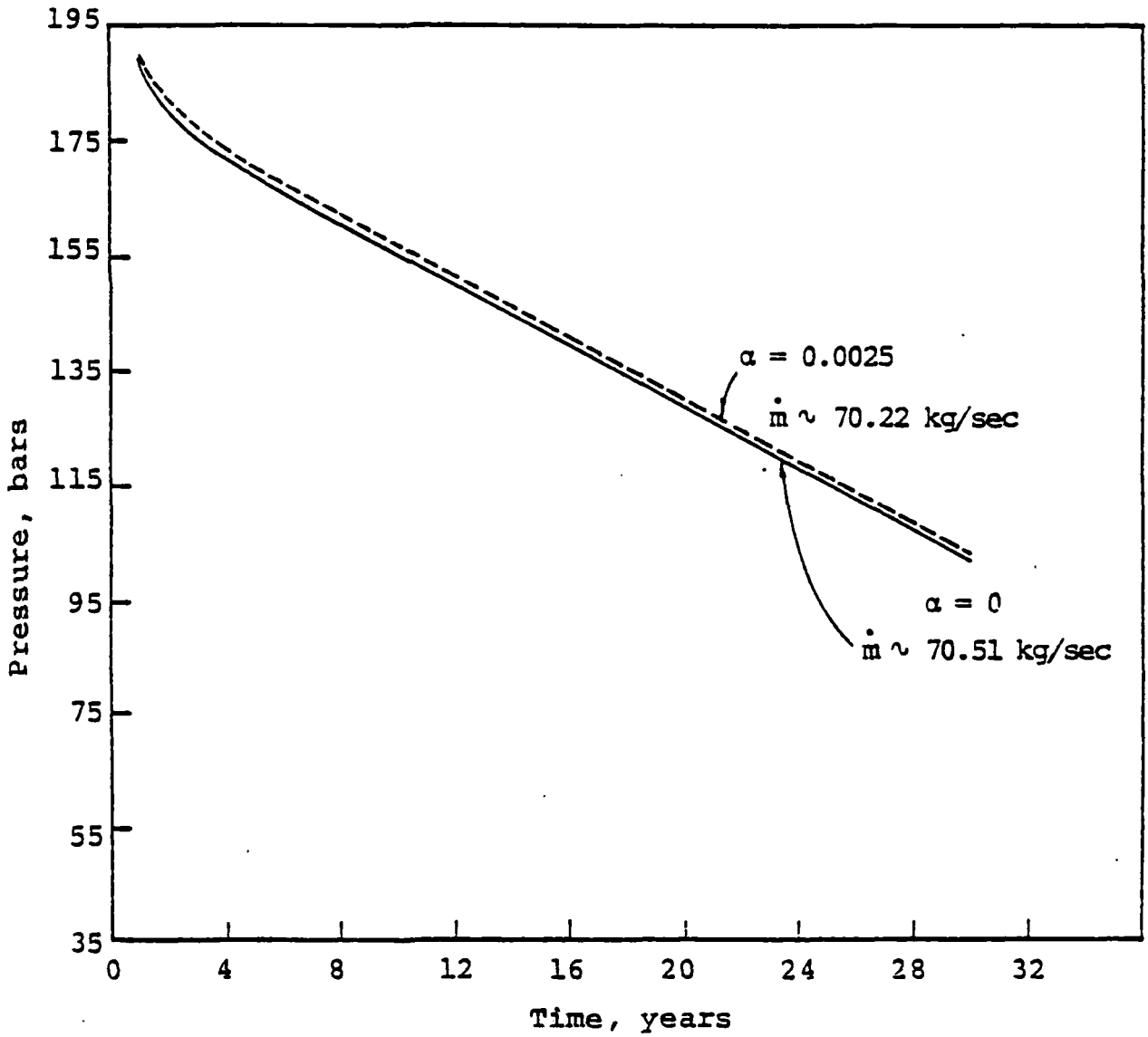

Figure 2.7. Effect of methane content α on well-head pressure.

consider local two-phase flow within a computational cell and describe the procedure for calculating the sandface conditions from the well-block conditions when the well is completed within a single computational zone. It is possible that a geopressured well will produce from several sand bodies separated by interbedded shales/clays; in this case, it is necessary to generalize the local two-phase treatment (outlined in Section IV) to multiple completions. This generalization, along with the inclusion of the wellbore model in the numerical simulator, will be accomplished during the early part of the third year of this project.

III. PRESSURE TRANSIENT ANALYSIS FOR GEOPRESSURED GEOTHERMAL RESERVOIRS

3.1 INTRODUCTION

In petroleum engineering and groundwater hydrology, well tests are routinely conducted to diagnose the well's condition and to estimate formation properties. Analysis of well-test data may be made to yield quantitative information regarding (1) formation permeability, storativity and porosity, (2) the presence of barrier and leaky boundaries, (3) the condition of the well (i.e., damaged or stimulated), (4) the presence of major fractures close to the well and (5) the mean formation pressure. Well testing procedures (and the quality of information obtained) depend on the age of the well. During temporary completion, testing involves producing the reservoir using a temporary plumbing system (e.g., drill stem testing); and the estimates obtained for the formation parameters are not very accurate. After completion, testing is usually performed in the hydraulic mode. In hydraulic testing, one or more wells are produced at controlled rates and changes in pressure within the producing well itself (drawdown/buildup tests) or nearby observation wells (interference tests) are monitored.

A major concern of well-testing is the interpretation of pressure transient data. Practical procedures presently exist for analyzing pressure transient data from isothermal single-phase (water, oil) and isothermal two-phase (oil with gas in solution, free gas) systems (see Ramey [1975], and Matthews and Russell [1967] for reviews of existing literature). The assumption of isothermal flow invoked in these analyses is justified for geopressured well-tests. However, a second major assumption invoked is that the formation compaction is small enough such that any associated changes in formation thickness and permeability may be neglected. This

assumption is most likely inappropriate for geopressured systems. It is generally believed that geopressured reservoirs contain undercompacted sandstones/shales which will undergo substantial (and possibly irreversible) compaction on fluid production; the formation compaction will be accompanied by significant changes in porosity and permeability. In this section, we present a series of drawdown/buildup calculations designed to assess the applicability of classical petroleum engineering/hydrology procedures to geopressured systems; more specifically, we will examine the effects of irreversible formation compaction, and changes in porosity and permeability.

Section 3.2 presents the mathematical basis for the classical interpretation procedures. In the numerical simulation of well-test data, it is often necessary to employ well-blocks with dimensions much larger than the wellbore radius; the relationship between the calculated well-block pressure and the actual flowing pressure is briefly discussed in Section 3.3. A series of drawdown and buildup calculations to assess the effects of nonlinearities in the formation response is presented in Section 3.4; for these calculations, the region near the wellbore was finely zoned to eliminate the uncertainties associated with the use of an 'equivalent radius' (i.e., radius at which calculated well-block pressure is equal to the actual flowing pressure). Finally in Section 3.5, we discuss the question of 'equivalent radius' in transient flow.

3.2 MATHEMATICAL THEORY OF PRESSURE-TRANSIENT ANALYSIS

We consider a fully penetrating well located in the center of an infinite reservoir of thickness h. We will neglect any variations in either formation or fluid properties in the vertical direction (this is a common assumption in pressure transient analysis). The geopressured reservoir may either be single-phase (liquid water with or without dissolved

gas), or two-phase (liquid water with dissolved gas, and free gas). In the following, we will briefly outline the theoretical foundations for these two cases.

3.2.1 Single-Phase Flow

We shall consider the isothermal flow of a liquid of small compressibility. Assuming that (1) the pressure gradients are small, (2) the liquid has constant viscosity and (3) the formation has constant compressibility, and constant and horizontally isotropic permeability, the governing equation for radial Darcian flow can be written as follows [Matthews and Russell, 1967]:

$$\frac{\partial^2 p}{\partial r^2} + \frac{1}{r}\frac{\partial p}{\partial r} = \frac{\phi\mu}{k} C_T \frac{\partial p}{\partial t} \qquad (3.1)$$

where

C_f = fluid compressibility

C_m = formation compressibility

C_T = total compressibility $= \frac{(1-\phi)}{\phi} C_m + C_f$

k = permeability

p = pressure

r = radius

t = time

ϕ = porosity

μ = fluid viscosity

We are interested in the solution of Eq. (3.1) for the case of flow into a fully penetrating well (located in an infinite reservoir of thickness h) at a constant volumetric rate of production (q). The basic solution for constant rate of production in conjunction with the principle of superposition, can

be made to yield solutions for arbitrary rate histories. In this case, the solution for the well-bottom pressure (p_w) at an instant of time t after the start of the production at constant rate q can be expressed as:

$$p_w = p_i + \frac{q\mu}{4\pi kh}\left\{Ei\left(\frac{-\phi\mu C_T r_w^2}{4kt}\right)\right\} \qquad (3.2)$$

where

$$-Ei\ (-z) = \int_z^\infty \frac{e^u}{u}\ du.$$

For $\frac{4\ k\ t}{\phi\mu C_T r_w^2} > 100$, Eq. (3.2) is closely approximated by

$$p_w = p_i - \frac{1.15\ q\mu}{2\pi\ kh}\left[\log_{10}\frac{kt}{\phi\mu C_T r_w^2} + 0.351\right] \qquad (3.3)$$

Equation (3.3) forms the basis of many well data interpretation techniques; it implies that the plot of p_w versus $\log_{10} t$ should be a straight line. The slope of the straight line yields the permeability k (assuming h is known); and Eq. (3.3) may then be utilized to determine the storativity $\phi h\ C_T$. In applying Eq. (3.3) to practical systems, it is important to bear in mind the fundamental assumptions (i.e., (1) constant formation thickness and permeability, and (2) constant formation compressibility) employed in deriving Eq. (3.1). In Section 3.4, we shall describe a series of calculations simulating the effects of formation compaction and the associated reductions in porosity and absolute permeability. We shall find that the use of Eq. (3.3) may be expected to yield reliable formation permeability data even when the formation compaction is accompanied by reductions in permeability,

but storativity estimates will be unreliable. Another factor that may make the use of Eq. (3.3) unreliable for determining average formation pressure from buildup tests is the irreversible compaction behavior of the formation.

3.2.2 Two-Phase Flow

A theoretical framework for analyzing isothermal multiphase pressure tests in oil/gas reservoirs was developed by Martin [1959]. Assuming that (1) the liquid and the (free) gas have constant but small compressibilities (2) pressure and gas saturation gradients are small, (3) the capillary pressure is negligible and relative permeabilities depend only upon the gas saturation, (4) the liquid and the gas have constant viscosities and (5) the formation has constant compressibility, and constant horizontally isotropic permeability, the governing equation for radial Darcian flow can be written as:

$$\frac{\partial p}{\partial t} = \frac{(k/\mu)_T}{\phi C_T} \left[\frac{1}{r} \frac{\partial p}{\partial r} + \frac{\partial^2 p}{\partial r^2} \right] \qquad (3.4)$$

where

$$(k/\mu)_T = k \left[\frac{R_\ell}{\mu_\ell} + \frac{R_g}{\mu_g} \right] = \text{total mobility.}$$

k = absolute permeability

$R_\ell (R_g)$ = relative permeability for liquid (gas)

$\mu_\ell (\mu_g)$ = liquid (gas) viscosity

C_T = total compressibility = $\frac{(1-\phi)}{\phi} C_m + C_f$

C_f = fluid compressibility = $(1-S)\, C_\ell + S\, C_g$

$$+ \frac{(1-S)\rho_\ell}{\rho_g} \frac{\partial \alpha_\ell}{\partial p}$$

S = gas volume fraction

$C_\ell (C_g)$ = liquid gas compressibility

α_ℓ = mass of dissolved gas per unit mass of liquid

It is straightforward to write down solutions for Eq. (3.4) by noting the correspondence between it and Eq. (3.1). Thus the well-bottom pressure for constant volumetric rate of production is given by Eqs. (3.2) and (3.3) with k/μ replaced by $(k/\mu)_T$.

3.2.3 Drawdown and Buildup Tests

As mentioned earlier, after completion, well-testing is usually performed in the hydraulic mode. In hydraulic testing, a well is produced at a controlled rate (usually at a constant volumetric rate q) for some time t. At time t, the flow rate is suddenly dropped to zero. Changes in bottom-hole pressure are monitored both during the drawdown (i.e., production) and buildup (time > t) periods. The bottom-hole pressure during drawdown is given by Eq. (3.3). An expression for bottom-hole pressure during buildup can be easily obtained by superposition.

$$p_w = p_i - \frac{1.15\, q\mu}{2\pi\, kh} \log \frac{t + \Delta t}{\Delta t} \tag{3.5}$$

where Δt denotes the buildup time. Equation (3.5) implies that a plot of p_w versus $\log (t + \Delta t/\Delta t)$ (usually called a Horner plot) should be a straight line. Let m be the slope of this straight line; then we have

$$k = \frac{1.15\, q\mu}{2\pi h} \tag{3.6}$$

In the limit $t + \Delta t/\Delta t \to 1$ (very large buildup times), Eq. (3.5) implies that $p_w \to p_i$. For the sake of clarity, we shall denote $\lim_{(t + \Delta t)/\Delta t \to 1} p_w$ by p^*. Note that $p^* \to p_i$ only for

infinite reservoirs; for finite reservoirs p* is in general different from p_i.

In writing down Eq. (3.5), it was implicitly assumed that the formation compressibility C_m (and also total compressibility C_T) is the same whether pore-pressure is increasing or decreasing. For geopressured formations, this is probably a poor assumption. Geopressured formations will most likely undergo irreversible pore compaction with reductions in pore pressure (drawdown). Assuming that

$$C_m = C_{mL} \text{ for } \partial p/\partial t < 0$$
$$= C_{mU} \text{ for } \partial p/\partial t > 0$$

and that during buildup formation compressibility is given by C_{mU} (this is not strictly true as pore pressure may be falling in parts of the reservoir distant from the borehole), the bottom-hole pressure can be approximated by:

$$p_w = p_i + \frac{1.15\, q\mu}{2\pi\, kh} \log \frac{C_{TL}}{C_{TU}} - \frac{1.15\, q\mu}{2\pi\, kh} \log \frac{t + \Delta t}{\Delta t} \qquad (3.7)$$

where

$$C_{Ti} = \frac{1 - \phi}{\phi} C_{mi} + C_f, \quad i = L, U.$$

Equation (3.7), like Eq. (3.5), implies that the formation permeability k is given by Eq. (3.6). Given the initial pressure p_i, and the slope m, Eq. (3.7) may be solved to yield the ratio C_{TL}/C_{TU}. We shall show in Section 3.4 that estimates for C_{TL}/C_{TU} obtained in this manner are only approximate due to the assumptions involved (i.e., use of (1) C_{mU} to characterize formation compressibility during buildup and (2) superposition) in deriving Eq. (3.7).

3.3 RELATIONSHIP BETWEEN WELL-BLOCK AND FLOWING BOTTOMHOLE PRESSURES

In the numerical simulation of reservoir behavior, it is often necessary to employ well-blocks (i.e., a grid block containing a well) with dimensions much larger than the well-bore radius. Naturally, the pressure calculated for the well-block will be, in general, different from the actual flowing bottomhole pressure. Van Poolen, et al. [1968] state that the calculated pressure for a well-block should be the average pressure in the portion of the reservoir represented by the block. Assuming steady-state single-phase flow in the well-block (but not in the reservoir as a whole), this implies that the calculated well-block pressure should be equal to the actual flowing pressure at a radius r_w,

$$\ln \frac{r_w}{r_0} = \frac{R^2 \ln (R/r_0)}{R^2 - r_0^2} - \frac{1}{2} \tag{3.8}$$

where r_0 is the actual well radius, and R is the radius of the radial grid-block. For $R >> r_0$, Eq. (3.8) simplifies to

$$\frac{r_w}{R} = e^{-1/2} \sim 0.6065 \tag{3.9}$$

Equations (3.8) and (3.9), strictly speaking, hold only for a well located in the center of a radial grid block. For rectangular grid-blocks (with dimensions Δx, Δy), Eq. (3.9) is usually replaced by the following expression

$$\frac{r_w}{\sqrt{\Delta x \Delta y}} = \frac{0.6065}{\sqrt{\pi}} \tag{3.10}$$

Assuming $\Delta x = \Delta y$, Eq. (3.10) yields

$$\frac{r_w}{\Delta x} = 0.342$$

Peaceman [1977] examined the grid pressures obtained in the numerical solution of steady incompressible single-phase flow into a single well located in the center of a square grid-block ($\Delta x = \Delta y$) and concluded that the well-block pressure should be equal to the actual flowing pressure at a radius of $0.2\,\Delta x$ (and not at the radius given by Eq. (3.10)).

In an attempt to evaluate the significance of Peaceman's results for numerical simulation, we have analyzed (see Appendix for details of the analysis) the numerical solution of steady incompressible single phase flow into a single well located in both radial and rectangular grid blocks. It is found that the equivalent radius depends, among other things, on the shape of the grid-block (radial or rectangular) and the type of mesh (uniform or stretch) employed. Thus, for example, use of uniform radial mesh yields $r_w/R \simeq 0.5615$ in the limit $N \to \infty$, where N denotes the number of grid-blocks. Results for several other mesh-types are discussed in the Appendix.

We shall return to the question of equivalent radius in Section 3.5 where we will compare the numerical solution for transient, slightly compressible (water) single-phase flow into a single well with the line-source solution for the diffusivity equation.

3.4 NONLINEAR FORMATION RESPONSE, TWO-PHASE FLOW, AND PRESSURE TRANSIENT ANALYSIS

In order to investigate the applicability of the mathematical theory, outlined in Section 3.2, to analyze pressure transient data in the presence of nonlinear formation behavior and two-phase flow (liquid water with dissolved methane, free methane), the Systems, Science and Software (S^3) reservoir simulator MUSHRM (see Garg, et al. [1977]) was exercised in its one-dimensional radial mode to generate a series of drawdown/buildup histories. All of the cases described in

this section were simulated using a 22 zone (Δr_1 = 6 cm; Δr_2 = 11 cm; Δr_3 = 18 cm; Δr_4 = 29 cm; Δr_5 = 48 cm; Δr_6 = 78 cm; Δr_7 = 130 cm; Δr_8 = 215 cm; Δr_9 = 353 cm; Δr_{10} = 582 cm; Δr_{11} = 961 cm; Δr_{12} = 1,583 cm; Δr_{13} = 2,610 cm; Δr_{14} = 4,304 cm; Δr_{15} = 7,096 cm; Δr_{16} = 11,699 cm; Δr_{17} = 19,288 cm; Δr_{18} = 31,801 cm; Δr_{19} = 52,430 cm; Δr_{20} = 86,444 cm; Δr_{21} = 142,521 cm; Δr_{22} = 237,783 cm) radial grid; the reservoir extends from r = 10 cm to r = 6×10^5 cm. The use of fine zoning near the wellbore (nominal well radius r_0 = 10 cm) is necessary to circumvent the difficulties associated with the selection of an 'equivalent radius'. The reservoir boundaries (r = 10 cm and r = 6×10^5 cm) are assumed to be impermeable and thermally insulated; and the effect of mass withdrawal is represented by a volumetric sink term in the well-block (radial extent r = 10 cm to r = 16 cm). The latter procedure for representing mass withdrawal is tantamount to assuming an effective well radius of approximately 13 cm.

The reservoir rock is taken to be a sandstone with the following properties:

Rock grain density $\rho_r = 2.65$ gm/cm^3

Initial rock porosity = $\phi_0 = 0.2$

Rock grain thermal conductivity $\kappa_r = 5.25\ 10^5 \frac{\text{ergs}}{\text{sec-cm°C}}$

Rock heat capacity $c_r = 10^7$ ergs/gm°C

Compressibility $C_{mL} = 1.754 \times 10^{-10}$ cm^2/dynes

for $\frac{\partial p}{\partial t} < 0$

C_{mU} = variable (see Table 3.1)

for $\frac{\partial p}{\partial t} \geq 0$.

Absolute permeability k_0 (at $\phi = \phi_0$) = 0.2×10^{-9} cm^2

($\sim$ 20 md)

Formation thickness h = 5,000 cm.

Seven cases were treated (Table 3.1). In each case, changes in porosity ϕ with pore pressure are given by the relationship [Garg et al., 1977]

$$\frac{\partial \phi}{\partial t} = (1 - \phi_0)\, C_{mi}\, \frac{\partial p}{\partial t}\,, \quad i = L, U. \tag{3.11}$$

Except in Cases 3 and 4 discussed below, the permeability k is assumed to be independent of porosity ϕ; for these two cases, permeability is represented by the Carman-Kozeny relation

$$k = k_0 \left(\frac{\phi}{\phi_0}\right)^3 \left(\frac{1-\phi_0}{1-\phi}\right)^2 . \tag{3.12}$$

The pore fluid is assumed to be pure water in Cases 1-4 with initial pressure and temperature being 750 bars and 150°C respectively. In Cases 5-7, the pore fluid is assumed to be two-phase (liquid water with dissolved methane, free methane); the initial fluid state is given in Table 3.1. Since Cases 5-7 involve two-phase flow in the reservoir rocks, it is necessary to specify relative permeabilities for these cases. Corey equations are utilized to represent relative permeabilities in Cases 5 and 6.

$$R_\ell = \left(S^*_\ell\right)^4$$

$$R_g = \left(1 - S^*_\ell\right)^2 \left(1 - S^{*2}_\ell\right) \tag{3.13}$$

where

$$S^*_\ell = \left(S_\ell - S_{\ell r}\right) \Big/ \left(1 - S_{\ell r} - S_{gr}\right)$$

$$S_\ell = 1 - S$$

$$S_{\ell r} = 0.3,\ S_{gr} = 0.05.$$

TABLE 3.1

PARAMETERS USED IN A SERIES OF SEVEN CALCULATIONS MADE WITH THE MUSHRM SIMULATOR. RELATIVE PERMEABILITIES ARE NOT MEANINGFUL FOR CASES 1-4 IN WHICH RESERVOIR FLUID IS PURE WATER.

Case No.	Formation Properties				Initial Fluid State					Remarks
	Formation Compressibility		Permeability (absolute)	Relative Permeabilities	Pressure (bars)	Temperature (°C)	Methane Mass Fraction	Gas Volume Fraction	Fluid Compressibility 10^{10} C_f (cm^2/dynes)	
	10^{10} C_{mL} (cm^2/dynes)	$10^{10}C_{mU}$ (cm^2/dynes)								
1	1.754	1.754	$k(\phi) \equiv k(\phi_0)$	-	750	150	0	0	0.473	Base Case
2	"	0.877	$k(\phi) \equiv k(\phi_0)$	-	"	"	0	0	0.473	Same as Case 1 except C_{mU}.
3	"	1.754	Eq. (3.12)	-	"	"	0	0	0.473	Same as Case 1 except $k(\phi)$.
4	"	0.877	Eq. (3.12)	-	"	"	0	0	0.473	Same as Case 1 except C_{mU} and $k(\phi)$.
5	"	1.754	$k(\phi) \equiv k(\phi_0)$	Eq. (3.13)	"	"	0.0075	0.00576	0.624	Same as Case 1 except for presence of methane and two-phase flow.
6	"	1.754	$k(\phi) \equiv k(\phi_0)$	Eq. (3.13)	"	"	0.019	0.0489	0.906	Same as Case 5 except for the initial fluid state.
7	"	1.754	$k(\phi) \equiv k(\phi_0)$	Eq. (3.14)	"	"	0.006057	0.0001418	0.588	Same as Case 5 except for the initial fluid state and relative permeabilities.

Note that for $S_\ell < S_{\ell r}$, $R_\ell = 0$ and $R_g = 1$, and for $S_\ell > (1 - S_{gr})$ $R_\ell = 1$ and $R_g = 0$. For Case 7, the following relative permeability functions were utilized:

$$R_\ell = \left\{\frac{1 - S - S_{\ell r}}{1 - S_{\ell r}}\right\}^4 \text{ for } 1 - S > S_{\ell r}$$

$$= 0 \text{ otherwise}$$

$$R_g = S^2/(1 - S_{\ell r})^2 \text{ for } 1 - S > S_{\ell r} \qquad (3.14)$$

$$= 1 \text{ otherwise.}$$

The mass withdrawal rate is assumed to be 70 kg/sec (i.e., 14 gm/sec-cm) for $t < \sim 1800$ sec and 0 for $t > \sim 1800$ sec.

Cases 1-4 were designed to assess the effects of (1) changes in reservoir permeability as a result of formation compaction and (2) irreversible pore collapse. In Case 1 (base case), the formation is assumed to exhibit identical compaction behavior during loading and unloading, and the permeability is taken to be independent of porosity; note that these are exactly the assumptions involved in deriving Eqs. (3.2), (3.3) and (3.5). The drawdown and buildup data for this case are shown in Figures 3.1a and 3.1b respectively; the permeability values (18.9×10^{-11} cm^2 and 19.3×10^{-11} cm^2) inferred (assuming h = 5,000 cm; M = 70 kg/sec, $\rho = 0.954$ gm/cm^3, $\mu = 0.198\ 10^{-2}$ poise) are in reasonable agreement with the actual value of 20×10^{-11} cm^2. At least a part of the difference between the inferred and actual values is caused by changes in porosity (ϕ) and hence formation thickness h during drawdown/buildup. For example, during drawdown, porosity changes from 0.2 at t = 0 sec to 0.184 at $t \sim 1800$ sec;

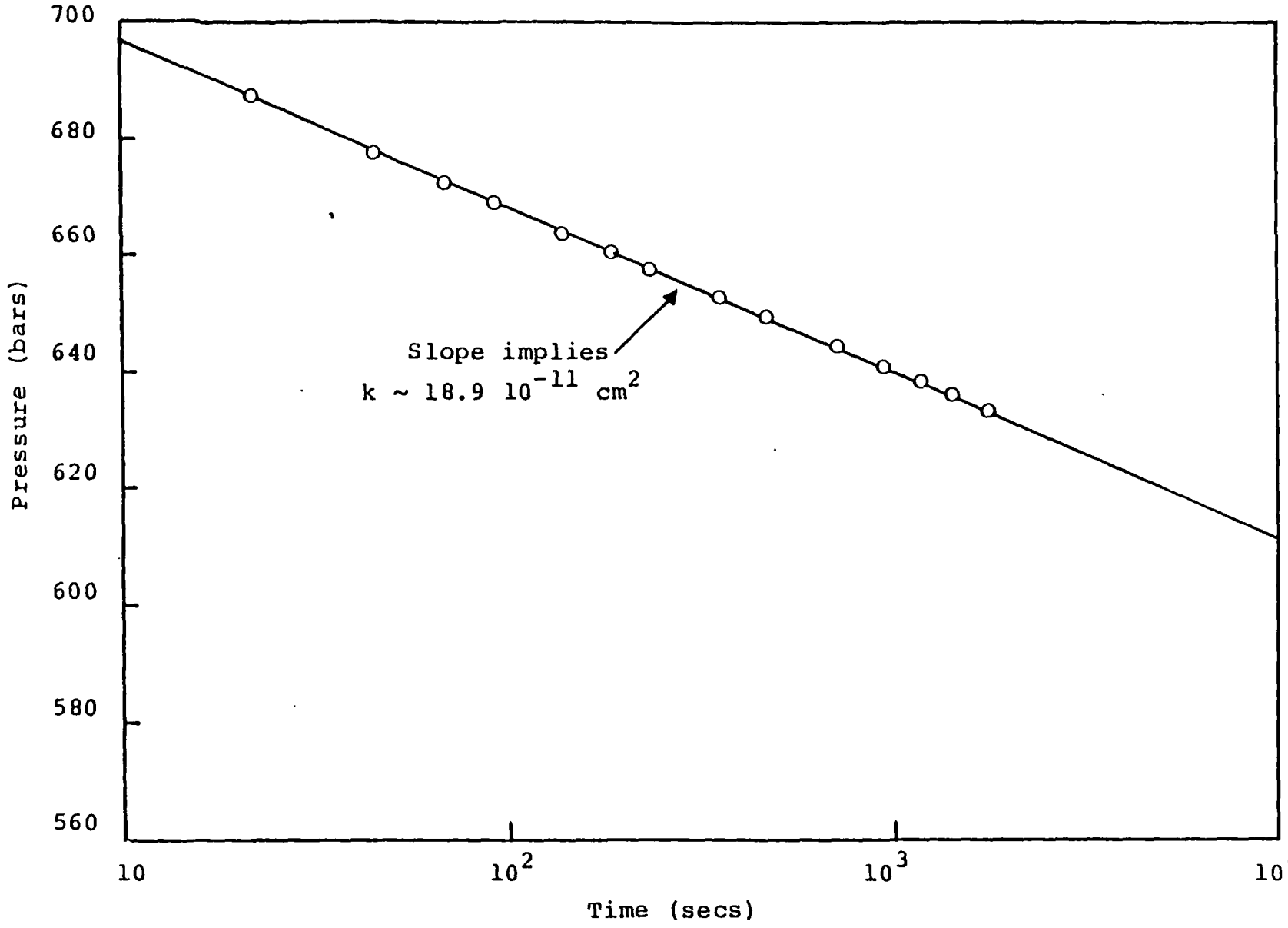

Figure 3.1a. Drawdown history for Case 1.

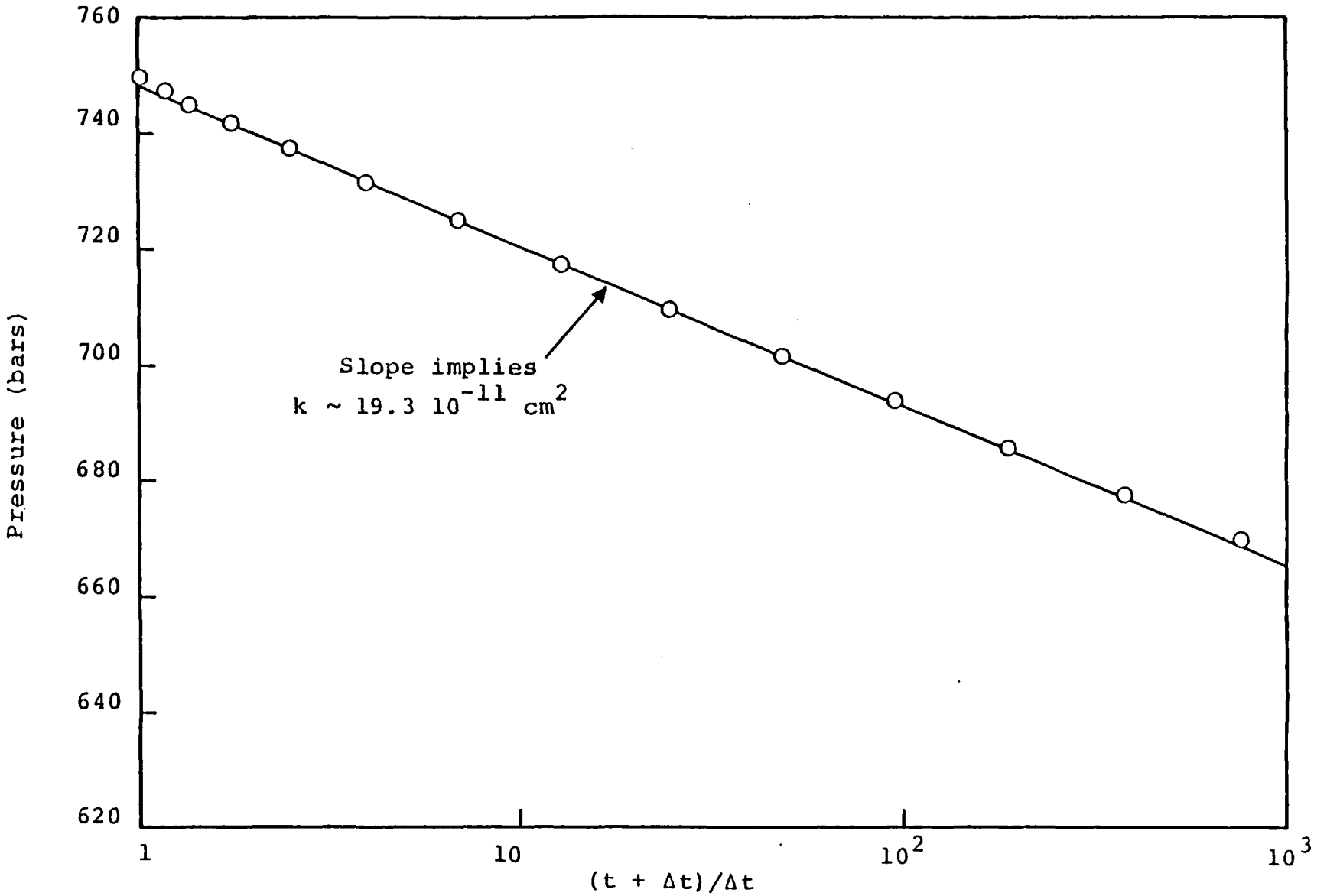

Figure 3.1b. Buildup history for Case 1b.

this implies that h ($\Delta h/h = \Delta\phi/1-\phi$) decreases by approximately 2 percent. As remarked earlier, given k, Eq. (3.3) may be utilized to determine the total compressibility; the value of total compressibility obtained in this manner ($\sim 7.95\ 10^{-10}$ cm^2/dynes) is also in satisfactory agreement with the actual value of $7.49\ 10^{-10}$ cm^2/dynes. Extrapolation of the straight line in Figure 3.1b to $t + \Delta t/\Delta t = 1$ yields $p^* \sim 748$ bars; the slight difference between p^* and p_i (= 750 bars) is due to the inapplicability of the semi-log approximation in the vicinity of $(t + \Delta t)/t = 1$. It is also worth noting here that the buildup data lie above the straight line as $(t + \Delta t)/\Delta t \to 1$.

Formation compaction exhibits irreversible behavior ($C_{mL} \neq C_mU$) in Case 2. The drawdown phase of Case 2 is identical with that of Case 1; once again the inferred values for permeability k (19.6×10^{-11} cm^2) and compressibility C_{TL} (6.75×10^{-10} cm^2/dynes) from the slope of the straight line (Figure 3.2a) and Eq. (3.3) are in good agreement with the actual values. The buildup behavior for this case is illustrated in Figure 3.2b; the slope of the straight line yields a permeability value of 19.1×10^{-11} cm^2. The buildup curve of Figure 3.2b differs in one essential respect from that of Figure 3.1b; the buildup pressures now approach p_i as $(t + \Delta t)/\Delta t \to 1$ from below the straight line. Extrapolation of the straight line to $(t + \Delta t)/\Delta t = 1$ yields $p^* = 755.3$ bars ($> p_i$). Substituting numerical values for p^* and p_i into Eq. (3.7), we obtain $C_{TL}/C_{TU} \sim 1.6$ (the actual value is ~ 1.9). The lack of good agreement between the calculated and actual values for C_{TL}/C_{TU} is not surprising in view of the assumptions invoked in deriving Eq. (3.7) (i.e., (1) applicability of semi-log approximation in the neighborhood of $t + \Delta t/\Delta t = 1$, (2) use of C_{mU} to characterize formation compaction during buildup), and the relatively small value of C_{mL}/C_{mU} in this case. The agreement between the inferred and actual values for C_{TL}/C_{TU} may be expected to improve with increasing C_{mL}/C_{mU} as this

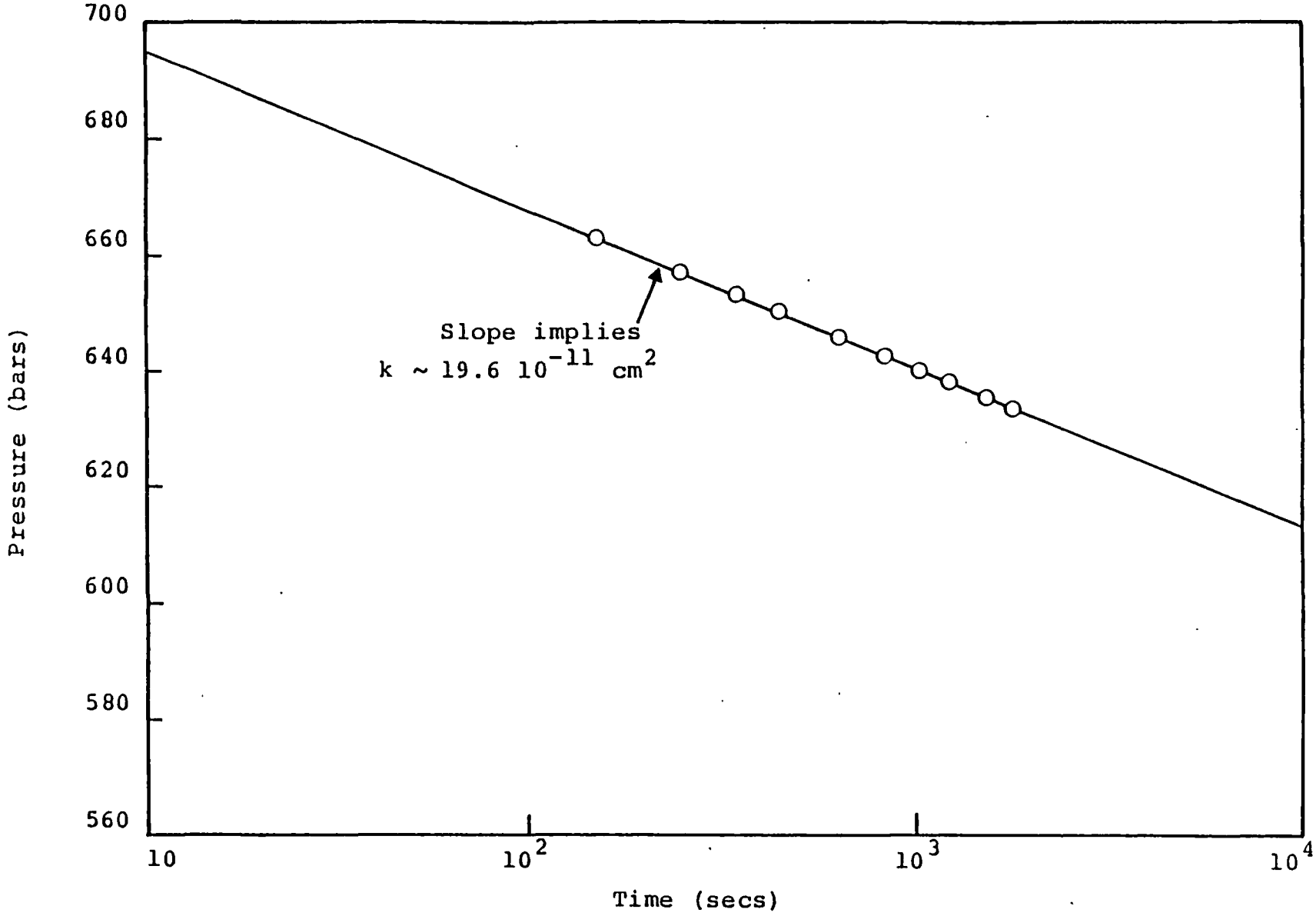

Figure 3.2a. Drawdown history for Case 2.

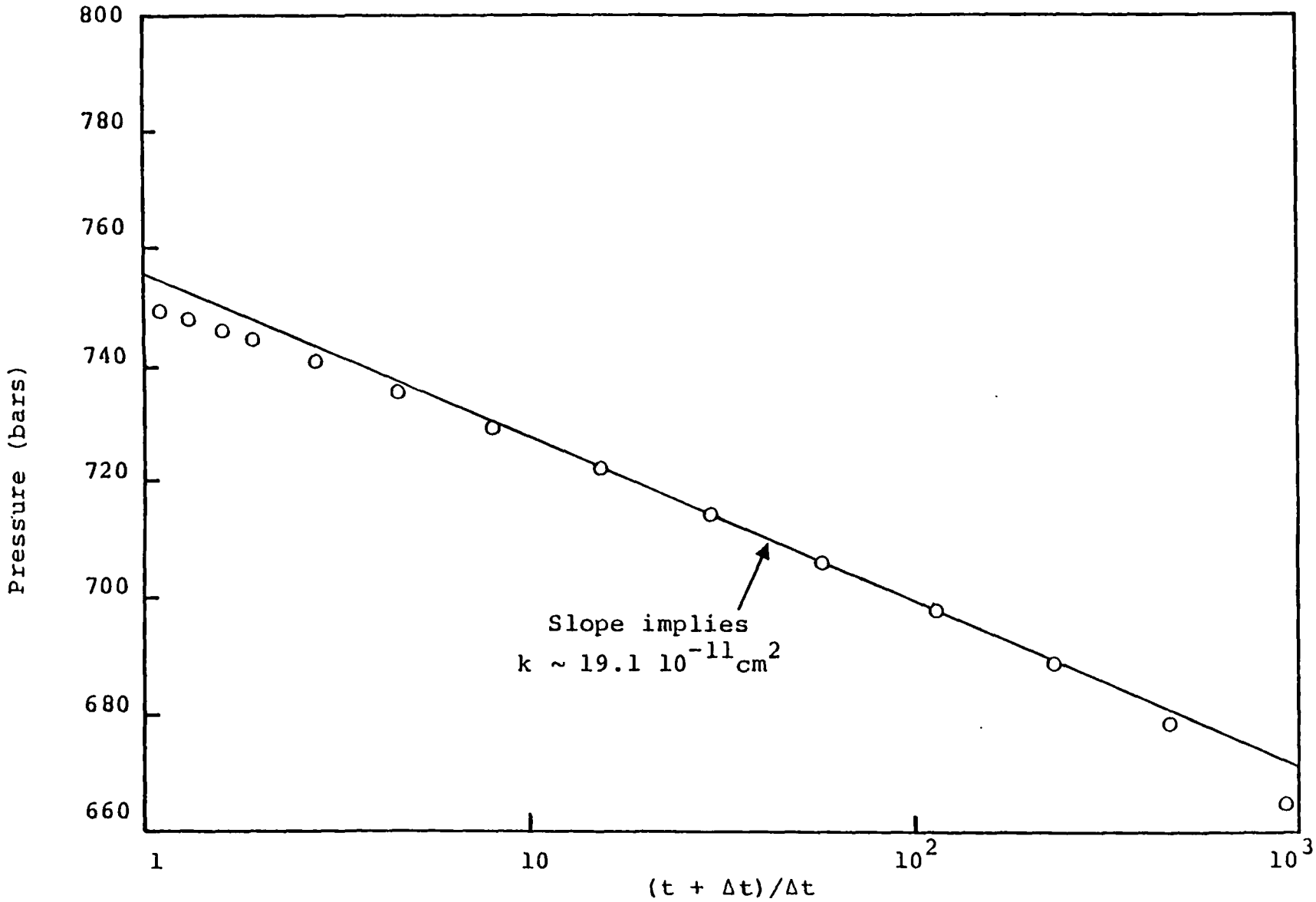

Figure 3.2b. Buildup history for Case 2.

would minimize the inaccuracies involved in using C_{mU} to represent the compaction behavior during buildup. In any event appearance of a p* greater than p_i is indicative of irreversible compaction behavior.

In Case 3, formation permeability is assumed to change with porosity. Drawdown and buildup data are plotted in Figures 3.3a and 3.3b respectively. It is apparent from these figures that no unique straight line exists in this case; as a matter of fact, several straight lines may be drawn depending upon one's choice of data points. This is really not surprising in view of the fact that permeability changes significantly during the test. The permeabilities obtained from the straight lines (Figures 3.3a and 3.3b) are in fair agreement with the actual well-block values at appropriate times (corresponding to the mid-point of the straight line), and may be utilized to construct the permeability-pore pressure relationship. Table 3.2 shows the inferred values of permeability as a function of pore pressure; for comparison purposes, we also give the calculated values of permeability (c.f., Eqs. (3.11) and (3.12)).

It is clear from Table 3.2 that even when the permeability changes during the test, it is possible to infer its value with fair accuracy from drawdown and buildup data. Unfortunately, such is not the case for the total compressibility C_T. Calculated values for C_T from the slope of the straight lines (Figure 3.3a) and Eq. (3.3) are 11.8 10^{-10} cm^2/dynes and 25.4 10^{-10} cm^2/dynes; these values are much larger than the actual value of 7.49 10^{-10} cm^2/dynes. This implies that in case the permeability is a function of porosity (and hence pore pressure), the use of classical techniques to estimate reservoir storativity ϕC_T h would lead to too high values.

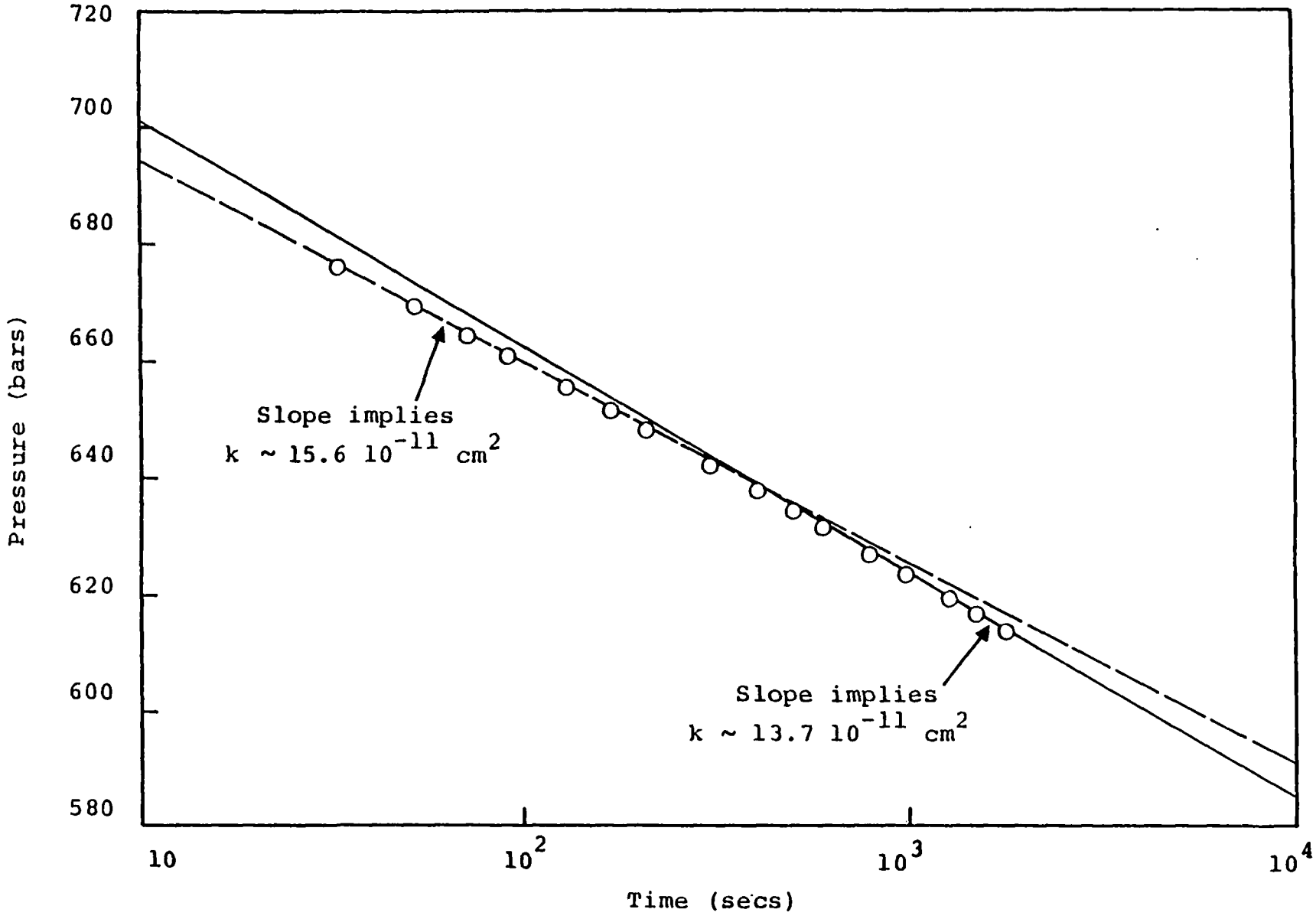

Figure 3.3a. Drawdown history for Case 3.

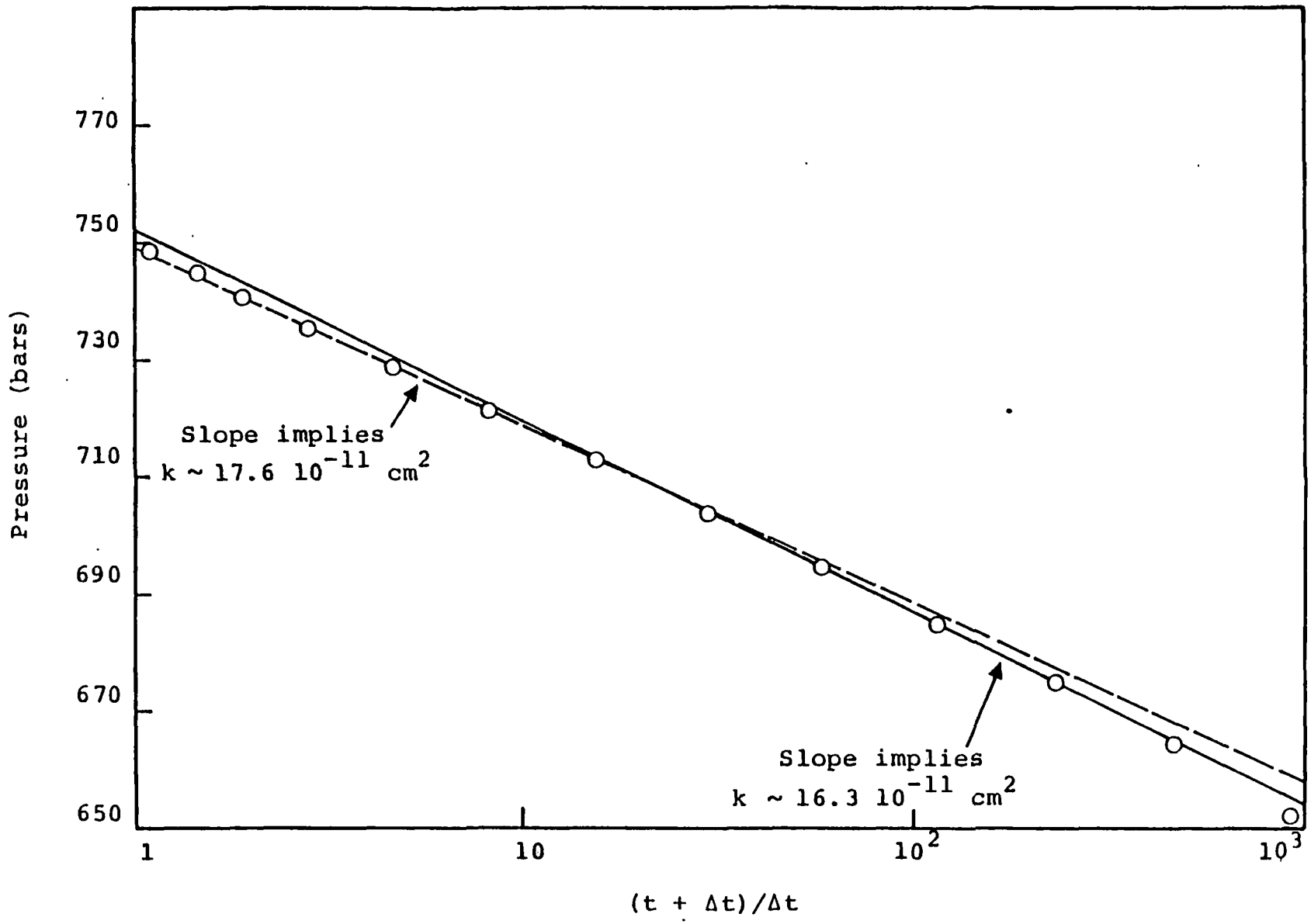

Figure 3.3b. Buildup history for Case 3.

TABLE 3.2

PRESSURE-DEPENDENCE OF PERMEABILITY

Pore Pressure (bars)	Permeability $10^{11}k$ (cm^2)	
	Inferred	Calculated (Eqs. (3.11) and (3.12))
620	13.7	14.3
666	15.6	16.2
692	16.3	17.3
728	17.6	18.9

Combined effects of pressure dependence of permeability and irreversible formation compaction are investigated in Case 4. As might be expected, the drawdown behavior (Figure 3.4a) is similar to that of Case 3; the permeability values obtained from the slope of the straight lines (16.1×10^{-11} cm^2 and 15.0×10^{-11} cm^2) are representative of well-block values. The compressibility C_T values, like in Case 3, are much larger (11.0×10^{-10} cm^2/dynes and 23.3×10^{-10} cm^2/dynes) than the actual value (7.49×10^{-10} cm^2/dynes). The buildup behavior for this case is shown in Figure 3.4b. The straight line drawn through points corresponding to large values of $(t + \Delta t)/\Delta t$ yields $k \sim 15.4 \times 10^{-11}$ cm^2 (actual value $\sim 17.3 \times 10^{-11}$ cm^2), $p^* = 763.6$ bars, and $C_{TL}/C_{TU} \sim 2.5$ (actual value ~ 1.9). Once again, the appearance of a $p^* > p_i$ can be used to diagnose irreversible formation compaction. The straight line passing through points for large buildup times, however, gives anomalous values for permeability (21.0×10^{-11} cm^2 against actual value of 18.3×10^{-11} cm^2) and p^* (751.6 bars). Use of the latter value for p^* would indicate little or no irreversible compaction. The selection of the proper straight line portion is thus of critical importance in analyzing buildup data. Based on the analysis of the cases examined here, it appears that the straight line segment for intermediate values of $(t + \Delta t)/\Delta t$ ($\sim 5 < (t + \Delta t)/\Delta t < \sim 200$ is likely to give the most reliable information.

The pore fluid in Cases 5-7 is two-phase (i.e., liquid water with dissolved methane and free methane gas). These cases were run to investigate the effects of (1) the presence of free methane in the pores and (2) the use of different relative permeability functions. In all of these cases, the free gas, initially immobile, becomes mobile during the simulated test; however, most of the production comes from the liquid phase such

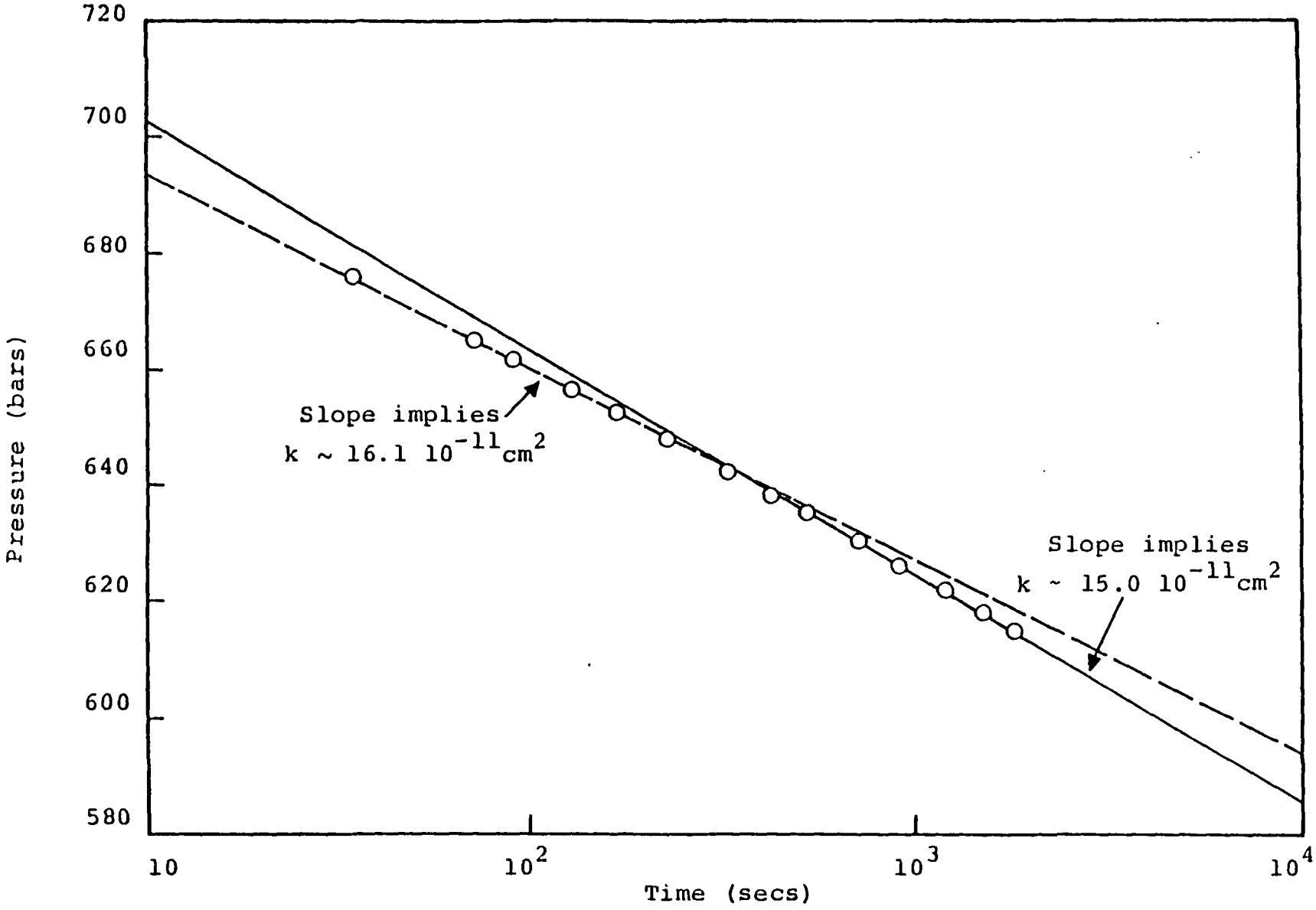

Figure 3.4a. Drawdown history for Case 4.

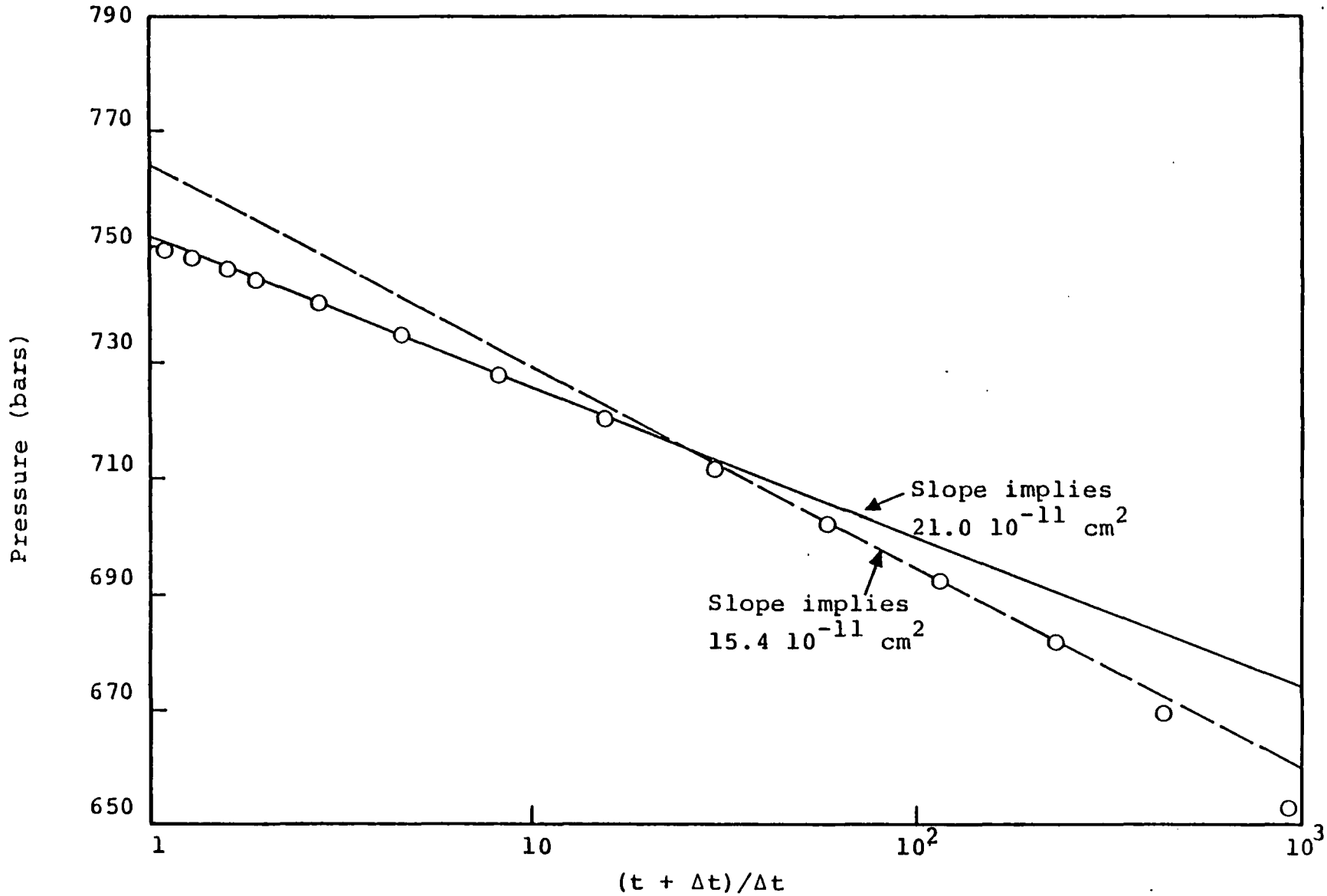

Figure 3.4b. Buildup history for Case 4.

that $q_T \sim q_\ell$ and $(k/\mu)_T \sim (k/\mu)_\ell$. As a result of production, (and consequent pressure drop), the gas volume fraction goes up in the pores (Case 5; from S = 0.00576 at t = 0 to S = 0.067 at t ∿ 1760 sec; Case 6: from S = 0.0489 at t = 0 to S = 0.0738 at t ∿ 1800 sec; Case 7: from S = 0.0001418 at t = 0 to S = 0.0092637 at t ∿ 1730 sec); the main effect of this increase in gas saturation is to decrease the liquid (and total) mobility without substantially increasing the gas mobility. Drawdown histories for these cases are shown in Figures 3.5 - 3.7. The total mobilities calculated from the slope of the straight lines are in good agreement with the actual range of mobility values (Figures 3.5 - 3.7). Case 6 is especially interesting in so far as it is possible to draw at least two straight lines (this is not unlike Cases 3 and 4 wherein permeability was assumed to vary with porosity). The compressibilities obtained from the slope of the straight lines and Eq. (3.3) for Cases 5 and 7 (7.6×10^{-10} cm^2/dynes and 8.2×10^{-10} cm^2/dynes) compare favorably with the actual values (7.6×10^{-10} cm^2/dynes and 7.6×10^{-10} cm^2/dynes). The inferred compressibility values for case 6 (9.6×10^{-10} cm^2/dynes and 12.7×10^{-10} cm^2/dynes), however, display poor agreement with the actual value (7.9×10^{-10} cm^2/dynes). This latter result is in agreement with out earlier remark (c.f., discussion of Cases 3 and 4) that whenever permeability changes substantially during the test, the calculated compressibility (and hence storativity) values will be in error.

3.5 EQUIVALENT RADIUS AND SIMULATION OF WELL TESTS

In the parametric calculations presented in Section 3.4 we utilized fine zoning near the wellbore to avoid ambiguities associated with the definition of an 'equivalent radius' (c.f., Section 3.3). The use of fine zoning near the wellbore imposes severe restrictions on the allowable time step in the computer calculations. Since well tests are usually run for several

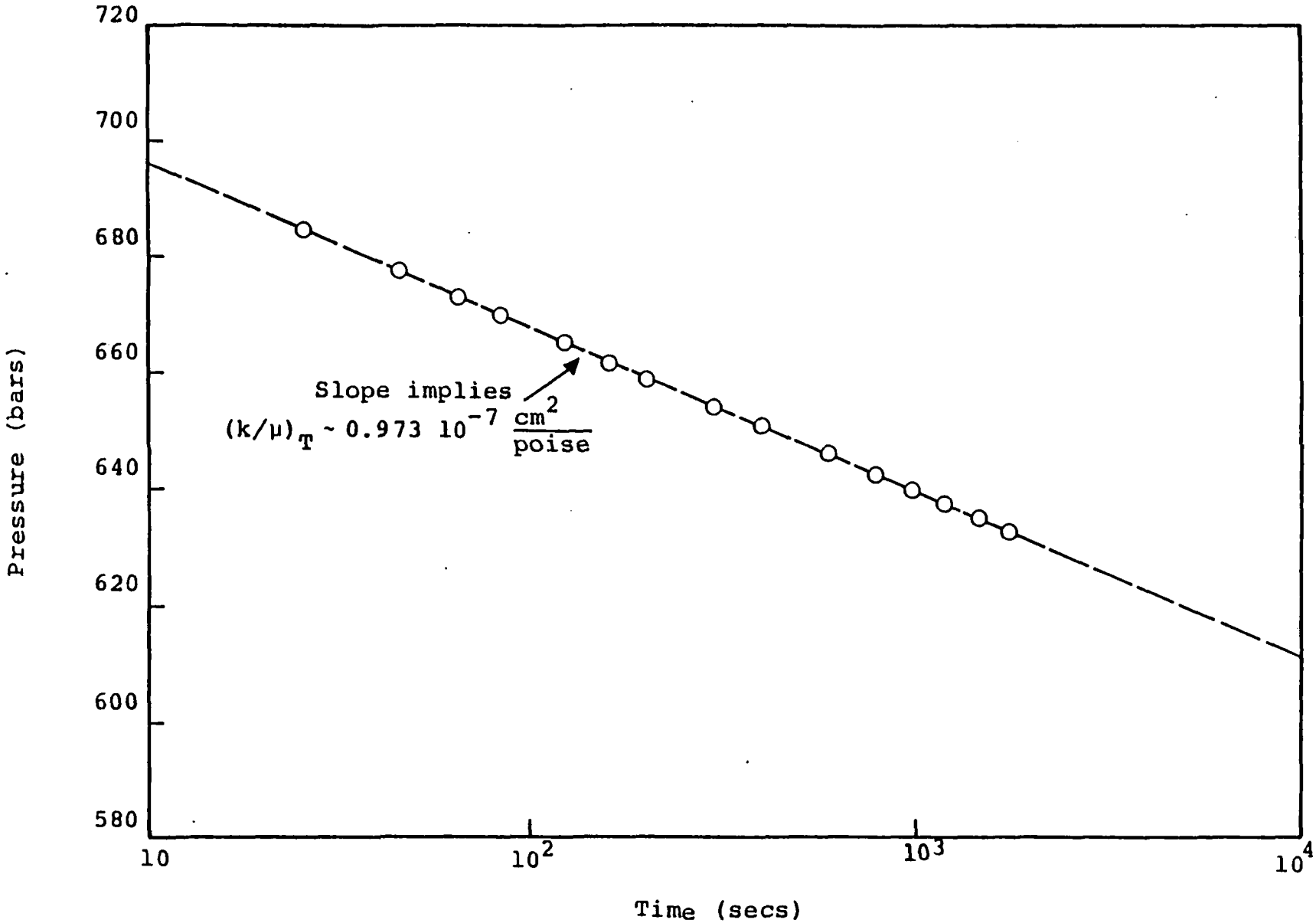

Figure 3.5. Drawdown history for Case 5. Most of the fluid production comes from the liquid phase such that $q_T \sim q_\ell$ and $(k/\mu)_T \simeq (k/\mu)_\ell$; $(k/\mu)_T$ changes from $1.01\ 10^{-7}$ cm^2/poise at t = 0 to $0.926\ 10^{-7}$ cm^2/poise at t ~ 1760 sec.

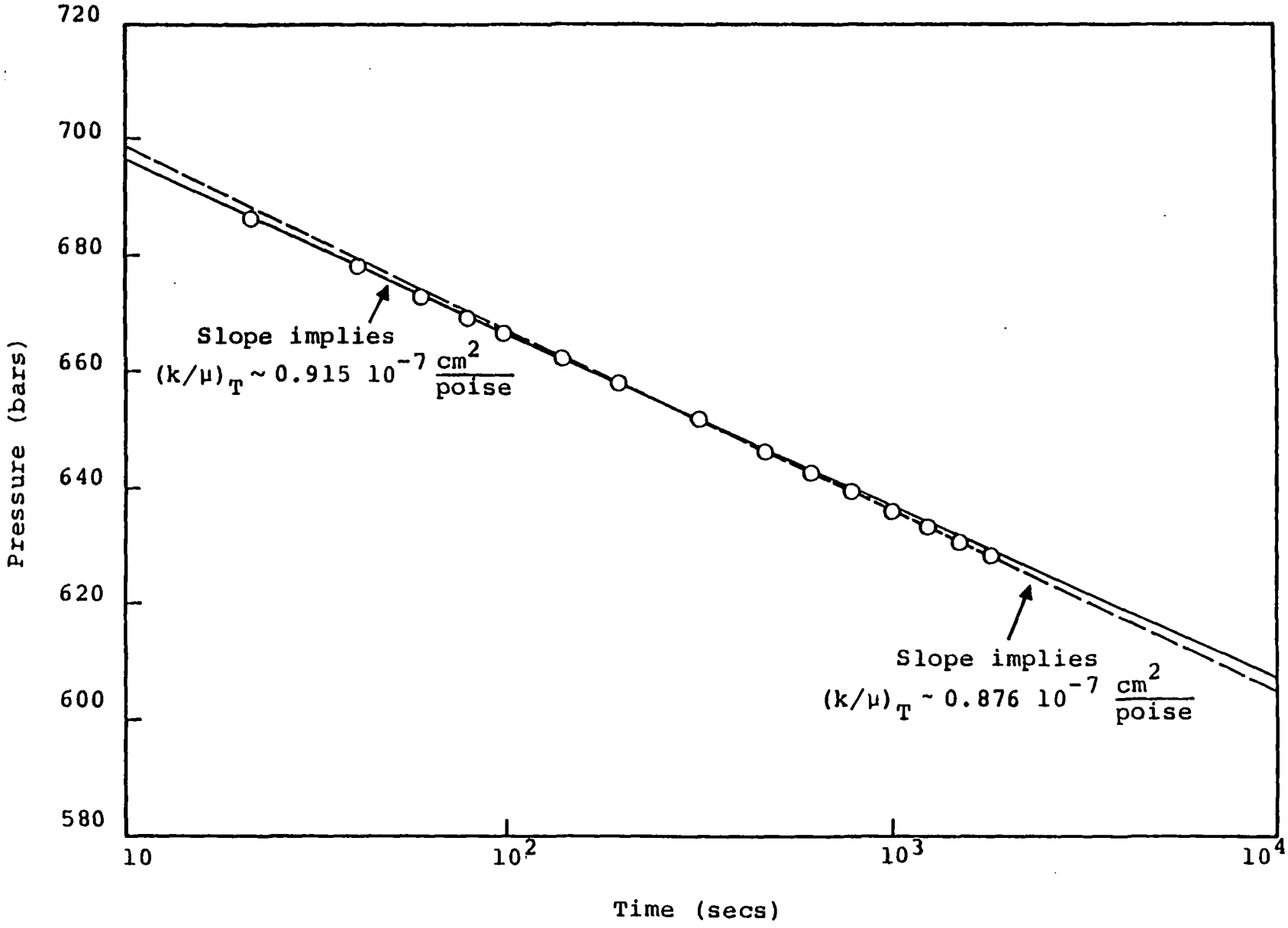

Figure 3.6. Drawdown history for Case 6. Most of the fluid production is from the liquid phase such that $(k/\mu)_T \sim (k/\mu)_\ell$; $(k/\mu)_T$ changes from 1.01 10^{-7} cm^2/poise at t = 0 to 0.887 10^{-7} cm^2/poise at t ~ 1800 sec.

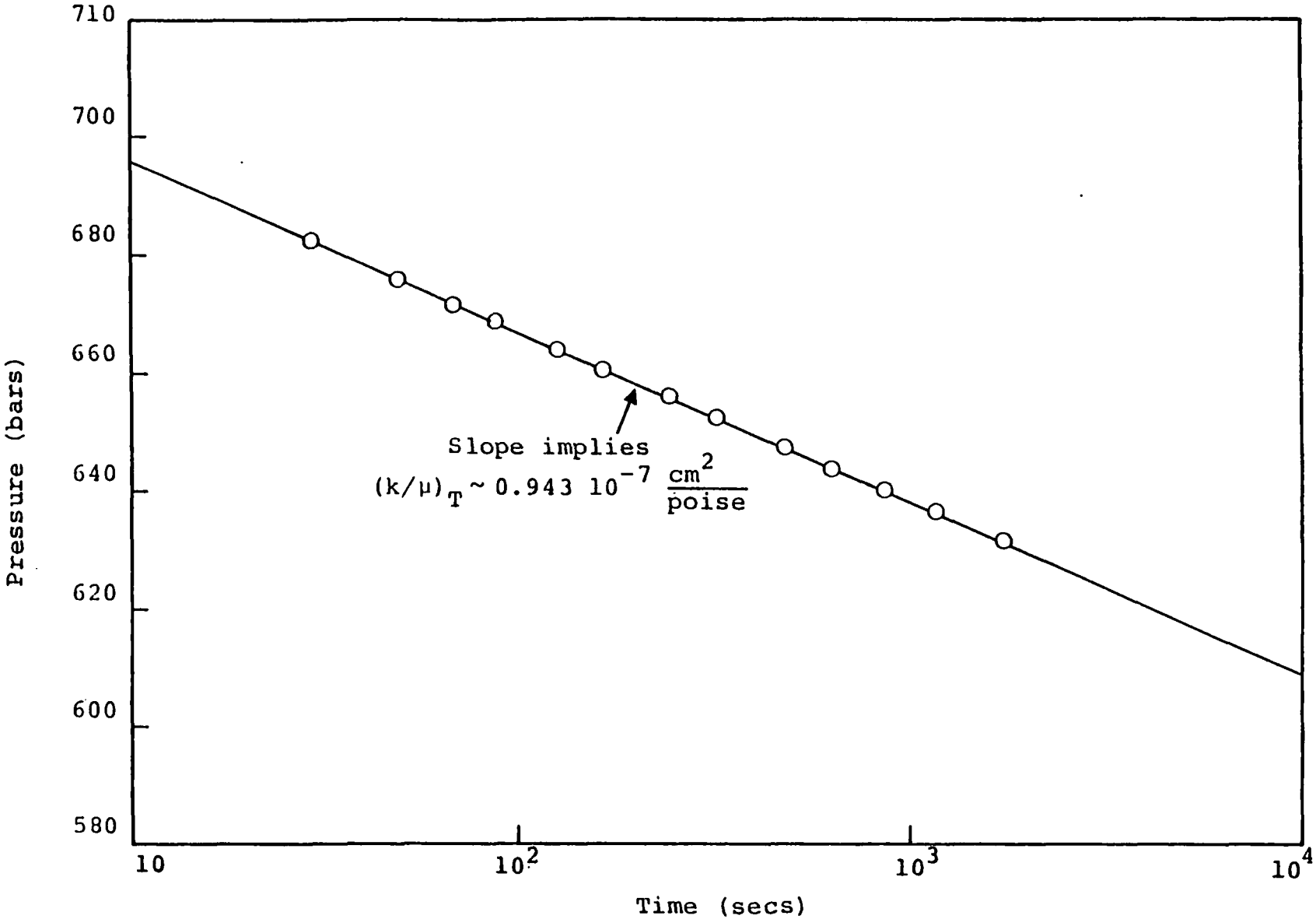

Figure 3.7. Drawdown history for Case 7. Most of the fluid production is from the liquid phase such that $(k/\mu)_T \sim (k/\mu)_\ell$; $(k/\mu)_T$ changes from 1.01 10^7 cm^2/poise at t = 0 to 0.982 10^{-7} cm^2/poise at t ~ 1730 sec.

hours (or even days), use of small time steps would make the simulation of well tests very expensive. Practical considerations, therefore, make it necessary to employ well-blocks (i.e., a grid block containing a well) with dimensions much larger than the well radius; this, of course, brings us back to the question of an 'equivalent well radius'.

We shall now present a series of three drawdown/buildup histories (Cases 8-10) generated by using an eleven zone radial grid (Δr_1 = 100 cm, Δr_2 = 140 cm, Δr_3 = 330 cm, Δr_4 = 780 cm, Δr_5 = 1,900 cm, Δr_6 = 4,500 cm, Δr_7 = 10,750 cm, Δr_8 = 25,600 cm, Δr_9 = 60,900 cm, Δr_{10} = 146,000 cm, Δr_{11} = 349,000 cm). The reservoir extends from r = 0 to r = 6×10^5 cm, and the well is assumed to be located in the first zone ($0 < r < \Delta r_1$); the drawdown time is 0.6068×10^6 sec.

Formation properties, initial fluid state, and mass production rate for Case 8 are identical with those of Case 1 (Section 3.4). Both the drawdown and buildup straight lines (Figures 3.8a and 3.8b) yield a permeability of 18×10^{-11} cm^2; The difference between the latter and the actual value (20×10^{-11} cm^2) is once again, at least in part, attributable to a reduction in formation porosity (from 0.2 to 0.177) and hence thickness ($\Delta h/h \sim 3$ percent). Given p_i (= 750 bars), $p_w(t)$ ($\sim$ 581.2 bars at $t \sim 10^6$ sec from the straight line in Figure 3.8a), ϕ (= 0.2), C_T (= 7.49 10^{-10} cm^2/dynes), and fluid viscosity μ (= 0.198 10^{-2} poise), Eq. (3.3) may be solved to yield equivalent radius r_w. For the present case, this gives $r_w \sim$ 56.2 cm; note that the calculated value for r_w is in good agreement with the value for r_w (for uniform radial mesh) given in Section 3.3. The latter observation provides a sort of justification for the use of equivalent radii values calculated on the basis of steady-flow (and uniform mesh) in calculations involving transient flow (with both uniform and stretch meshes).

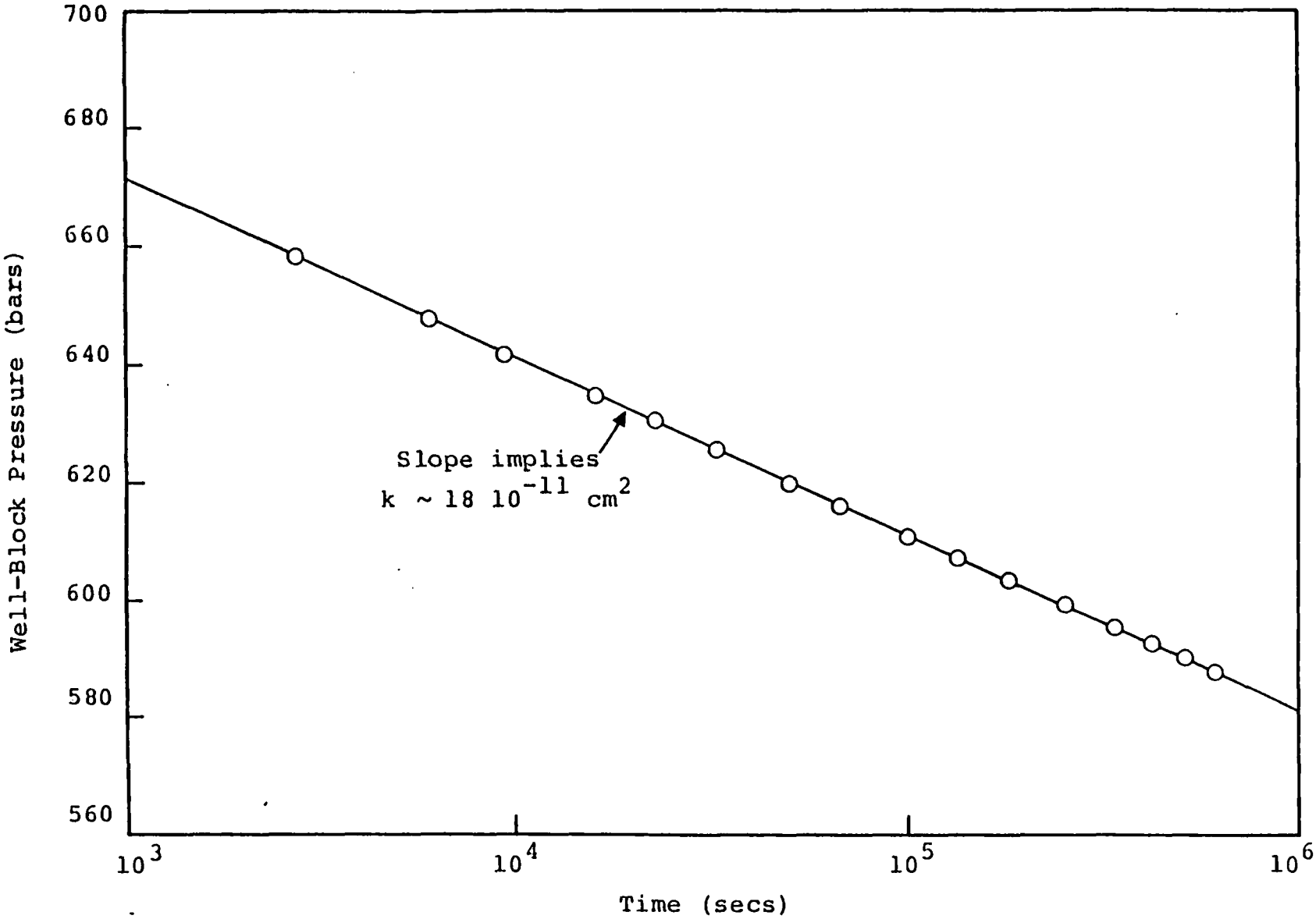

Figure 3.8a. Drawdown history for Case 8.

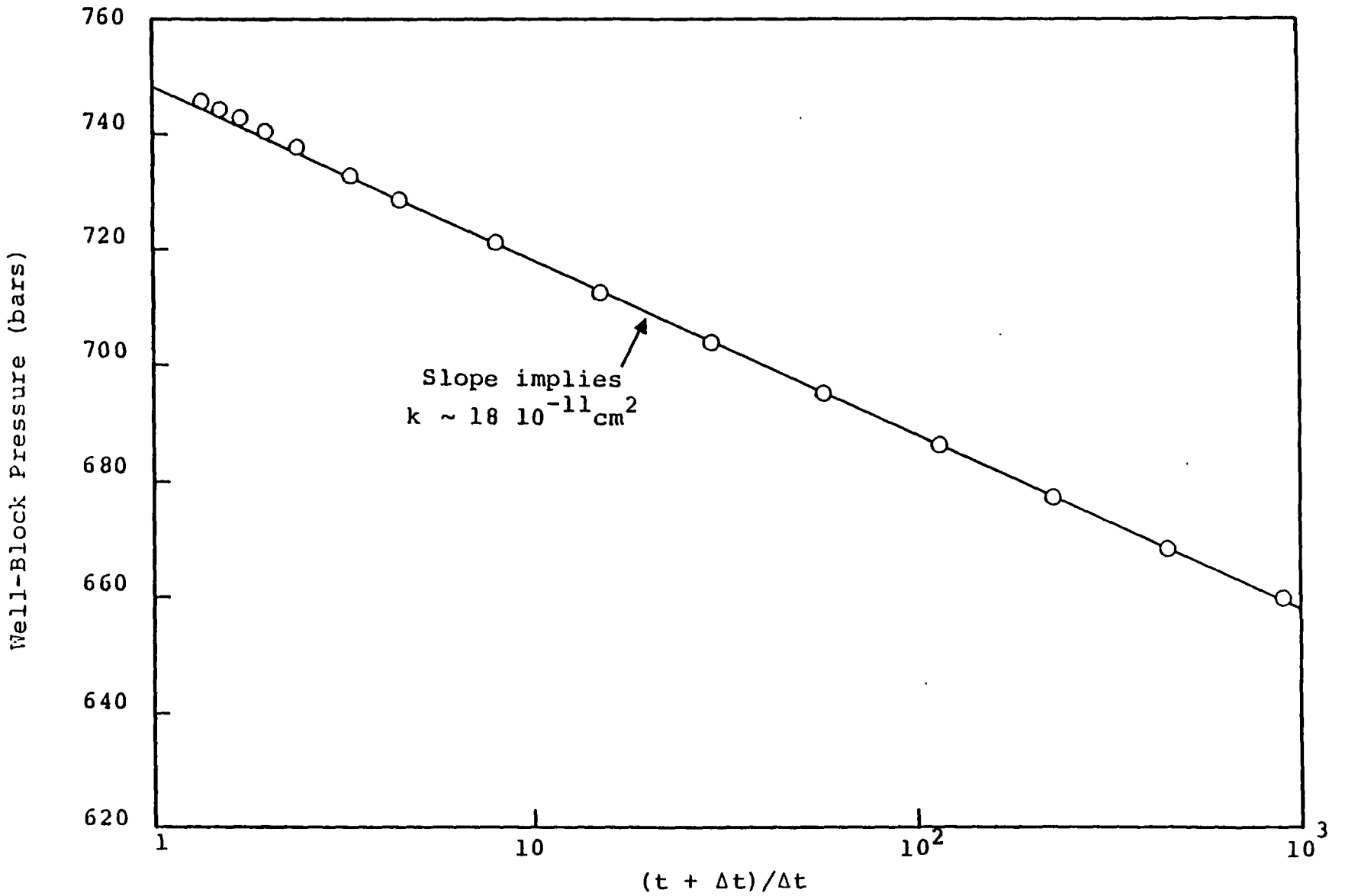

Figure 3.8b. Buildup history for Case 8.

The formation (except $C_{mU} = 1.754\ 10^{-11}$ cm^2 dynes = 0.1 C_{mL}) and fluid parameters used as input for Case 9 are the same as Case 2. Both the drawdown and buildup curves (Figures 3.9a and 3.9b), like Case 8, yield $k \sim 18 \times 10^{-11}$ cm^2. Proceeding as in Case 8, we obtain an equivalent radius r_w of 51.9 cm. The buildup curve yields $p^* = 770$ bars ($> p_i$); this together with Eq. (3.7) gives $C_{TL}/C_{TU} \sim 4.8$ (the actual value is ~ 6.3). The agreement between the inferred and actual values for C_{TL}/C_{TU} is considerably better in this case than that obtained for Case 2; as we remarked earlier an increase in C_{mL}/C_{mU} will lead to more accurate estimates of C_{TL}/C_{TU} from the buildup data.

Case 10 has the same formation and fluid parameters as those for Case 6. The drawdown and buildup histories are plotted in Figures 3.10a and 3.10b respectively. Like Case 6, it is possible to draw more than one straight line through the drawdown/buildup data; the values of total mobility inferred from the various straight line segments (Figures 3.10a and 3.10b) are in fair agreement with the actual range of values. Assuming $r_w \sim 56$ cm, the two straight line segments in Figure 3.10a give $C_T = 11.0 \times 10^{-10}$ cm^2/dynes and 30.0×10^{-10} cm^2/dynes; both of these values are much higher than the actual value (7.9×10^{-10} cm^2/dynes). In view of the fact that the inferred value of C_T is a strong function of the straight line segment (i.e., production time) and also taking into consideration the results of Case 6, it is likely that the observed difference between the calculated and actual value of C_T is not due to a possibly improper application of single-phase r_w to the present two-phase problem. This does not, of course, imply that the single-phase equivalent radius is the correct one for

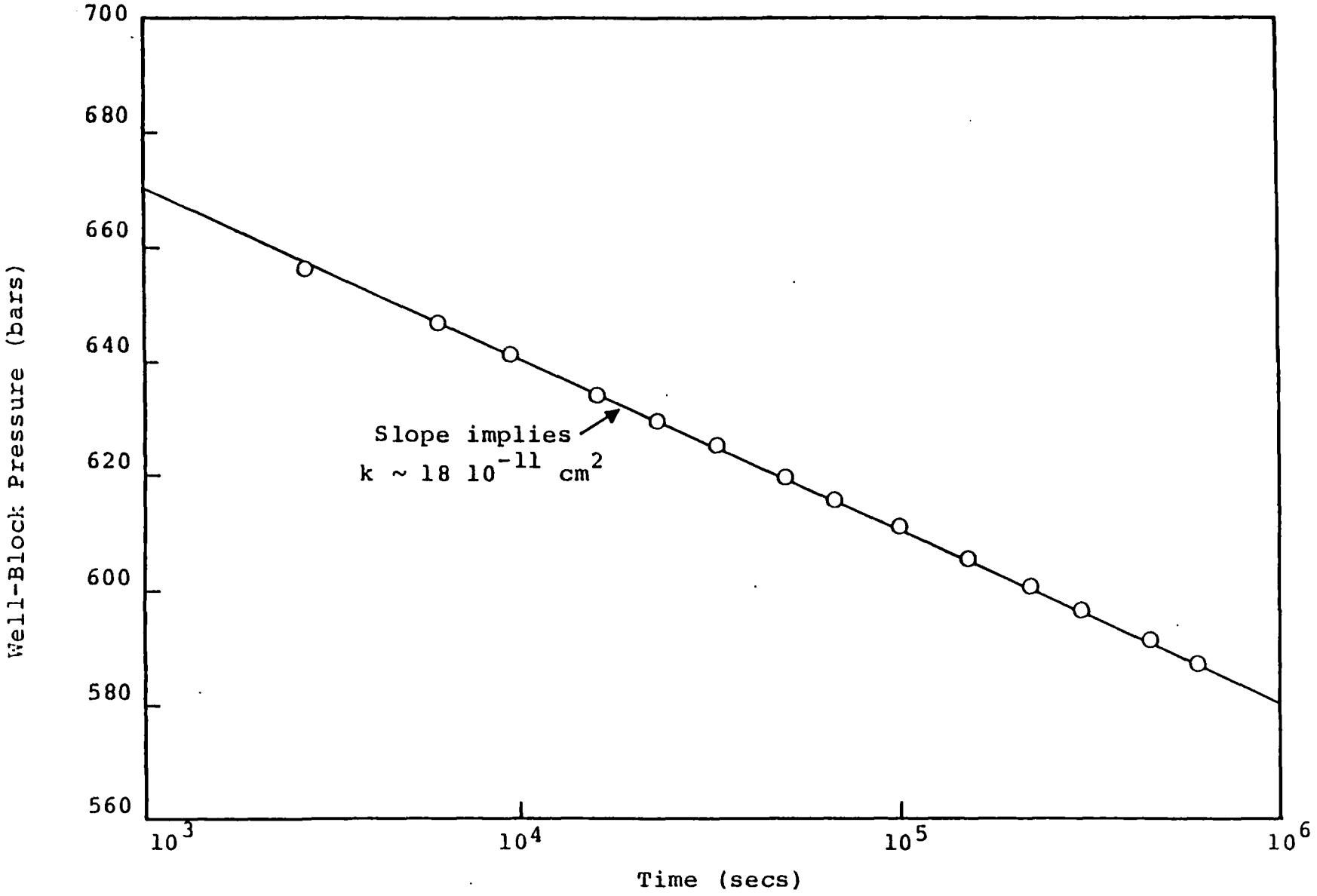

Figure 3.9a. Drawdown history for Case 9.

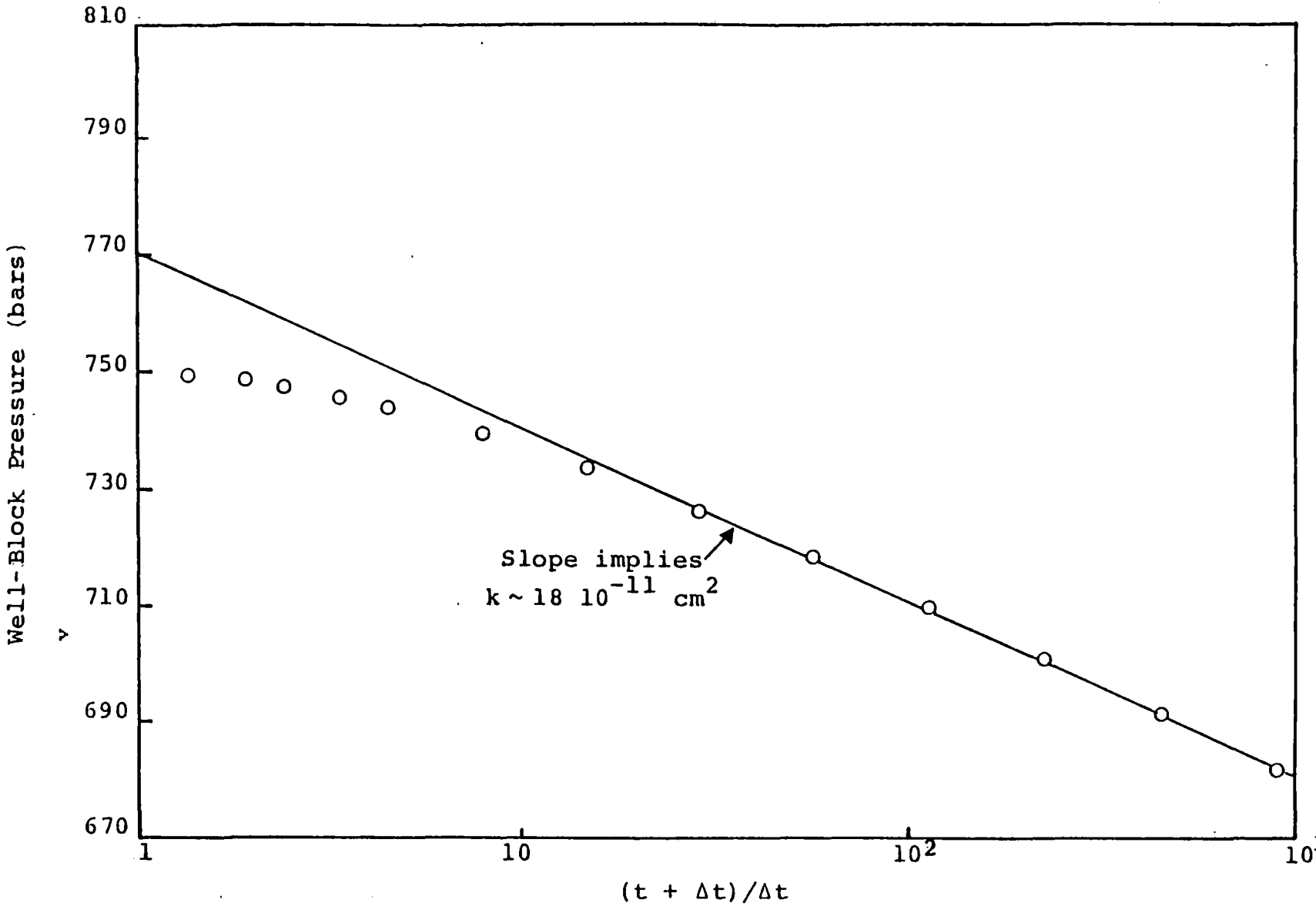

Figure 3.9b. Buildup history for Case 9.

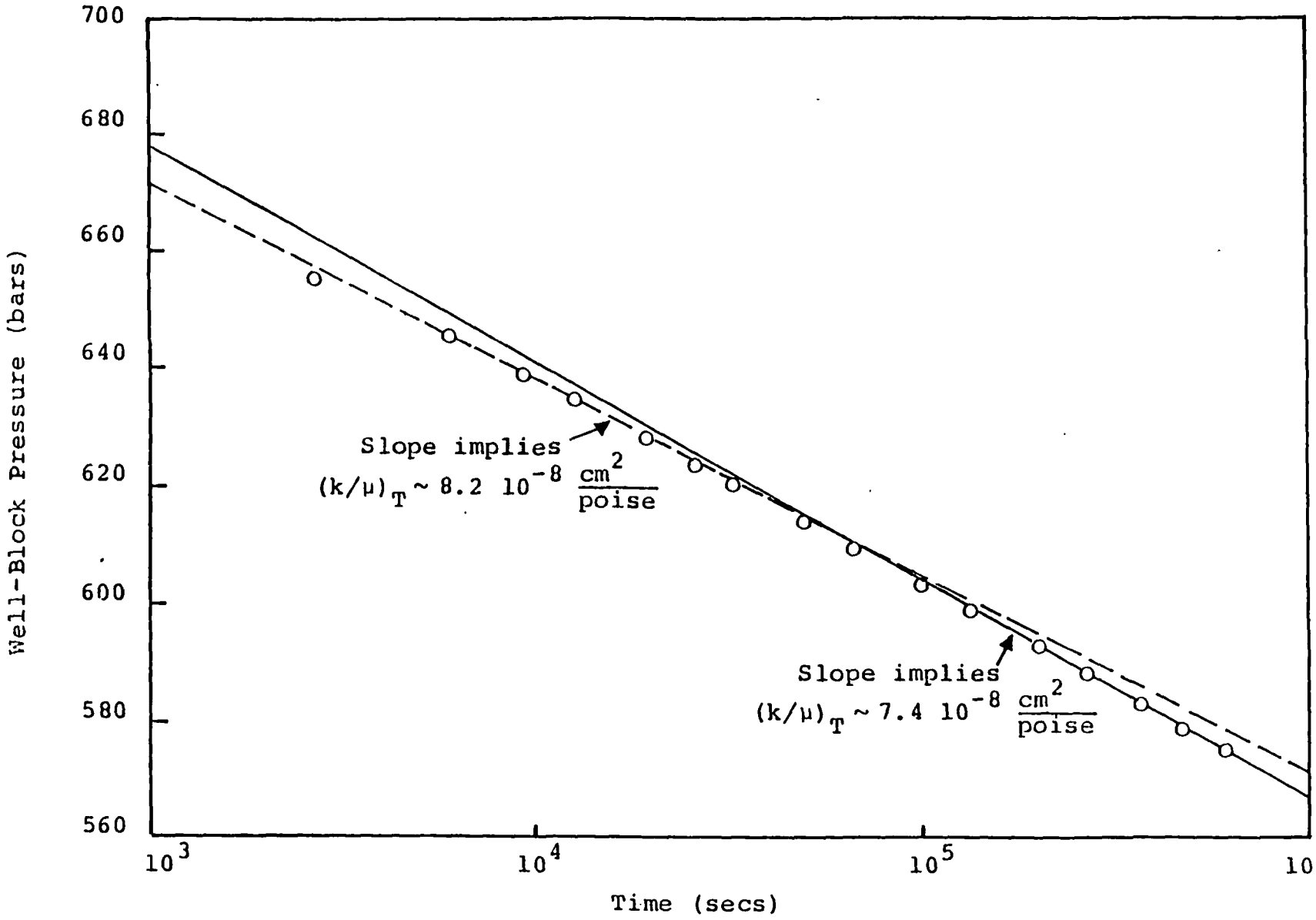

Figure 3.10a. Drawdown history for Case 10. Most of the fluid production is from the liquid phase such that $(k/\mu)_T \sim (k/\mu)_\ell$; $(k/\mu)_T$ changes from 1.01 10^{-7} cm^2/poise at t = 0 to 0.852 10^{-7} cm^2/poise at 0.6068 10^6 sec.

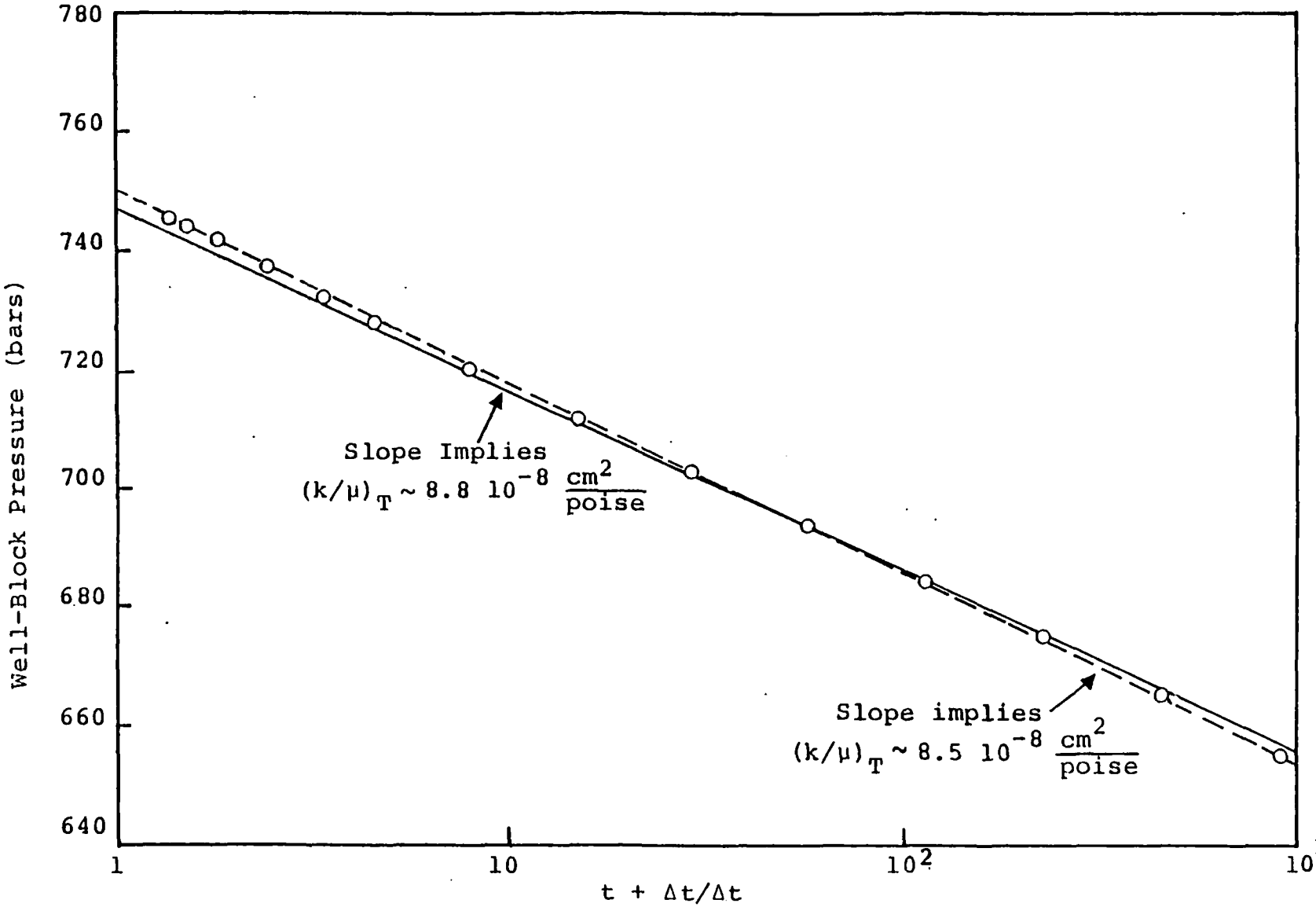

Figure 3.10b. Buildup history for Case 10.

the two-phase case. Unfortunately, in the two-phase case, unlike the single-phase case, there does not appear to be any simple way of calculating the correct r_w. Therefore, most workers in reservoir simulation at present use the single-phase r_w in two-phase problems as well (see also Peaceman [1977]).

3.6 SUMMARY AND CONCLUSIONS

The main purpose of this section was to (1) assess the applicability of conventional well test interpretation techniques to geopressured systems, and (2) to determine the relationship between the simulator calculated well-block pressures and the actual flowing pressures. A series of parametric calculations (Section 3.4) simulating well drawdown/buildup tests was performed to assess the effects of formation compaction and methane saturation (and the associated changes in absolute permeability and/or total mobility). It was found that conventional well test analysis may be expected to yield reliable formation permeability (or mobility) data even when compaction occurs and methane evolves out of solution, but storativity estimates will be unreliable. Drawdown and buildup test data together can be used to diagnose irreversible compaction response of the formation. Comparison of the numerical solution for transient, slightly compressible single-phase flow into a single well with the analytical solution (Section 3.5) shows that the equivalent radius (i.e., the radius at which the calculated well-block pressure is equal to the actual flowing pressure) in transient flow is closely approximated by the equivalent radius computed on the basis of steady flow (with uniform mesh).

IV. A NUMERICAL TECHNIQUE TO DETERMINE SANDFACE CONDITIONS FROM WELL-BLOCK DATA IN GEOPRESSURED GEOTHERMAL RESERVOIR SIMULATION

4.1 INTRODUCTION

In numerical reservoir simulation, interest more often than not is centered upon the response of the reservoir as a whole to the production (and perhaps injection) of fluids. Thus, the reservoir is typically subdivided into a large number of computational zones (or "blocks"). Appropriate boundary conditions are imposed at the perimeter of this grid of zones, and the assumed initial state for each zone is specified. Then, the solution is carried out in a time-marching fashion, imposing prescribed mass sources or sinks in various zones to represent the effects of production or injection wells, respectively, which are located within the volume of space represented by the zone.

Normally, the size of a grid block containing a well will be much larger (i.e., tens or hundreds of meters) than the wellbore diameter itself (a small fraction of a meter). Therefore, conditions calculated by a numerical simulator for the well-block will in some sense represent average conditions in the general vicinity of the well, but will be different from the actual conditions prevailing at the sandface of the well. The disparity between the two will increase as the ratio of the well-block size to the wellbore size increases.

For many applications, of course, it is not necessary that sandface conditions be known at all. Sometimes, however, these conditions are of substantial interest. Particular applications include numerical simulation of pressure testing and production problems involving specification of well-head conditions. In the latter case, semi-empirical models of single- and multi-phase fluid and heat flow up the well have been developed over the years (see, e.g., Section II). These models require, however,

the sandface condition prevailing at the bottom of the hole. Stated somewhat differently, numerical reservoir simulators provide a way of obtaining well-block conditions from overall reservoir conditions; multi-phase wellbore models yield well-head conditions given bottomhole conditions. The "missing link" is a procedure for determining sandface conditions if the well-block conditions are known. This problem is the subject of this section.

4.2 THE SINGLE-PHASE CASE

Under very special circumstances, the problem can be approached analytically. Let us assume that the rock within the well-block is homogeneous and that the flow is essentially isothermal and single-phase. Since the time-scale for pressure response of the subgrid regime is much shorter than for the reservoir as a whole, the flow within the well-block may be regarded as steady. In horizontal, steady single-phase radial flow, conservation of fluid mass may be expressed by:

$$\frac{d}{dr}(r\phi\rho v) = 0 \tag{4.1}$$

Darcy's law for the single-phase case is simply:

$$v = -\frac{k}{\phi\mu}\frac{dP}{dr} \tag{4.2}$$

so that we may obtain integrating once:

$$\frac{2\pi rkH}{\nu}\frac{dP}{dr} = -Q \tag{4.3}$$

where

r = radius (measured from the well axis)

ϕ = rock porosity

ρ = fluid density

v = fluid radial velocity (positive outward)

k = rock permeability (constant)

μ = fluid dynamic viscosity

H = layer thickness (constant)

P = fluid pressure

Q = injection rate from well (mass per unit time); negative for a production well

ν = fluid kinematic viscosity = μ/ρ = const.

Equation (4.3) may readily be integrated again to yield:

$$P_w = P_0 + \frac{2\pi kH}{\nu Q} \ln (r_0/r_w) \qquad (4.4)$$

where P_w is the sandface pressure, P_0 is the well-block pressure, r_w is the borehole radius, and r_0 is the so-called "effective wellbore radius". Methods for estimating r_0 for particular problems are discussed elsewhere in this report (Section III and Appendix A); for the present, we note only that r_0 will be proportional to the linear dimensions of the well-block, so that as well-block size increases, the disparity between the computed well-block pressure and the true sandface pressure also increases.

In geopressured geothermal applications, Eq. (4.4) is probably adequate for treating reinjection wells. Fluids to be reinjected tend to be cool and devoid of methane, so that the reinjection stream will be single-phase. For production wells, however, Eq. (4.4) will often produce inaccurate results. In geopressured reservoirs, free methane may exist in the pores (or be produced in the pores by the production-induced pressure drop) so that the single-phase assumption implicit in Eq. (4.4) is inappropriate. In these cases, numerical integration of the governing equations from $r = r_w$ to $r = r_0$ may be employed to establish the relationship between well-block and sandface conditions.

4.3 FUNDAMENTAL TWO-PHASE GOVERNING EQUATIONS

The basic partial differential equations governing conservation of mass, species, momentum and energy in geothermal reservoirs are summarized in this section (see Garg, et al. [1977] for a detailed discussion of the governing equations). We consider a system with as many as two phases present in the pores of the reservoir rock (i.e., liquid water with dissolved methane, and free methane) with the mixture consisting of two species (water and methane). Momentum conservation is expressed by Darcy's law, written separately for each phase:

$$\underline{v}_\ell = \frac{kR_\ell}{\phi V_\ell \mu_\ell} (\rho_\ell \underline{g} - \nabla P) \tag{4.5}$$

$$\underline{v}_g = \frac{kR_g}{\phi V_g \mu_g} (\rho_g \underline{g} - \nabla P) \tag{4.6}$$

where

$\underline{v}_\ell, \underline{v}_g$ = velocity for liquid and gas phases, respectively

k = rock absolute permeability

ϕ = rock porosity

R_ℓ, R_g = relative permeability for liquid and gas phases

V_ℓ, V_g = liquid and gas pore volume fractions (note that $V_\ell + V_g = 1$)

μ_ℓ, μ_g = viscosities for each phase

ρ_ℓ, ρ_g = density for each phase

$\underline{g}$ = acceleration of gravity

P = fluid pressure.

Conservation of mass for the entire pore mixture (both phases, both species) may be expressed by

$$\frac{\partial}{\partial t}(\phi\rho) + \nabla \cdot (\phi\rho_\ell V_\ell \underline{v}_\ell + \phi\rho_g V_g \underline{v}_g) = 0 \qquad (4.7)$$

where

ρ = total density of pore contents (i.e., total pore mass/total pore volume)

$= \rho_\ell V_\ell + \rho_g V_g$.

For methane mass balance, we may write:

$$\frac{\partial}{\partial t}(\phi\rho C) + \nabla \cdot (\phi\rho_\ell V_\ell C_\ell \underline{v}_\ell + \phi\rho_g V_g \underline{v}_g) = 0 \qquad (4.8)$$

where

C = mass of methane in pore/total pore mass

C_ℓ = pore mass of methane in liquid phase/total pore liquid phase mass.

The energy balance may be expressed as follows:

$$\frac{\partial}{\partial t}[(1-\phi)\rho_R h_R + \phi(\rho_\ell h_\ell V_\ell + \rho_g h_g V_g)] - \frac{\partial}{\partial t}[\phi P] + \nabla \cdot (\phi\rho_\ell V_\ell h_\ell \underline{v}_\ell + \phi\rho_g V_g h_g \underline{v}_g) = \nabla \cdot (K\nabla T) + \phi(\rho_\ell V_\ell \underline{v}_\ell + \rho_g V_g \underline{v}_g) \cdot \underline{g} \qquad (4.9)$$

where

ρ_R = rock matrix density

h_R = rock matrix enthalpy

h_ℓ, h_g = enthalpy of liquid and gas phases, respectively

K = thermal conductivity of system

It will be convenient to express the enthalpies of the various phases by

$$h_x = E_x + \frac{P}{\rho_x} \qquad (4.10)$$

where x stands for ℓ or g, and where E_x denotes the internal energy per unit mass for phase x. It will also prove useful to define M_x and e_x as:

$$M_x = \frac{\rho_x V_x}{\rho} = \text{mass of phase x/pore mass} \tag{4.11}$$

$$e_x = \frac{M_x E_x}{E} = \text{energy in phase x/pore energy} \tag{4.12}$$

where E is the bulk internal energy per unit mass of the pore contents. Note that $\Sigma M_x = \Sigma e_x = 1$, where the sums are over both the phases.

4.4 GOVERNING EQUATIONS FOR STEADY TWO-PHASE RADIAL FLOW

For application to the problem at hand, the equations of the preceding section may be simplified substantially. We make the following observations:

1. The flow near the wellbore may be regarded as steady, so that

$$\frac{\partial}{\partial t}(X) \to 0.$$

2. Since flow velocities are high near operating wells, heat conduction may be ignored in comparison with convection.

3. The flow may be regarded as horizontal, so that gravity terms may be dropped.

4. The flow is radial, so that the divergence operator is:

$$\nabla \cdot (\vec{X}) \to \frac{1}{r}\frac{d}{dr}(rX).$$

With these simplifications, Eqs. (4.7), (4.8) and (4.9) may be written in the following way:

Total Mass:

$$\frac{d}{dr}\left(r\ k\ \rho\ \frac{dP}{dr}\ \Sigma_1\right) = 0 \tag{4.13}$$

Methane Mass:

$$\frac{d}{dr}\left(r\ k\ \rho\ \frac{dP}{dr}\ \Sigma_2\right) = 0 \tag{4.14}$$

Energy:

$$\frac{d}{dr}\left(r\ k\ \rho\ E\ \frac{dP}{dr}\ \Sigma_3 + r\ k\ P\ \frac{dP}{dr}\ \Sigma_4\right) = 0 \tag{4.15}$$

where

$$\Sigma_1 \equiv \frac{R_\ell\ M_\ell}{V_\ell\ \mu_\ell} + \frac{R_g\ M_g}{V_g\ \mu_g} \tag{4.16}$$

$$\Sigma_2 \equiv \frac{R_\ell\ M_\ell\ C_\ell}{V_\ell\ \mu_\ell} + \frac{R_g\ M_g}{V_g\ \mu_g} \tag{4.17}$$

$$\Sigma_3 \equiv \frac{R_\ell\ e_\ell}{V_\ell\ \mu_\ell} + \frac{R_g\ e_g}{V_g\ \mu_g} \tag{4.18}$$

$$\Sigma_4 \equiv \frac{R_\ell}{\mu_\ell} + \frac{R_g}{\mu_g} \tag{4.19}$$

Equations (4.13) through (4.15) can be integrated to yield:

$$\left(r\ k\ \frac{dP}{dr}\right)\ \rho\ \Sigma_1 = -\ \frac{Q}{2\pi H} \tag{4.20}$$

$$\left(r\ k\ \frac{dP}{dr}\right)\ \rho\ \Sigma_2 = -\ \frac{Q_m}{2\pi H} \tag{4.21}$$

$$\left(r\ k\ \frac{dP}{dr}\right)\ \left(\rho E\ \Sigma_3 + P\ \Sigma_4\right) = -\ \frac{\dot{e}}{2\pi H} \tag{4.22}$$

Here, as before, H represents the aquifer (or layer) thickness, and (-Q) is the mass production rate from the well. The quantity ($-Q_m$) is the production rate of methane, and ($-\dot{e}$) is the enthalpy production rate. All of these quantities are constants. Now, dividing Eqs. (4.21) and (4.22) by Eq. (4.20), we obtain the set:

$$2\pi r\, k\, H\, \rho\, \Sigma_1 \frac{dP}{dr} = -\, Q = \text{const.} \tag{4.23}$$

$$\frac{\Sigma_2}{\Sigma_1} = \frac{Q_m}{Q} = F_m = \text{const.} \tag{4.24}$$

$$E\, \frac{\Sigma_3}{\Sigma_1} + \frac{P}{\rho}\, \frac{\Sigma_4}{\Sigma_1} = \frac{\dot{e}}{Q} = \varepsilon = \text{const.} \tag{4.25}$$

Note that F_m is just the mass fraction of methane in the total mass flow (-Q) entering the well, and ε is the bulk enthalpy of that fluid.

The essential problem, then, is to solve the system of Eqs. (4.23)-(4.25) over the interval

$$r_w \leq r \leq r_0$$

where r_0 is the effective well-block radius and r_w is the well radius with $Q < 0$ (i.e., a production well), and with the essential constitutive data (that is, P, E and C) known at $r = r_0$. To close the system of equations, we assume that constitutive data, that is (e_x, V_x, M_x, μ_x, C_ℓ and ρ for $x = \ell$ and g) are known functions of, say, P, E and C (see Garg, et al. [1977] for a description of the equation of state for water-methane mixtures). We further assume that the relative permeabilities for each phase (R_ℓ, R_g) are defined in terms of other constitutive parameters, i.e.,

$$R_x = \text{fns of } (V_\ell,\ V_g,\ M_\ell,\ M_g,\ P,\ T,\ \text{etc.}).$$

4.5 NUMERICAL SOLUTION TECHNIQUE

Given constitutive relations for water-methane mixtures, the essential governing equations of the preceding section must be solved numerically. A computer program has been written to solve these equations given arbitrary boundary conditions. The numerical procedure is as follows. We divide the region of interest from r_w to r_0 into M-1 zones, separated by M nodes located at the r_i, where:

$$r_i = r_w \left(\frac{r_0}{r_w}\right)^{\left(\frac{i-1}{M-1}\right)} \tag{4.26}$$

Each node has associated with it a particular value of permeability k_i. The boundary conditions are specified at $r = r_0$, that is, at $i = M$. Using the constitutive package, we may then evaluate the constants in Eqs. (4.24) and (4.25) setting $P_M = P_0$, $E_M = E_0$, $C_M = C_0$ where P_0, E_0 and C_0 represent well-block conditions at r_0:

$$F_m = \Sigma_{2_M}/\Sigma_{1_M} \tag{4.27}$$

$$\varepsilon = E_M \left(\frac{\Sigma_3}{\Sigma_1}\right)_M + \frac{P_M}{\rho_M}\left(\frac{\Sigma_4}{\Sigma_1}\right)_M \tag{4.28}$$

Note that this boundary data is all that is required to establish the enthalpy and composition of the material entering the well.

Next, we fill in the data for the remainder of the grid ($1 \leq i \leq M-1$) in a stepwise fashion. If the state at node $i + 1$ (that is, at $r = r_{i+1}$) is known, the state at node i ($r = r_i$) may be determined as follows:

Step 1: Predict the pressure at node i by:

$$P_i = P_{i+1} + \frac{Q\,(k_i + k_{i+1})\,\ell n\,(r_{i+1}/r_i)}{4\pi\, k_i\, k_{i+1}\, H\, \rho_{i+1}\, \Sigma 1_{i+1}} \tag{4.29}$$

Step 2: Obtain the remainder of the constitutive description at $r = r_i$ by simultaneously satisfying the following to determine E_i and C_i:

$$\frac{\Sigma 2_i}{F_m\, \Sigma 1_i} - 1 = 0 \tag{4.30}$$

$$\frac{E_i\, \Sigma 3_i + \frac{P_i}{\rho_i}\, \Sigma 4_i}{\varepsilon\, \Sigma 1_i} - 1 = 0 \tag{4.31}$$

Step 2 involves an iteration upon E_i and C_i to simultaneously satisfy Eqs. (4.30) and (4.31). Once the entire grid has been filled in (that is, P_i, E_i and C_i have been determined for $1 \leq i \leq M$), conditions at the sandface of the well are those at $i = 1$.

V. PRELIMINARY ASSESSMENT OF LONG-TERM PRODUCTION AND SUBSIDENCE BEHAVIOR OF THE BRAZORIA COUNTY PROSPECT

5.1 INTRODUCTION

For the last several years, the University of Texas at Austin (under sponsorship of the U. S. Department of Energy) has been conducting a study to evaluate the potential of producing geothermal energy from the geopressured Tertiary sandstones along the Texas Gulf Coast. According to Bebout, et al. [1977], the objective of this work is to locate several prospective reservoirs with the following specifications:

Reservoir volume > 3 cubic miles
Permeability > 20 md
Fluid temperature > 300°F
Initial bottom hole pressure > 10,000 psi
Production rate (per well) ∿ (20,000-40,000) bbl/day.

The produced water is expected to have a salinity of 20,000 - 80,000 ppm total dissolved solids and to be saturated with methane (40-50 cu ft/bbl of water). Preliminary indications are that three formations - the Frio, Vicksburg and Wilcox - have potential to meet these specifications [Bebout, et al., 1977]. So far, only the Frio formation has been investigated in detail. Five "geothermal fairways" (areas with thick sandstone bodies with estimated temperatures in excess of 300°F) - Hidalgo, Armstrong, Corpus Christi, Matagorda, and Brazoria - have been identified in the Frio formation (Figure 5.1). It, however, appears that only the Brazoria fairway meets all the specifications for a geothermal prospect; the Austin Bayou Prospect (Figure 5.2), lying between the Danbury Dome area and chocolate Bayou, has been developed within this fairway. A test well (General Crude Oil Company and DOE 1 Martin Ranch) is scheduled to be drilled in this area later this year.

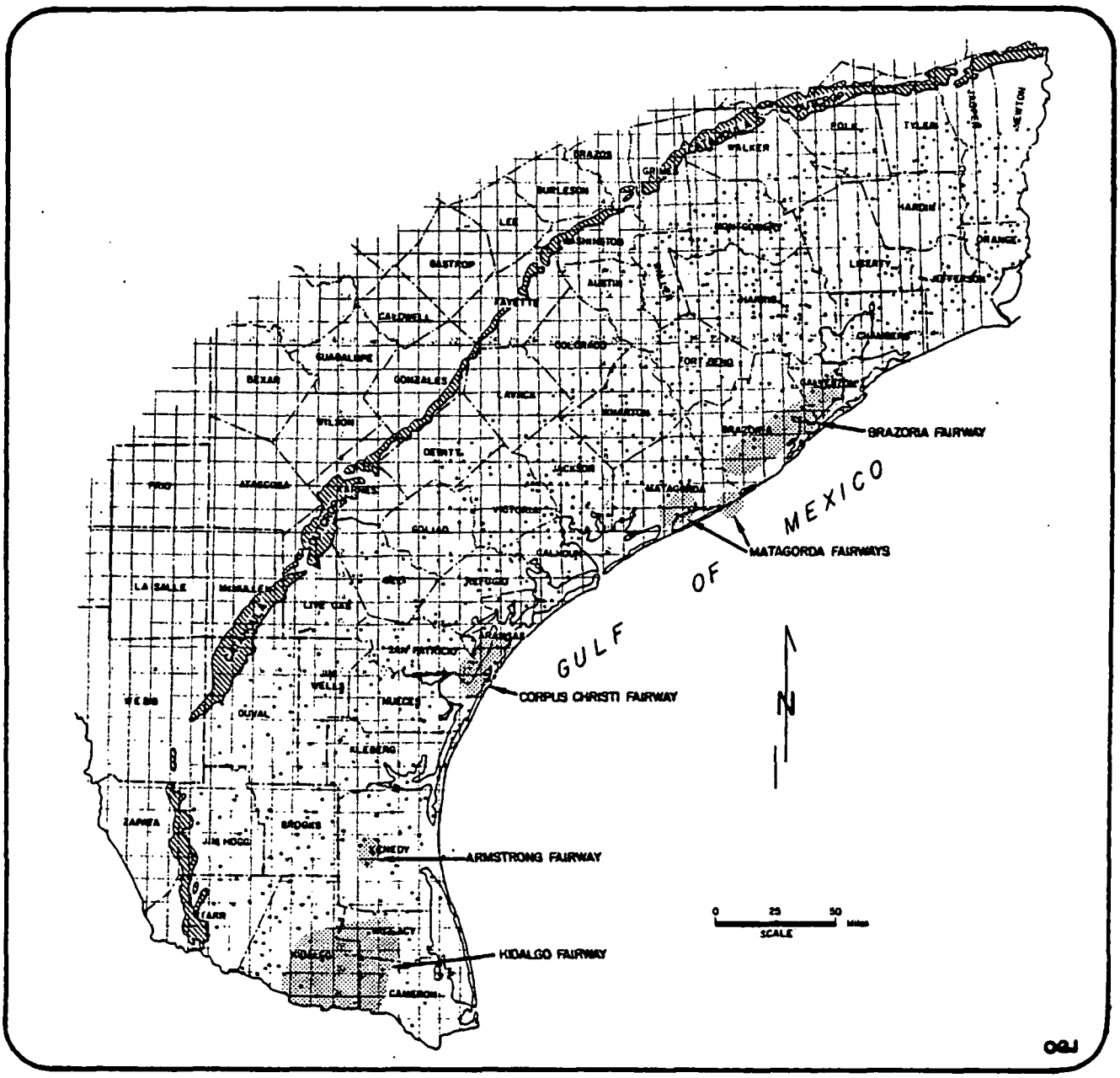

Figure 5.1. Geothermal fairways, Texas Gulf Coast (Frio formation). Reproduced from Bebout, et al. [1977].

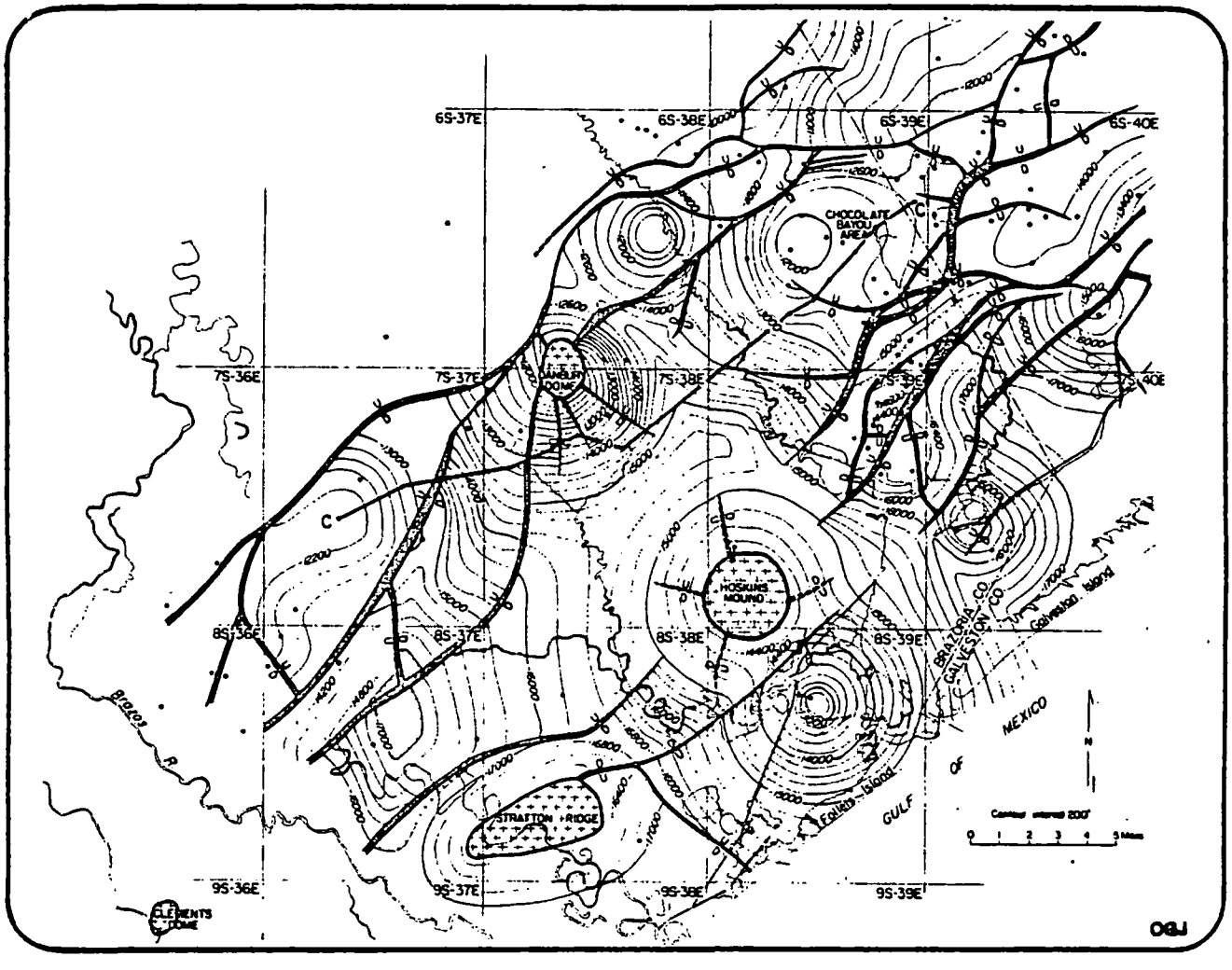

Figure 5.2. Structure at Brazoria Fairway - top of Anomalina bilateralis zone. Reproduced from Bebout, et al. [1977].

Geothermal gradients along the Gulf Coast are in the range 1.4 to 2.4°F/100 feet; in Brazoria County, the geothermal gradient is approximately 1.8°F/100 feet as indicated by temperature measurements in wells at depths ranging from 8,500 feet to 18,000 feet [Bebout, et al., 1977]. The 200°F and 300°F isotherms occur at depths of 8,200 feet and 13,500 feet, respectively. The top of the geopressure is at approximately 10,000 feet below sea level, and the geopressure gradients lie between 0.465 and 0.98 psia per foot.

The Brazoria fairway is approximately 20 miles long and 10 miles wide; the prospective geothermal sandstone reservoirs lie within the Anomalina bilateralis zone (Figure 5.2). Reservoir thickness varies from more than 1,200 feet in the Danbury Dome area to less than 200 feet at Chocolate Bayou. The Austin Bayou (site of test well), Figure 5.3, has been selected on the basis of the most promising combination of sand thickness, permeability and temperature. In the Chocolate Bayou field, the net sandstone thickness is low, individual sandstone bodies are thick, temperatures are low and permeability is high. On the other hand, near the Danbury dome, the cumulative sandstone thickness is high, individual sandstone bodies are thin, fluid temperatures are high and permeability is low. It is estimated that the Austin Bayou area (located between the Danbury dome and the Chocolate Bayou) has a total sandstone thickness of 800-900 feet, average permeability (from unconfined cores) of 40-60 md, and fluid temperature in the range of 300°F (at 14,000 feet depth) to 350°F (at 16,500 feet). Salinities may lie anywhere in the range 40,000 ppm to 100,000 ppm.

Bebout, et al. [1977] estimate that the proposed test well in the Austin Bayou prospect will drain several sandstone reservoirs (see zones labeled as A, B, C, D, E and F in Figure 5.4) in an area of approximately 16 square miles. The net sandstone thickness, inferred from an interpolated

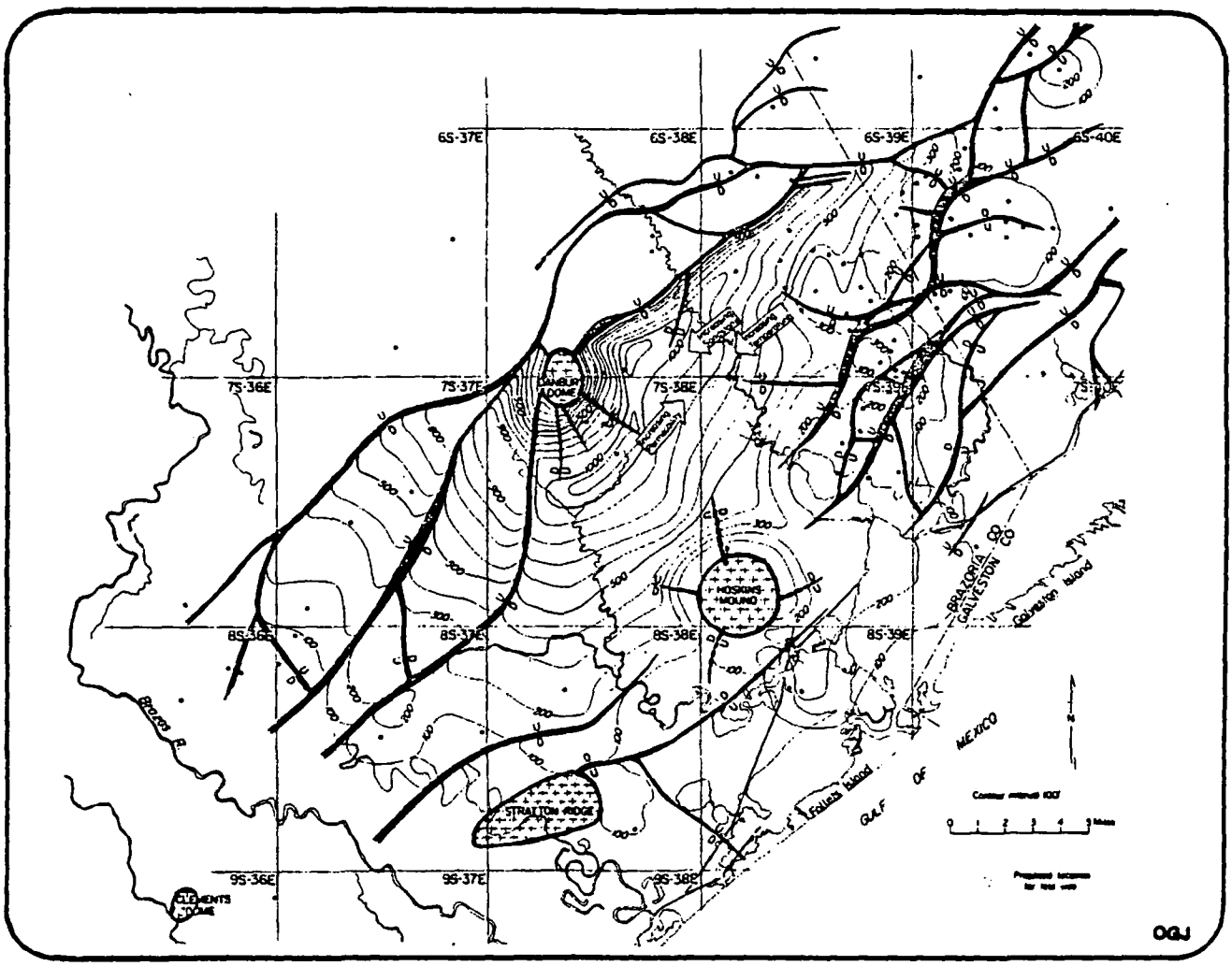

Figure 5.3. Net sandstone map zones showing location of Austin Bayou prospect (→ ←). Reproduced from Bebout, et al. [1977].

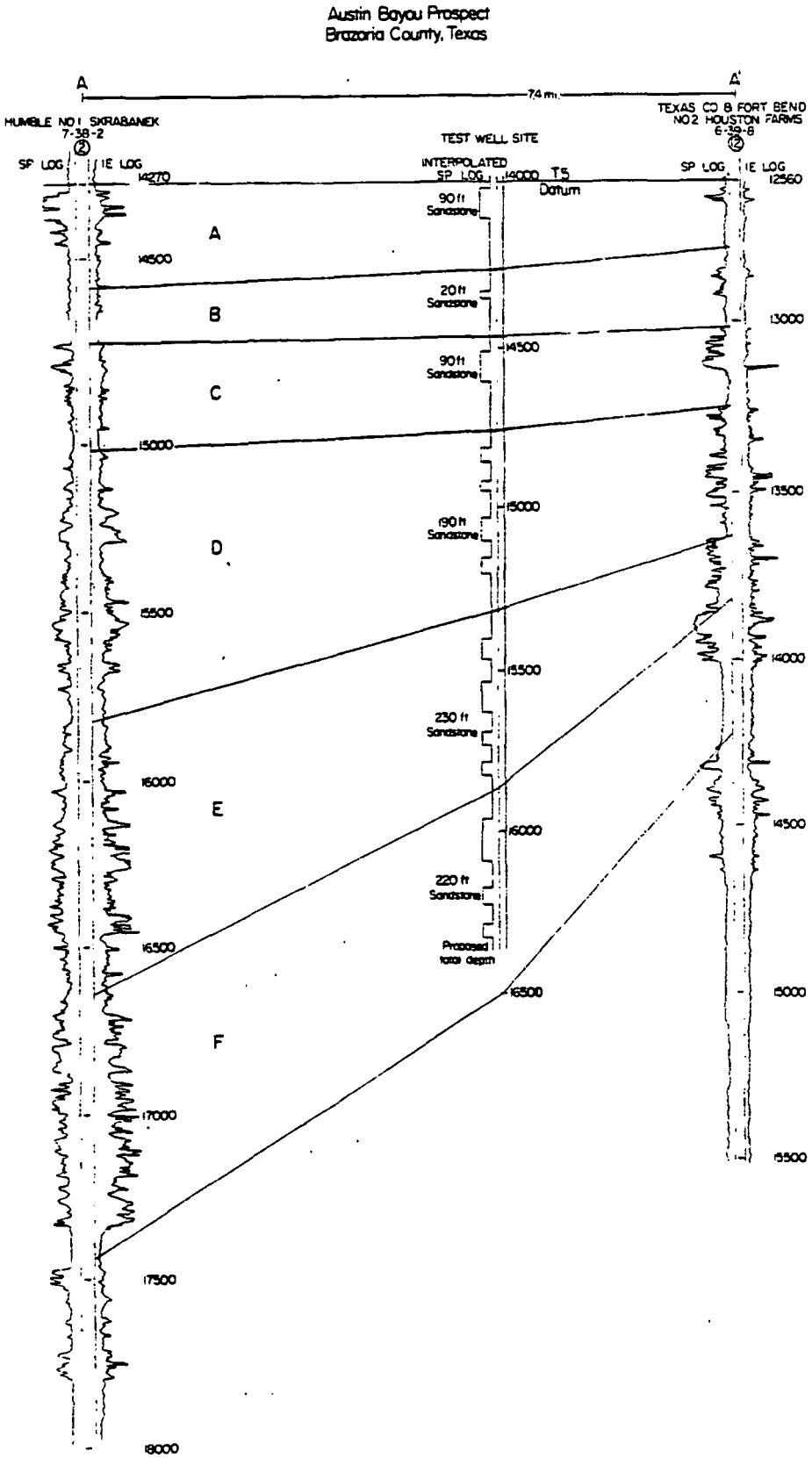

Figure 5.4. Expected sandstone distribution for the test-well site from a synthetic SP log created by interpolation from existing control wells. Reproduced from Bebout, et al. [1977].

spontaneous potential log, is 840 feet. Average porosity of at least 20 percent is predicted for 250 feet of the sandstone; the remaining sandstone has a porosity between 5-20 percent with an average value of 15 percent. The total pore volume, water in pores, and gas in place are estimated to be 60 billion cubic feet, 10 billion bbl, and 426 billion cubic feet, respectively.

It need be hardly emphasized that the estimated values for reservoir properties must be confirmed by well tests. Nevertheless, pending the availability of actual well test data, it is useful to employ the estimated reservoir properties in numerical simulations to assess the long term production and subsidence behavior of the Austin-Bayou prospect. Such numerical simulations should be valuable in (1) planning well tests and (2) assessing the sensitivity of reservoir behavior to variations in fundamental reservoir properties (fault size, porosity, permeability, sand thickness, shale distribution, etc.) and production/injection strategies.

The reservoir simulation group at UTA (University of Texas at Austin) has run a series of areal calculations to study the effects of variations in drainage area, sandstone compressibility and pore fluid salinity. In parallel with this work, a series of four axisymmetric calculations was made at Systems, Science and Software (S^3) to investigate the role of shale distribution, compressibility and vertical permeability. The S^3 work is discussed in Section 5.2. The UTA and S^3 parametric runs taken together provide a basis for the initial design of well tests (to be undertaken early in the third year of this work).

Gustavson and Kreitler [1976] have discussed the environmental concerns arising from the production of geopressured geothermal reservoirs; according to these authors subsidence is a major concern along the Texas Gulf Coast. In

Section 5.3, we give very preliminary estimates of subsidence associated with the production of waters from the Austin-Bayou prospect. It should be emphasized that these predictions are based upon hypothetical overburden/underburden properties, and as such may not have any quantitative significance. Like the reservoir assessment calculations, more accurate prediction of subsidence will have to await the availability of well-test and core-analysis data.

5.2 SHALE DISTRIBUTION, PERMEABILITY AND COMPRESSIBILITY, AND RESERVOIR PERFORMANCE

It is likely that, at least initially, the test well will be used to produce fluids from one or more sand bodies located within a single zone (Figure 5.4). Flow testing of individual sand bodies is required to obtain accurate estimates for formation parameters. In the following, we will, therefore, confine our attention to zone E (Figure 5.4). The top and the bottom of zone E are at depths of 15,300 feet and 15,800 feet, respectively. We also note that zone E has the thickest sandstone bodies (from 50 to 100 feet).

A series of four axisymmetric calculations was run with the MUSHRM reservoir simulator to study the sensitivity of the reservoir behavior to (1) variations in sandstone/shale distribution, (2) shale compressibility, and (3) vertical shale permeability. For this series of parametric calculations, it is convenient to consider a standard base case (Case 1) and to vary the parameters of interest around the values assumed in the base case.

In all the cases reported hereunder, the reservoir is assumed to be a right circular cylinder with radius $R = 3.63 \times 10^5$ cm (corresponding to a block area of 16 square miles) and height $h = 1.524 \times 10^4$ cm (500 feet). The net sand thickness (= net shale thickness) is 0.762×10^4 cm (250 feet). The numerical grid, along with the shale/sand arrangement, used in

the base case is shown in Figure 5.5. Rock properties for the base case are given in Table 5.1. The reservoir fluid is assumed to be pure liquid water (zero salinity) saturated with methane. The initial pore pressure, temperature, and methane mass fraction at a depth of 15,500 feet are P = 793 bars (∿ 11,500 psi), T = 162.7°C (∿ 325°F) and C = 0.007015, respectively. Initially, the reservoir fluids are assumed to be in hydrostatic equilibrium; the initial conditions assigned by the simulator are listed in Table 5.2. The reservoir is produced at a constant mass rate $3.679\ 10^4$ gm/sec (∿ 20,000 STB/day); it is assumed that all of the production is from the sandstone layers (j = 2, 4, 6, 7, 9). In the numerical simulation, the effect of mass withdrawal is represented by a constant volumetric sink term in the sandstone zones closest to the centerline (see Figure 5.5). The volumetric sink term (i.e., mass produced/unit volume of well-block) is given by

$$\dot{m} = \frac{3.679\ 10^4}{5 \times 1524 \times \pi\ 10^8}\ \text{gm/cm}^3\text{sec}$$

$$= 1.536827\ 10^{-8}\ \text{gm/cm}^3\text{sec}.$$

Table 5.3 gives the pressure drop in the various well-blocks as a function of drawdown time. The pressure drops in well-blocks (i = 1, j = 2,4,9) are practically the same but differ substantially from those in blocks (i = 1, j = 6,7). This clearly illustrates the influence of fluid influx from the adjoining shales. Layers j = 2,4,9 are 1524 cm (50 feet) thick sandstone bodies sandwiched between shales whereas layers j = 6,7 are contiguous sandstone bodies (total thickness ∿ 3048 cm). As far as well testing is concerned, we note that influx from shales should have little or no effect for practical drawdown/buildup times (Table 5.3 shows that the pressure drops in the various well-blocks are essentially the same for times less than 1-2 years).

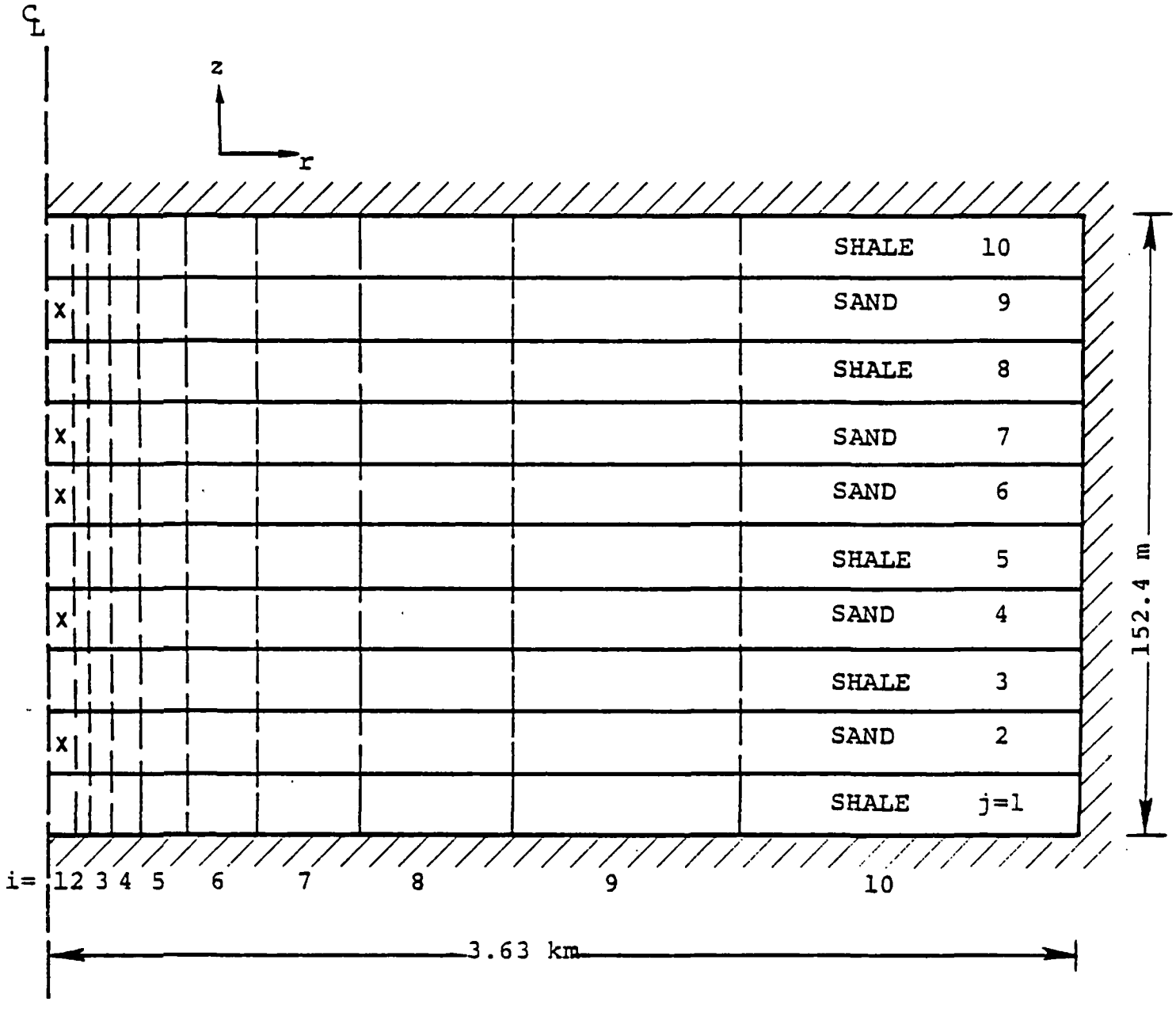

Figure 5.5. Numerical grid and the shale/sandstone arrangement utilized in Cases 1, 3 and 4. The reservoir is approximated by a 10×10 grid ($\Delta z_1 = \Delta z_2 = \ldots = \Delta z_{10} = 1524$ cm; $\Delta r_1 = 10^4$ cm; $\Delta r_2 = 4.9\times10^3$ cm; $\Delta r_3 = 7.3\times10^3$ cm; $\Delta r_4 = 10.9\times10^3$ cm; $\Delta r_5 = 16.3\times10^3$ cm; $\Delta r_6 = 24.2\times10^3$ cm; $\Delta r_7 = 36.0\times10^3$ cm; $\Delta r_8 = 53.8\times10^3$ cm; $\Delta r_9 = 80.1\times10^3$ cm; $\Delta r_{10} = 119.5\times10^3$ cm). The well-blocks are indicated by x.

TABLE 5.1

ROCK PROPERTIES FOR THE BASE CASE

	Sand	Shale
Porosity	0.2	0.2
Density (Grain)	2.633 gm/cm^3 (164.4 lbm/cu ft)	2.633 gm/cm^3 (164.4 lbm/cu ft)
Specific Heat	0.963 10^7 ergs/gm°C (0.23 Btu/lb°F)	0.963 10^7 ergs/gm°C (0.23 Btu/lb°F)
Rock Grain Thermal Conductivity	5.25 ergs/cm sec°C (3.033 Btu/hr ft°F)	5.25 ergs/cm sec°C (3.003 Btu/hr ft°F)
Vertical Permeability	2 10^{-11} cm^2 (2 md)	10^{-16} cm^2 (10^{-5} md)
Horizontal Permeability	20 10^{-11} cm^2 (20 md)	10^{-15} cm^2 (10^{-4} md)
Compressibility	0.725 10^{-10} cm^2/dynes (5×10^{-6} psi^{-1})	14.5 10^{-10} cm^2/dynes (10^{-4} psi^{-1})

Relative permeabilities given by Corey equations

Residual liquid saturation = 0.30

Residual gas saturation = 0.00

TABLE 5.2

INITIAL CONDITIONS ASSIGNED BY THE SIMULATOR
(CASES 1, 3 AND 4)

j	Rock Type	Pressure (bars)	Methane Mass Fraction
1	Shale	799.26(11,592 psi)	0.00705
2	Sandstone	797.86(11,571 psi)	0.00704
3	Shale	796.46(11,551 psi)	0.00704
4	Sandstone	795.07(11,531 psi)	0.00703
5	Shale	793.67(11,511 psi)	0.00702
6	Sandstone	792.28(11,490 psi)	0.00701
7	Sandstone	790.88(11,470 psi)	0.00700
8	Shale	789.49(11,450 psi)	0.00700
9	Sandstone	788.09(11,430 psi)	0.00699
10	Shale	786.70(11,410 psi)	0.00698

TABLE 5.3

PRESSURE DROP (BARS) IN WELL-BLOCKS (i = 1, j) FOR THE BASE CASE

Time (Years)	2	4	6	7	9
0.0028	7.87	7.86	7.87	7.86	7.58
0.090	21.25	21.31	21.27	21.26	21.27
0.901	31.04	31.02	31.12	31.11	31.00
1.802	36.16	36.16	36.36	36.36	36.11
2.703	40.79	40.77	41.30	41.25	40.74
3.605	45.44	45.17	46.23	46.22	45.23
4.506	49.62	49.61	50.83	50.84	49.57
5.407	53.54	53.78	55.54	55.53	53.83
6.309	57.79	57.79	60.10	59.96	57.74
7.210	61.62	61.60	64.59	64.58	61.51
8.111	65.36	65.38	68.76	68.97	65.31
9.012	68.94	69.00	73.21	73.20	68.81
9.914	72.38	72.42	77.37	77.38	72.33
10.815	75.65	75.71	81.52	81.51	75.71
11.716	78.90	78.96	85.54	85.57	78.84
12.617	82.04	82.05	89.50	89.49	81.88
13.519	84.95	85.03	93.57	93.29	84.89
14.420	87.68	87.86	97.30	97.29	87.84
15.321	90.57	90.68	101.00	101.03	90.52
16.222	93.11	93.34	104.66	104.65	93.18
17.124	95.79	95.94	108.30	108.36	95.74
18.025	98.28	98.48	111.86	111.85	98.14
18.926	100.65	100.83	115.32	115.42	100.61
19.827	102.92	103.17	118.82	118.81	102.82
20.729	105.18	105.40	122.17	122.15	105.14
21.630	107.35	107.56	125.47	125.46	107.37
22.531	109.39	109.67	128.70	128.72	109.36
23.432	111.37	111.64	131.88	131.87	111.42
24.424	113.48	113.98	135.31	135.30	113.49
25.325	115.42	115.70	138.40	138.39	115.43
26.226	117.17	117.56	141.42	141.41	117.13
27.128	118.95	119.35	144.41	144.40	118.94
28.029	120.60	121.08	147.35	147.34	120.61
28.930	122.25	122.80	150.18	150.17	122.25
30.282	124.57	125.12	154.40	154.38	124.59

(Maximum gas saturation at 30.282 years $\sim$ 1.4 percent)

The MUSHRM simulator updates porosity along with fluid state. Given current and initial porosities (ϕ and ϕ_0), the formation compaction can be calculated from the formula:

$$\Delta h_i = \sum_{j=1}^{10} h_j \frac{\phi_{ji}}{1-\phi_{0j}}$$

where

Δh_i = change in thickness of column i

h_j = thickness of layer j

ϕ_{ji} = current porosity in grid-block (i,j)

ϕ_{0j} = initial porosity of layer j.

The computed formation compaction at t = 30.282 years for the base case is given in Table 5.4. As might be expected, the formation compaction is maximum near r = 0 and drops off with increasing radius.

The results for the base case discussed above illustrate the importance of shale/sand arrangement. To further investigate the effects of shale distribution, in Case 2 the shale/sand arrangement was changed to the one shown in Figure 5.6. Note that in Case 2, like the base case, the net sandstone thickness is 0.762×10^4 cm (250 feet). The numerical grid in the r-direction is the same as that of Case 1; in the z-direction we employ four layers ($\Delta z_1 = \Delta z_2 = \Delta z_8 = \Delta z_9 = 1905$ cm) to represent the shale and five layers ($\Delta z_3 = \Delta z_4 = \ldots = \Delta z_7 = 1524$ cm) for the sandstones. The initial conditions assumed by the simulator for this case are shown in Table 5.5. The mass production is from the sandstone grid blocks closest to the centerline (i.e., i = 1, j = 3,4,...,7). The rest of the input parameters for Case 2 are identical with those of Case 1. The pressure drops in the well-blocks are given in Table 5.6; within numerical precision, the pressure drops are the same

TABLE 5.4

RESERVOIR COMPACTION AT t = 30.282 YEARS FOR THE BASE CASE

Column (i)	Δh (cm)
1	133.8
2	126.9
3	123.1
4	119.3
5	115.6
6	111.9
7	108.3
8	104.9
9	101.9
10	99.8

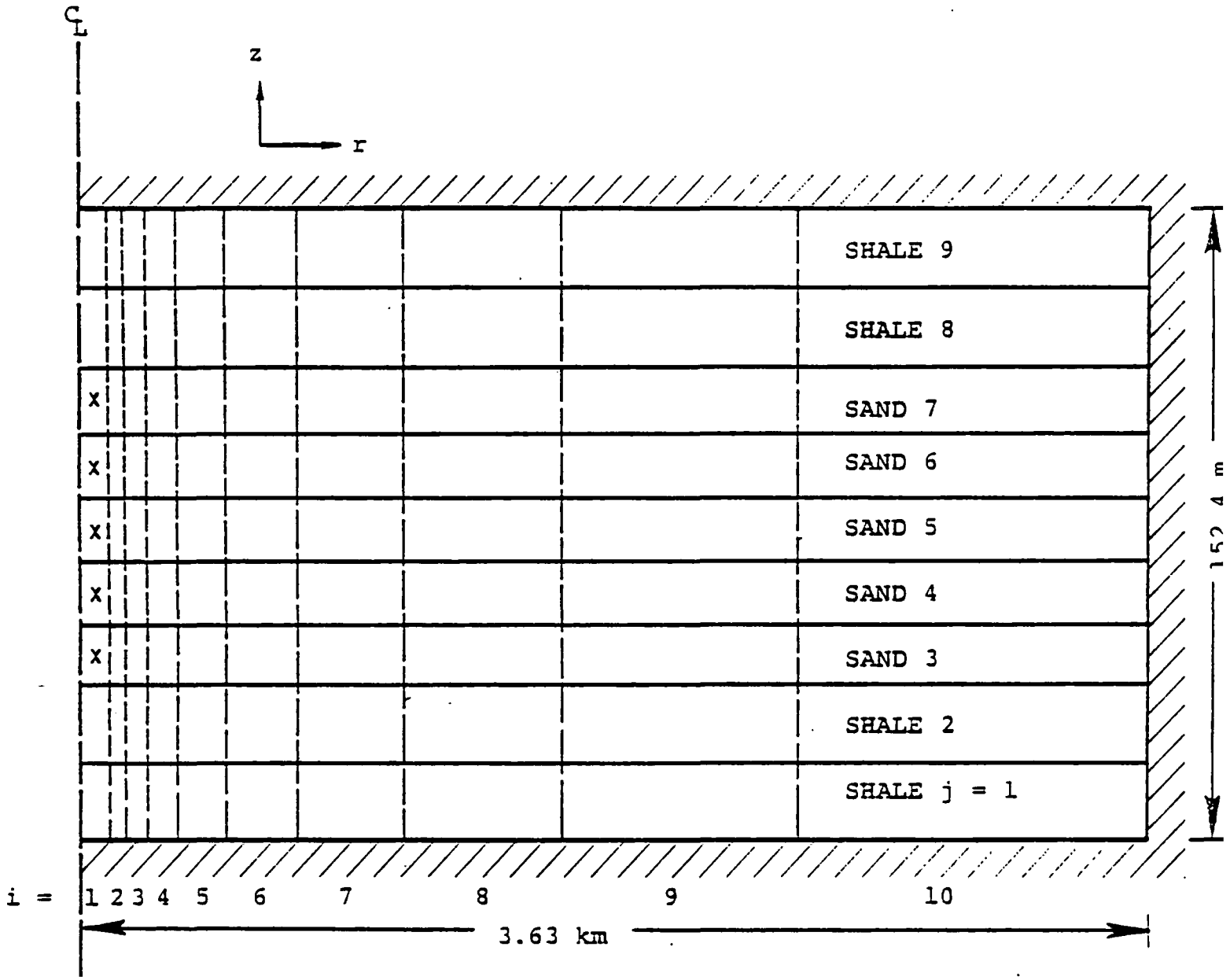

Figure 5.6. Numerical grid and the shale/sandstone arrangement utilized in Case 2. The reservoir is approximated by a 9×10 grid ($\Delta z_1 = \Delta z_2 = \Delta z_8 = \Delta z_9 = 1905$ cm; $\Delta z_3 = \Delta z_4 = \ldots = \Delta z_7 = 1524$ cm; $\Delta r_1 = 10^4$ cm; $\Delta r_2 = 4.9\times10^3$ cm; $\Delta r_3 = 7.3\times10^3$ cm; $\Delta r_4 = 10.9\times10^3$ cm; $\Delta r_5 = 16.3\times10^3$ cm; $\Delta r_6 = 24.2\times10^3$ cm; $\Delta r_7 = 36.0\times10^3$ cm; $\Delta r_8 = 53.8\times10^3$ cm; $\Delta r_9 = 80.1\times10^3$ cm; $\Delta r_{10} = 119.5\times10^3$ cm). The well-blocks are indicated by x.

TABLE 5.5

INITIAL CONDITIONS ASSUMED BY THE SIMULATOR FOR CASE 2

j	Rock Type	Pressure (bars)	Methane Mass Fraction
1	Shale	799.07(11,589 psi)	0.007049
2	Shale	797.34(11,564 psi)	0.007040
3	Sandstone	795.77(11,541 psi)	0.007035
4	Sandstone	794.37(11,521 psi)	0.007025
5	Sandstone	792.98(11,501 psi)	0.007015
6	Sandstone	791.58(11,480 psi)	0.007005
7	Sandstone	790.19(11,460 psi)	0.007000
8	Shale	788.62(11,437 psi)	0.006994
9	Shale	786.87(11,412 psi)	0.006981

TABLE 5.6

PRESSURE DROP (BARS) IN WELL-BLOCKS (i = 1, j) FOR CASE 2

Time (Years)	3	4	5	6	7
0.003125	8.24	8.24	8.24	8.24	8.24
0.1	21.67	21.67	21.67	21.66	21.67
0.6	29.15	29.18	29.19	29.14	29.16
1.1	32.47	32.47	32.47	32.47	32.47
2.1	38.20	38.20	38.20	38.20	38.20
3.1	43.89	43.88	43.89	43.88	43.88
4.1	49.51	49.50	49.50	49.50	49.50
5.1	55.07	55.06	55.06	55.06	55.06
6.1	60.59	60.58	60.58	60.58	60.57
7.1	66.06	66.05	66.05	66.05	66.05
8.1	71.46	71.45	71.45	71.44	71.44
9.1	76.85	76.84	76.84	76.83	76.83
10.1	82.20	82.19	82.19	82.18	82.18
11.1	87.52	87.50	87.50	87.49	87.49
12.1	92.81	92.79	92.79	92.78	92.78
13.1	98.07	98.06	98.06	98.05	98.05
14.1	103.21	103.19	103.19	103.18	103.18
15.1	108.36	108.34	108.34	108.33	108.33
16.1	113.45	113.44	113.44	113.44	113.44
17.1	118.55	118.54	118.54	118.53	118.53
18.1	123.60	123.58	123.58	123.57	123.57
19.1	128.59	128.58	128.58	128.57	128.56
20.1	133.57	133.56	133.56	133.55	133.54
21.1	138.47	138.46	138.46	138.45	138.44
22.1	143.38	143.37	143.37	143.36	143.36
23.1	148.23	148.22	148.22	148.21	148.20
24.1	153.06	153.05	153.05	153.04	153.03
25.1	157.84	157.83	157.83	157.82	157.81
26.1	162.56	162.54	162.54	162.53	162.53
27.1	167.28	167.27	167.26	167.25	167.25
28.1	171.96	171.95	171.94	171.92	171.92
29.1	176.58	176.57	176.56	176.55	176.55
30.1	181.21	181.20	181.19	181.18	181.18

(Maximum vapor saturation at 30.1 years ≈ 0.015)

for all of the well-blocks. Figures 5.7 and 5.8 compare the pressure drops obtained in Case 1 with those for the present case. Not surprisingly, for times less than one to two years, there is little difference between the pressure drops for the two cases; this once again emphasizes the fact that the influx from shale is likely to be important only for long production times. For $t > \sim 3$ years, the present case yields higher pressure drops; this is again consistent with the results for Case 1 insofar as the importance of influx from shale decreases with increasing sandstone thickness. The formation compaction at $t \sim 30.1$ years is given in Table 5.7. A comparison of Tables 5.4 and 5.7 shows that the formation compaction is somewhat lower in the present case; this result is mainly due to a smaller pressure drop in the shales (which are more compressible than the sandstones).

Case 3 was designed to assess the effects of vertical shale permeability; in this case the vertical shale permeability is taken to be 10^{-15} cm^2 ($\sim 10^{-4}$ md) - a factor of 10 greater than the value assumed in the base case. All other input parameters (rock properties, grid, mass production rate, etc.) remain unchanged from the base case. The pressure drops in the well-blocks and the formation compaction are given in Tables 5.8 and 5.9, respectively. The major effect of an increase in vertical shale permeability is to enhance influx from shales and to reduce pressure drop in well-blocks (see Figures 5.7 and 5.8). Figures 5.7 and 5.8 also show that for periods less than one year, the shale influx is liable to be minimal. Increased influx from shales results in a larger pressure drop in the shales (and hence larger formation compaction - Table 5.9).

The input parameters for Case 4 are identical with those utilized in the base case except the shale compressbility was changed to 1.45 10^{-10} cm^2/dynes ($\sim 10^{-5}$ psi) - i.e., one-tenth of its value in the base case. The well-block

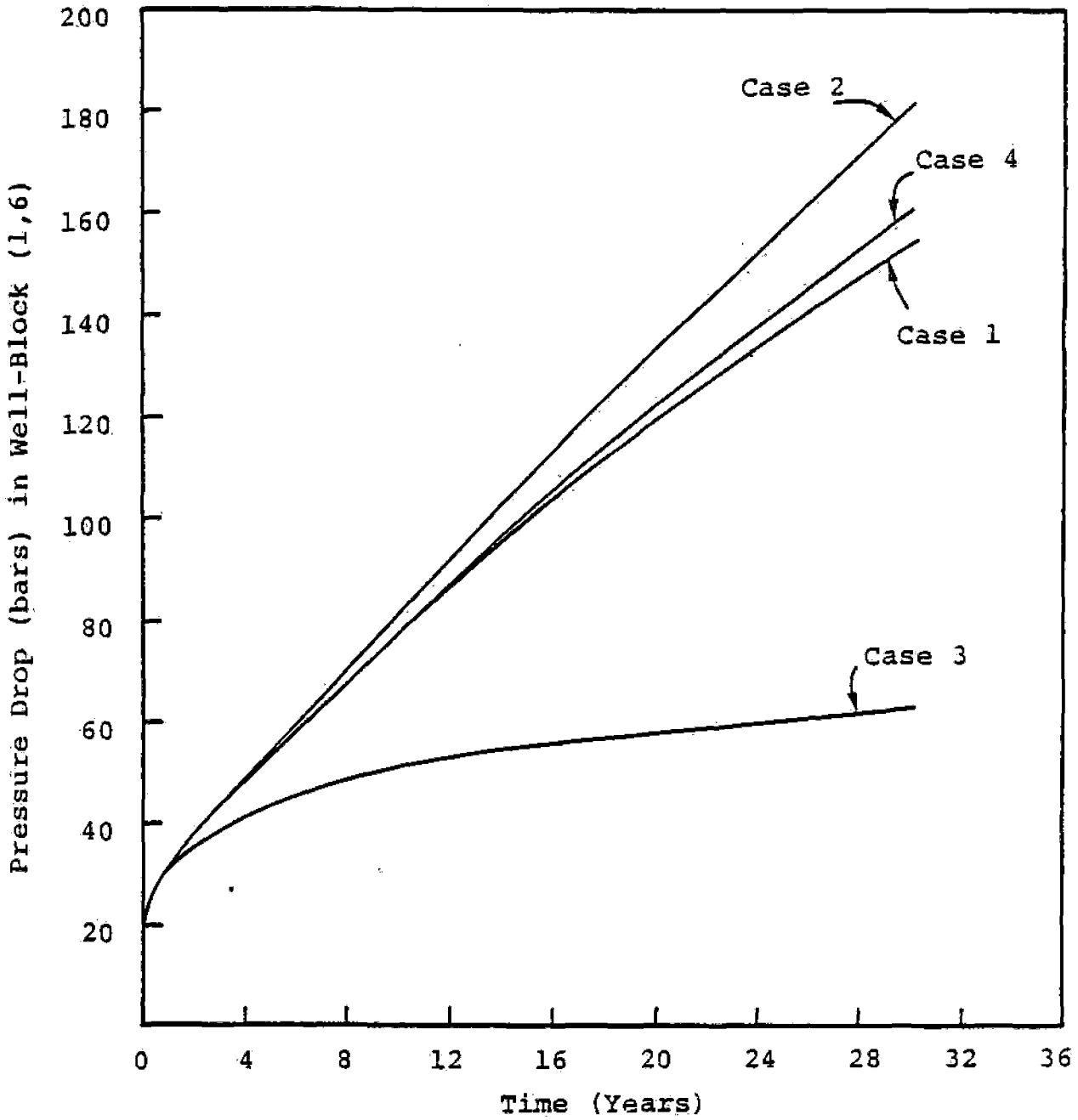

Figure 5.7. Pressure drop in well-block (i=1, j=6). For cases 1, 3 and 4, the pressure drop is identical for well-blocks (i=1, j=6,7); and for Case 2, the pressure drop is the same for all well-blocks (i=1, j=3,4,...7).

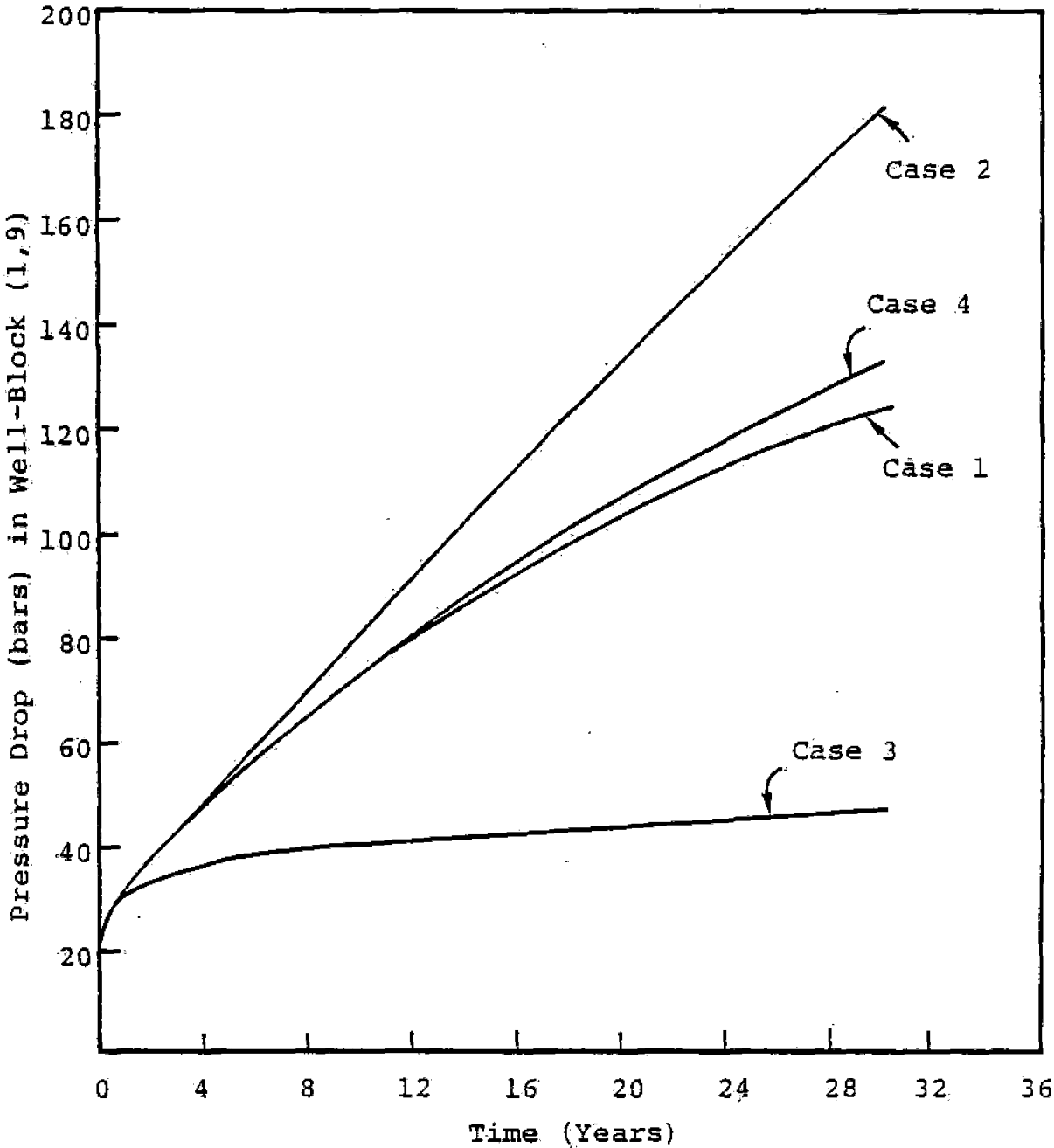

Figure 5.8. Pressure drop in well-block (i=1, j=9). For Cases 1, 3 and 4, the pressure drop is the same in well-blocks (i=1, j=2,4,9). For Case 2, the pressure drop is identical for all well-blocks (i=1, j=3,4,...7).

TABLE 5.7

RESERVOIR COMPACTION AT t = 30.1 YEARS FOR CASE 2

Column (i)	Δh (cm)
1	115.1
2	111.1
3	108.9
4	106.8
5	104.6
6	102.5
7	100.3
8	98.3
9	96.6
10	95.4

TABLE 5.8

PRESSURE DROP (BARS) IN WELL-BLOCKS (i = 1, j) FOR CASE 3

Time (Years)	2	4	6	7	8
0.003125	8.25	8.23	8.25	8.24	8.23
0.1	21.55	21.54	21.61	21.61	21.52
0.6	28.21	28.20	28.68	28.66	28.18
1.1	30.57	30.50	31.45	31.44	30.52
2.1	33.51	33.59	35.59	35.58	33.47
3.1	35.48	35.56	38.95	38.94	35.58
4.1	36.90	37.09	41.69	41.68	36.86
5.1	37.90	38.06	44.06	44.05	37.85
6.1	38.60	38.86	45.94	45.94	38.65
7.1	39.18	39.49	47.68	47.67	39.26
8.1	39.57	40.13	49.07	49.06	39.72
9.1	39.99	40.68	50.26	50.25	40.10
10.1	40.39	41.02	51.32	51.31	40.59
11.1	40.80	41.51	52.34	52.33	40.95
12.1	40.96	41.92	53.23	53.22	41.31
13.1	41.22	42.46	54.09	54.07	41.61
14.1	41.67	42.83	54.72	54.71	42.03
15.1	41.91	43.22	55.42	55.41	42.35
16.1	42.13	43.64	56.07	56.06	42.69
17.1	42.45	43.98	56.70	56.69	42.96
18.1	42.65	44.45	57.27	57.26	43.29
19.1	42.80	44.79	57.84	57.83	43.63
20.1	43.15	45.23	58.41	58.40	43.99
21.1	43.43	45.68	58.92	58.92	44.36
22.1	43.78	46.02	59.45	59.44	44.67
23.1	44.05	46.54	59.97	59.96	44.98
24.1	44.32	46.93	60.46	60.45	45.27
25.1	44.50	47.33	60.93	60.92	45.62
26.1	44.81	47.64	61.46	61.46	46.02
27.1	45.08	48.12	61.95	61.94	46.33
28.1	45.34	48.51	62.41	62.41	46.71
29.1	45.58	48.90	62.89	62.88	46.98
30.1	45.93	49.32	63.36	63.35	47.33

(Maximum gas saturation at t = 30.1 years is 0.011.)

TABLE 5.9

RESERVOIR COMPACTION AT t = 30.1 YEARS FOR CASE 3

Column (i)	Δh (cm)
1	249.5
2	218.8
3	202.0
4	185.4
5	168.7
6	152.4
7	136.6
8	121.9
9	109.2
10	100.7

pressure drops and the formation compaction are given in Tables 5.10 and 5.11, respectively. The reduction in shale compressibility results in somewhat larger pressure drops in the well-blocks (Figures 5.7 and 5.8); this effect, however, becomes evident only for large production times (> 10-12 years).

In summary, the parametric runs discussed here strongly suggest that for sandstone thicknesses greater than 50 feet, the effect of shale influx will not be felt for production times less than one to two years. As far as well tests are concerned, this implies that shale influx can be ignored for practical drawdown/buildup times. For large production periods, however, the influx from shales will play an important role in determining the pressure drop in the sandstone reservoir, and also in the associated formation compaction.

5.3 PRELIMINARY SUBSIDENCE CALCULATIONS

5.3.1 Physical System

Gustavson and Kreitler [1976] have discussed the environmental concerns associated with the production of geothermal fluids from the Texas Gulf Coast reservoirs. According to these authors, production of geothermal water from geopressured zones has potential for causing land subsidence and for activating surface faults. Geopressured zones along the Texas Gulf Coast generally contain sandstones/mudstones with abnormally high porosities. Production of geothermal fluids (and consequent depressurization of sandstones and mudstones) will invariably result in a subsequent decrease in porosity and, hence, subsidence. The Texas Gulf Coast region contains numerous growth faults; and it is likely that most geothermal reservoirs will be located between major growth faults which may act as permeability barriers. The pressure drop (and, hence, compaction of the sediments) will be confined to the

TABLE 5.10

PRESSURE DROP (BARS) IN WELL-BLOCKS (i = 1, j) FOR CASE 4

Time (Years)	2	4	6	7	9
0.003125	8.25	8.24	8.25	8.24	8.23
0.1	21.67	21.69	21.68	21.68	21.67
0.6	29.09	29.07	29.14	29.11	29.05
1.1	32.31	32.26	32.39	32.38	32.29
2.1	37.73	37.66	38.04	38.04	37.69
3.1	42.83	42.87	43.46	43.46	42.71
4.1	47.77	47.87	48.80	48.79	47.65
5.1	52.55	52.49	54.03	54.02	52.45
6.1	57.07	57.12	59.11	59.10	56.98
7.1	61.49	61.49	64.12	64.11	61.39
8.1	64.64	65.81	69.09	69.07	65.69
9.1	69.71	69.85	73.92	73.90	69.63
10.1	73.71	73.91	78.65	78.64	73.64
11.1	77.53	77.81	83.40	83.39	77.46
12.1	81.21	81.53	87.96	87.95	81.09
13.1	84.78	85.17	92.52	92.51	84.72
14.1	88.17	88.67	96.97	96.95	88.20
15.1	91.57	92.25	101.29	101.28	91.56
16.1	94.75	95.50	105.63	105.62	94.78
17.1	97.90	98.80	109.84	109.83	97.94
18.1	101.02	101.96	114.08	114.08	100.98
19.1	104.04	105.13	118.29	118.28	104.06
20.1	106.90	108.13	122.34	122.33	106.97
21.1	109.81	111.19	126.34	126.33	109.87
22.1	112.54	114.09	130.34	130.33	112.61
23.1	115.24	116.98	134.31	134.30	115.37
24.1	117.89	119.86	138.13	138.12	118.10
25.1	120.44	122.63	141.99	141.97	120.70
26.1	123.00	125.37	145.79	145.78	123.29
27.1	125.50	128.09	149.52	149.51	125.77
28.1	127.97	130.77	153.28	153.27	128.25
29.1	130.36	133.45	156.97	156.95	130.65
30.1	132.72	135.99	160.56	160.55	133.08

(Maximum gas saturation at t = 30.1 years is 0.014.)

TABLE 5.11

RESERVOIR COMPACTION AT t = 30.1 YEARS FOR CASE 4

Column (i)	Δh (cm)
1	124.7
2	118.9
3	115.7
4	112.5
5	109.3
6	106.2
7	103.1
8	100.2
9	97.7
10	95.9

region within fault blocks. Differential compaction of sediments within a fault block may cause fault movement and differential subsidence (see Gustavson and Kreitler [1976] for specific examples of oil/gas reservoirs along the Gulf Coast exhibiting this behavior).

In considering the environmental impact of subsidence and possible fault activation, it is essential to consider (1) the geologic characteristics of the reservoir and the underlying/overlying formations, (2) geographic location of the reservoir and, (3) the present and future land use. White, et al. [1977] have conducted a preliminary study of the environmental questions for the planned geothermal test well in the Brazoria prospect. These authors estimate that the surface subsidence resulting from reservoir sandstones alone (i.e., not including the shale compaction) will range from 9 cm/year during the first two years of fluid production to 6 cm/year during a five year period. Differential subsidence may also result along growth faults known to exist near the well site. Significant amounts of subsidence and/or fault activation could seriously affect the following facilities: two petrochemical plants; a small township along Chocolate Bayou; several gas, crude and product pipelines; and paved highways. Surface subsidence may also aggravate the flood hazards.

Bebout, et al. [1976] give a compilation of the regional tertiary cross-sections of the Texas Gulf Coast. The proposed test well lies between control wells 15 and 17 of cross-section W-W' (see Figure 6 of Bebout, et al. [1976]). The Frio formation occurs below a depth of 10,000 feet. As we remarked in Section 5.1, the top of the geopressure is at approximately 10,000 feet below sea level (i.e., coincident with Frio formation). In the geopressure zone, rocks are likely to be competent. Above that depth (say < 10,000 feet) the rocks may be unconsolidated. Subsidence predictions require a knowledge of the stress-strain response behavior of the rock units

constituting the reservoir and the overlying/underlying strata. Unfortunately, such data are not available at the present time. In the subsidence calculations discussed below, we will therefore utilize hypothetical properties for the various rock units. It is almost certain that availability of data from test well cores will require a substantial revision of the assumed stress-strain response behavior (and, consequently, subsidence predictions).

5.3.2 Subsidence Simulators

The basic governing equations for the deformation of a fluid-saturated rock aggregate have previously been discussed by Brownell, et al. [1977]. The momentum balance relation for the fluid-saturated rock aggregate is [Brownell, et al., 1977]:

$$- \nabla \dot{p}_c + \nabla \cdot \dot{\underset{\sim}{S}} + \dot{\rho} \underline{g} = 0 \tag{5.1}$$

where

p_c = composite (rock/fluid) pressure,

$\underset{\approx}{S}$ = deviatoric stress tensor for the rock matrix,

ρ = composite density = $(1-\phi)\rho_r + \phi\rho_f$,

$\rho_r(\rho_f)$ = rock grain (fluid) density,

ϕ = porosity,

and the dot denotes the time-rate of change. Assuming small deformations, we have the following constitutive relations for $\dot{p}_c$ and $\dot{\underset{\sim}{S}}$:

$$\dot{p}_c = \left(1 - \frac{K}{K_s}\right) \dot{p}_f - K \left[\dot{\varepsilon}_r - 3\eta \dot{T}\right] \tag{5.2}$$

$$\dot{\underset{\sim}{S}} = 2\mu \dot{\underset{\sim}{e}} \tag{5.3}$$

where

$K(K_s)$ = instantaneous bulk modulus of porous rock (rock grain)

η = linear thermal expansion coefficient for porous rock

μ = shear modulus of porous rock.

The bulk volumetric strain-rate $\dot{\varepsilon}_r$ and the deviatoric strain-rate tensor $\underset{\approx}{\dot{e}}$ are given by

$$\dot{\varepsilon}_r = v_{i,i}$$

$$\underset{\approx}{\dot{e}} = \frac{1}{2}\,(v_{i,j} + v_{j,i}) - \frac{\dot{\varepsilon}_r}{3}\,\delta_{ij} \tag{5.4}$$

$$v_i = \frac{\partial u_i}{\partial t}$$

u_i = displacement of the rock matrix

The porosity change is governed by the relation:

$$\dot{\phi} = \left[\frac{1}{K_s} - \frac{1-\phi}{K}\right](p_c - p_f)^{\cdot} + 3\,(1-\phi)(\eta-\eta_s)\,\dot{T} \tag{5.5}$$

where η_s denotes the linear thermal expansion coefficient of the rock grain.

We note that K - the bulk modulus of the porous rock - depends upon $(p_c - p_f)$, the loading direction (i.e., increase or decrease in $(p_c - p_f)$ and the past stress history. This dependence of K on the loading direction and history is responsible for the hysteretic effects observed in ground subsidence/uplift due to change in subsurface pore pressure. In many instances it is either not possible to measure K and μ separately or it is sufficient to consider the reservoir compaction to be

primarily uniaxial (the latter assumption is usually invoked in reservoir engineering calculations; see, e.g., Garg, et al. [1977]). The uniaxial compaction coefficient C_m is related to K and μ through the relation:

$$C_m = \frac{1}{(K + \frac{4}{3}\mu)} \tag{5.6}$$

The system of Eqs. (5.1) through (5.4) can be used to describe the stress-strain response of both the reservoir and the surrounding rocks (overburden/underburden). The overburden/underburden rocks are usually represented by linear (or nonlinear) elastic material models and the pore pressure (in case these formations are fluid-saturated) is not explicitly considered. Putting $p_f \equiv 0$ in Eqs. (5.1) through (5.4), we obtain the governing equations for a homogeneous nonlinear elastic material.

In order to model the effect of time-varying fluid flow on matrix stress in a geothermal reservoir, and also to monitor surface subsidence and horizontal deformations, a finite element solid equilibrium code, STAGR (STatic Analysis of Geothermal Reservoirs) has been developed to solve the system of Eqs. (5.1) through (5.5) [Pritchett, et al., 1975]. Like any such finite element code, it is basically a program for solving the problem of a loaded linear elastic continuum; however, problems requiring treatment of nonlinear material behavior may be solved by iteration, using effective elastic moduli ("tangent" or "secant" moduli) in the element. In addition to the usual features found in finite element continuum codes, STAGR can solve problems involving nonsymmetric stress-strain relations. Given fluid pressure history in the reservoir, STAGR may be employed to yield the time varying stress field and the deformation (both vertical and horizontal) in the matrix. STAGR can also be used to model the overburden.

An interactive code AGRESS (Active Geothermal REServoir Simulator) has also been developed which couples the fluid response code MUSHRM (incorporating the one-dimensional consolidated theory) with the rock response code STAGR [Pritchett, et al., 1976]. In AGRESS, the system is marched through any desired number of time steps as follows: in each time step, a MUSHRM cycle calculation is performed yielding values of pore pressure, temperature and fluid density at the end of the time step. This information is then used in the STAGR calculation to yield the instantaneous equilibrium condition (i.e., rock displacements, stress, etc.) as functions of rock properties and fluid variables.

5.3.3 Numerical Results

In this section, we will present some preliminary subsidence predictions for the planned geopressured test well site. We will assume that the formation properties, initial fluid state, and the production history are identical with those of the base case discussed in Section 5.2. In addition to the formation properties given earlier, we require the bulk and the shear moduli of the porous rock, the bulk modulus of the rock grain, and the linear coefficients of thermal expansion for the rock grain and the porous rock. The assumed values for these properties are given in Table 5.12. Since we are only concerned with drawdown (i.e., the production phase of the reservoir during which pore pressure declines monotonically), it is only necessary to define K for $(p_c - p_f)^{\cdot} > 0$ (Table 5.12). Furthermore, in the absence of data from core-analysis (and also in conformity with constant compressibility value assumed in Section 5.2) we will assume K to be a constant - independent of $(p_c - p_f)$ and loading history.

The reservoir along with the overburden/underburden is shown in Figure 5.9. We shall assume the overburden/underburden rocks to be linearly elastic. Region I of Figure 5.9

TABLE 5.12

PARAMETERS ASSUMED FOR THE RESERVOIR ROCKS IN SUBSIDENCE CALCULATIONS

	Sandstone	Shale
Bulk modulus of porous rock K	9.1954 kb**	0.45977 kb**
Shear modulus of porous rock μ	3.44828 kb	0.172414 kb
Coefficient of linear thermal expansion of porous rock η	0 cm/cm°C	0 cm/cm°C
Uniaxial compaction coefficient $C_m = (K + 4/3\mu)^{-1}$	0.725 10^{-10} cm^2/dynes*	14.5 10^{-10} cm^2/dynes*
Bulk modulus of rock grain K_s	300 kb	100 kb
Coefficient of linear thermal expansion of rock grain η_s	0 cm/cm°C	0 cm/cm°C

* Values for C_m are identical with those for compressibility in Table 5.1

** Valid for $(p_c - p_f)^{\cdot} > 0$

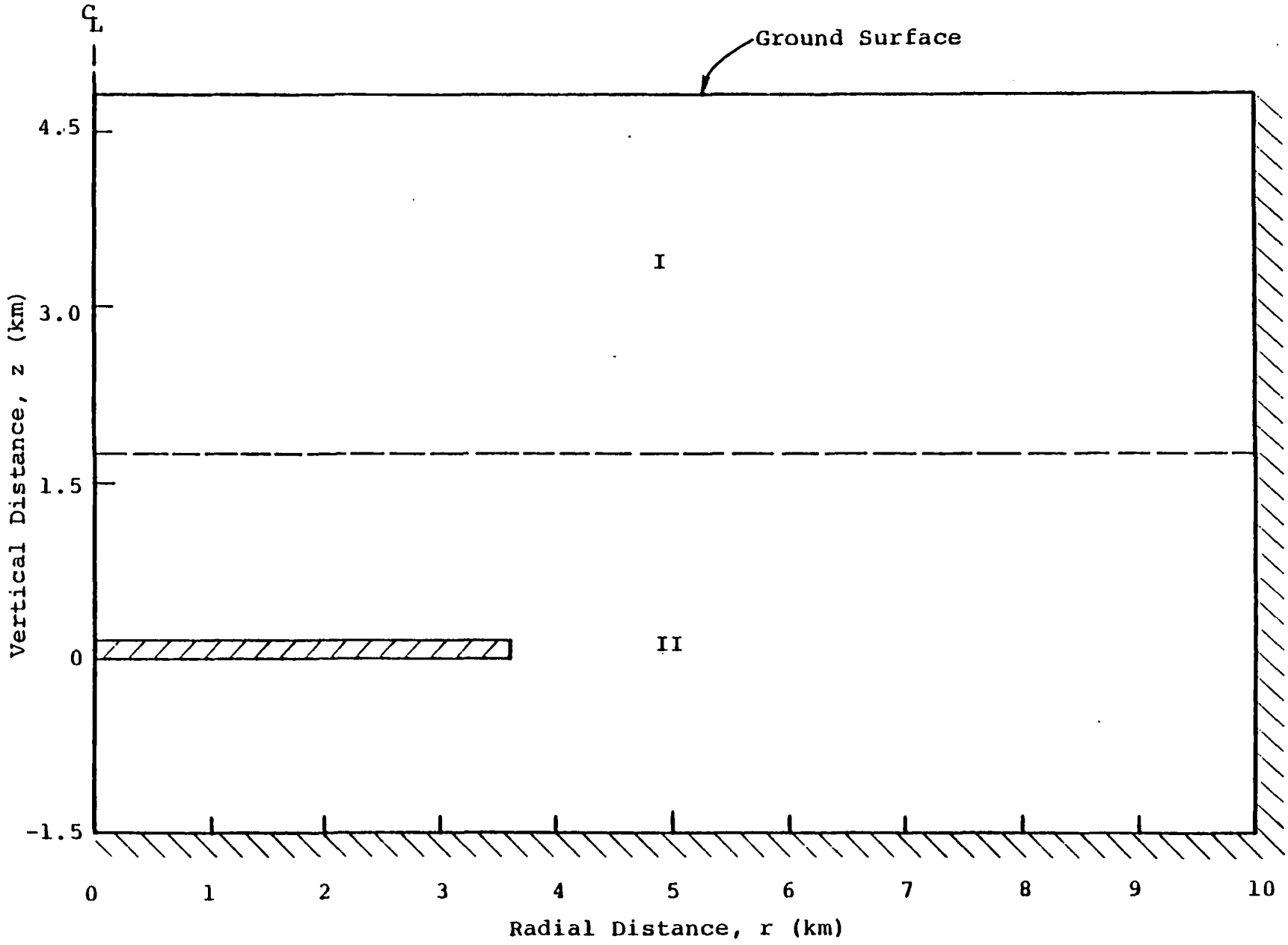

Figure 5.9. Reservoir (hatched) and the overburden/underburden rocks. Region I extends from surface to 10,000 feet depth. Region II lies below 10,000 feet. Both the bottom and the right vertical (i.e., r = 10 km) boundaries are assumed to be fixed.

extends from the ground surface to a depth of 10,000 feet, and is believed to contain unconsolidated rocks. The region below 10,000 feet (Region II in Figure 5.10) contains consolidated sandstones/mudstones. Since actual rock properties are presently unavailable, it was decided to do a series of three parametric runs to assess the effects of variations in rock properties on subsidence. The assumed properties for the three cases are listed in Table 5.13. All of the three AGRESS runs use the MUSHRM calculation for the base case (Case 1) representation of the Austin-Bayou prospect reservoir.

The surface vertical and horizontal movements predicted by the AGRESS simulator at $t \sim 30.282$ years (i.e., corresponding to the end of the Case 1 reservoir production calculation discussed in Section 5.2) for these three cases are shown in Figures 5.10 and 5.11 respectively. The horizontal movement is directed towards $r = 0$. The combined effect of the vertical and horizontal movements is to form a bowl. The main effect of an increase in rock stiffness is to reduce surface displacements (compare case a with cases b and c in Figures 5.10 and 5.11). Figure 5.10 also shows that only a small fraction of reservoir compaction (see Table 5.4) will appear as surface subsidence; the exact amount of surface subsidence is, of course, determined by the properties of the rocks surrounding the reservoir. For comparison with the earlier work of White, et al. [1977], we show the surface displacement history at $r = 0$ in Figure 5.12; the displacement is a linear function of time as a consequence of the assumptions made in our analysis (i.e., (1) linear elastic overburden/underburden, (2) constant compressibility for the reservoir rocks and, (3) constant mass production rate). Maximum subsidence rates predicted (Figure 5.12) are 0.66-1.42 cm/year. These rates are of the same order but generally lower than the values predicted by White, et al. [1977]. Presumably, the differences between the two predictions are related to the differences

TABLE 5.13

ASSUMED ELASTIC PROPERTIES FOR THE OVERBURDEN/ UNDERBURDEN ROCKS UTILIZED IN A SERIES OF THREE PARAMETRIC RUNS

Case No.	Material Region I		Material Region II	
	Bulk Modulus, kb	Shear Modulus, kb	Bulk Modulus, kb	Shear Modulus, kb
a	25	9.375	25	9.375
b	25	9.375	100	37.5
c	100	37.5	100	37.5

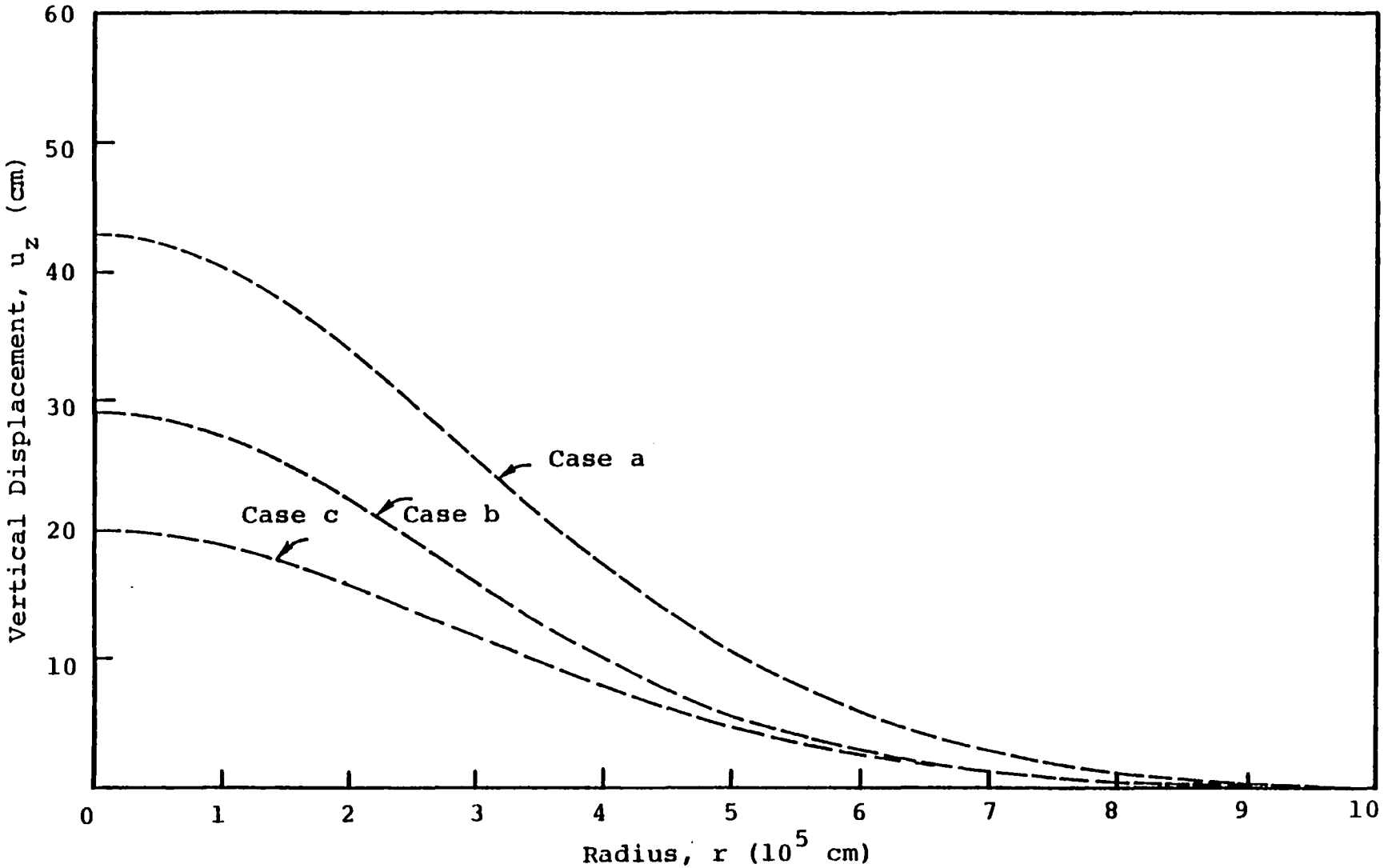

Figure 5.10. Surface vertical displacement at t ≈ 30.282 years.

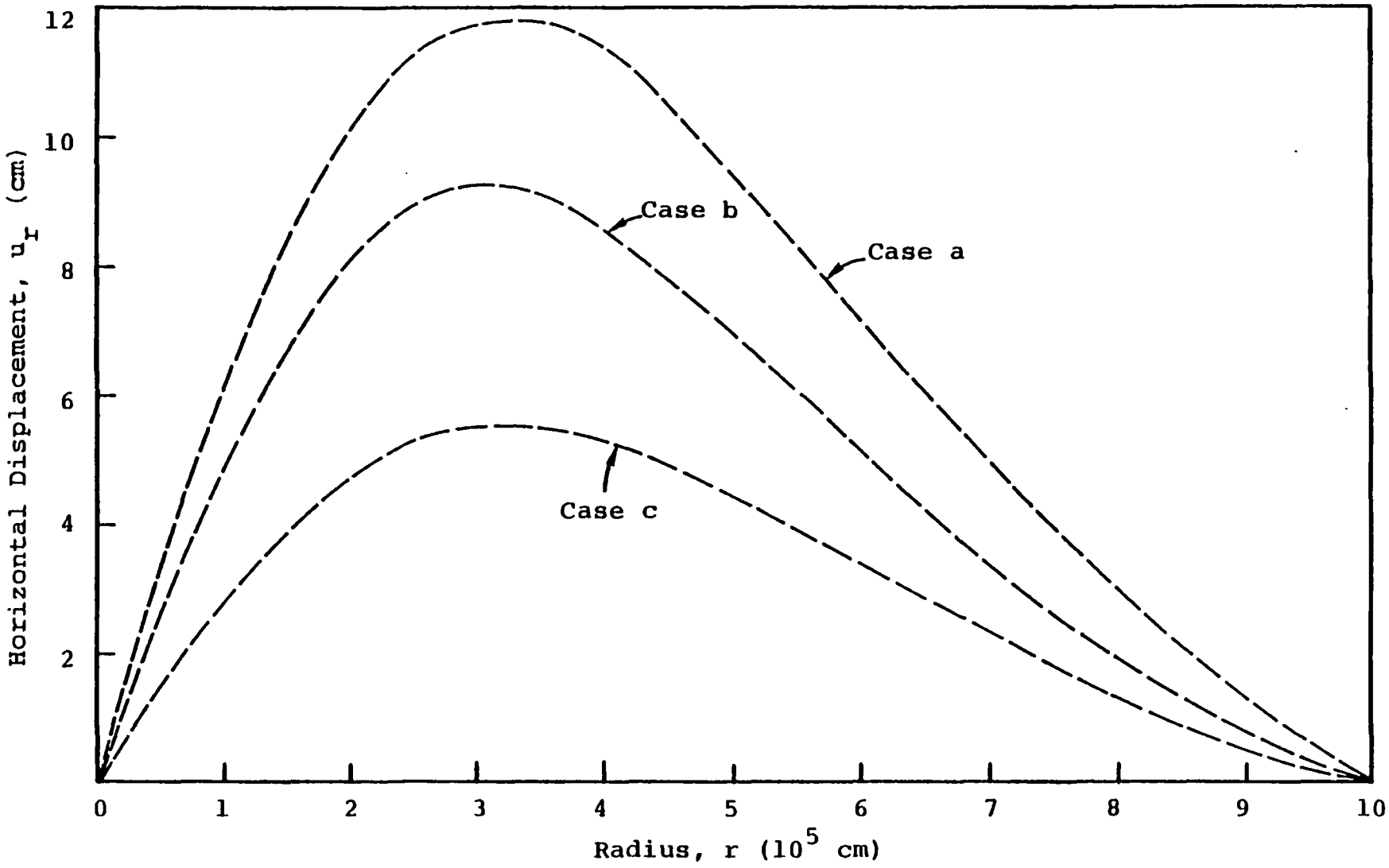

Figure 5.11. Surface horizontal displacement at t ≈ 30.282 years.

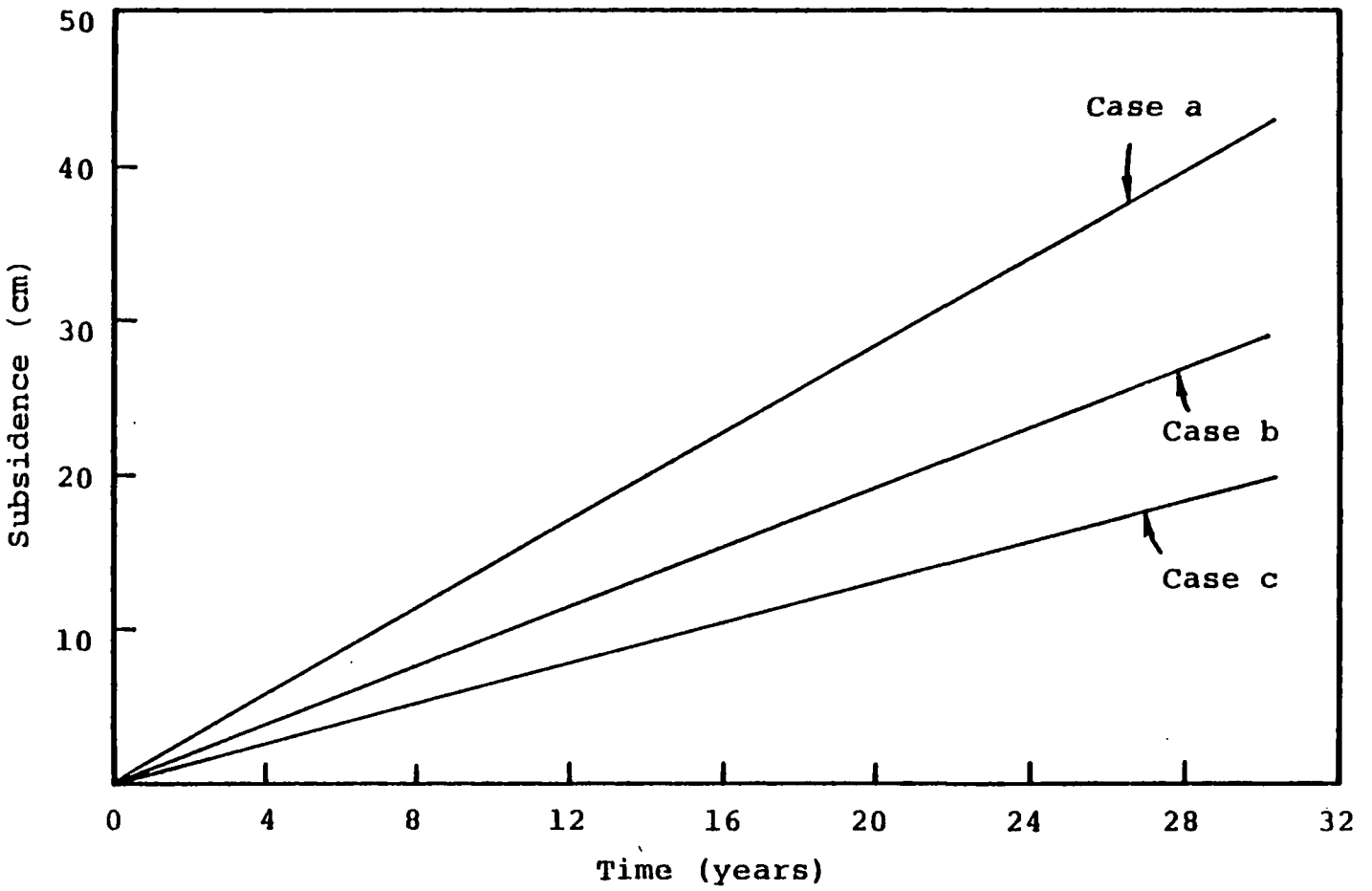

Figure 5.12. Subsidence at r = 0 as a function of time.

between the assumed rock properties and the mass production rate. As the input parameters used by White, et al. [1977] are not available to us, it is not possible to directly compare the two sets of calculations.

The main purpose of this subsection was to present a preliminary estimate of subsidence to be expected at the site of the geopressured test well. In view of the unavailability of data on rock properties and the geologic structure (such as existence of active faults), the present calculations have only a qualitative significance. In particular, we do not expect subsidence to be a linear function of time as implied by the present calculations. Thus, for example, at Wairakei geothermal field (New Zealand), the observed subsidence is a highly nonlinear function of pressure drop (and hence time); the subsidence history implies that over the producing life of the reservoir the formation compressibility C_m has changed by a factor of fifteen [Pritchett, et al., 1976]. The drilling of the test well and analysis of cores obtained from it will hopefully enable us to obtain more realistic rock properties and to refine the subsidence predictions for the Austin-Bayou prospect.

VI. SUMMARY AND FUTURE PLANS

During the first year of this effort, a rather general reservoir simulator (MUSHRM) for treating the important mechanisms in a geopressured geothermal reservoir system was developed and used for preliminary reservoir production/injection calculations. A substantial part of the effort during the second year was concerned with the development of mathematical techniques for dealing with the local two-phase (water with dissolved methane and free methane) flow in a well-block, and for treating two-phase flow in the wellbore. The MUSHRM simulator was employed in its one-dimensional radial configuration to generate a series of drawdown/buildup histories; these simulated histories were used to test the applicability of conventional well-test analysis techniques to geopressured geothermal systems. During the latter part of the second year research effort, a series of axisymmetric calculations were made to make a preliminary assessment of the sensitivity of long-term production behavior of the Brazoria County, Texas prospect to variations in shale distribution, and shale permeability and compressibility. Calculations were also made to demonstrate the land surface movement, both horizontal and vertical (subsidence), that might be associated with fluid production. These preliminary Brazoria County calculations are of necessity based on conjectured reservoir/overburden properties since no actual well-test data were available during this past research period.

A major part of the work planned for a third year of the S^3 effort is the application of the reservoir simulator to the Brazoria County prospect. In cooperation with UTA, a well-testing strategy will be devised; particular emphasis will be placed on the use of multiple flow rates, and the ratio of drawdown/buildup times. The actual well test data from the planned General Crude/DOE 1 Martin Ranch test well

will become available sometime during the later half of 1978. The MUSHRM simulator, along with appropriate mathematical models, will be utilized to history match the observed drawdown/buildup data, and to infer the in situ reservoir properties. It is also planned to employ the in situ reservoir properties and the MUSHRM simulator to estimate the long-term response of the reservoir for selected production/injection strategies. In addition, the potential land surface subsidence associated with alternate production/injection strategies will also be estimated.

A geopressured well may produce from several different sand bodies separated by interbedded shales. It is, therefore, planned to generalize the techniques for treating local two-phase flow within a computational zone, developed during Year 2, to include the treatment of a geopressured well producing from several computational zones. Early during the third year we will modify the equations-of-state for methane/water mixtures to include the effect of salinity on the thermodynamic behavior of the reservoir fluid; the solubility of methane declines with increasing salinity. These modifications of MUSHRM will significantly enhance its usefulness for well-test analysis and for reservoir performance predictions.

REFERENCES

Bebout, D. G., P. E. Luttrell and J. H. Seo [1976], "Regional Tertiary Cross Sections - Texas Gulf Coast," Bureau of Economic Geology, the University of Texas, Austin, Texas, Geological Circular 76-5.

Bebout, D. G., R. G. Loucks and A. R. Gregory [1977], "Study Looks at Gulf Coast Geothermal Potential," Oil and Gas Journal, September 26, 1977. "Texas Geothermal Prospect Slated to Begin Operations at Martin Ranch," Oil and Gas Journal, October 3, 1977.

Brownell, D. H., Jr., S. K. Garg and J. W. Pritchett [1977], "Governing Equations for Geothermal Reservoirs," Water Resources Research, 13, p. 929.

Coury, G. E. [1977], "Production of Geothermal Brine Wells in Two-Phase Flow," Geothermal: State of the Art, Transactions Annual Meeting of the Geothermal Resources Council, San Diego, California, p. 61.

Dukler, A. E., M. Wicks, III and R. G. Cleveland [1964], "Frictional Pressure Drop in Two-Phase Flow: B. An Approach through Similarity Analysis," AIChE Journal, 10, p. 44.

Garg, S. K. and J. W. Pritchett [1977a], "Simulation of Drive Mechanisms in Geopressured Reservoirs," Proceedings 18th U. S. Symposium on Rock Mechanics, Keystone, Colorado, pp. 1B5-1 to 1B5-4.

Garg, S. K. and J. W. Pritchett [1977b], "Two Phase Flow in Geopressured Geothermal Wells," presented at the Third Geopressured Geothermal Energy Conference, University of Southwestern Louisiana, Lafayette, Louisiana, November (published in Energy Conversion, Vol. 18, pp. 45-51, 1978).

Garg, S. K., J. W. Pritchett, M. H. Rice and T. D. Riney [1977], "U.S. Gulf Coast Geopressured Geothermal Reservoir Simulation," Systems, Science and Software, La Jolla, California, Report SSS-R-77-3147.

Gustavson, T. C. and C. W. Kreitler [1976], "Geothermal Resources of the Texas Gulf Coast. Environmental Concerns Arising from the Production and Disposal of Geothermal Waters," Bureau of Economic Geology, the University of Texas, Austin, Texas, Geological Circular 76-7.

Hagedorn, A. R. and K. E. Brown [1964], "The Effect of Liquid Viscosity in Two-Phase Vertical Flow," J. Petroleum Technology, p. 203.

Hagedorn, A. R. and K. E. Brown [1965], "Experimental Study of Pressure Gradients Occurring During Continuous Two-Phase Flow in Small-Diameter Vertical Conduits," J. Petroleum Technology, p. 475.

Hughmark, G. A. [1962], "Holdup in Gas-Liquid Flow," Chemical Engineering Progress, 58, p. 63.

Hughmark, G. A. and B. S. Pressburg [1961], "Holdup and Pressure Drop with Gas-Liquid Flow in a Vertical Pipe," AIChE Journal, 7, p. 677.

Knapp, R. M. and O. F. Isokrari [1976], "Aspects of Numerical Simulation of Future Performance of Geopressured Geothermal Reservoirs," Proceedings Second Geopressured Geothermal Energy Conference, the University of Texas, Austin, Texas, Volume III, p. 101.

Knapp, R. M., O. F. Isokrari, S. K. Garg and J. W. Pritchett [1977], "An Analysis of Production from Geopressured Geothermal Aquifers," Society of Petroleum Engineers Preprint No. 6825.

Martin, J. C. [1959], "Simplified Equations of Flow in Gas Drive Reservoirs and the Theoretical Foundations of Multiphase Pressure Buildup Analyses," Trans. AIME, 216, p. 309.

Matthews, C. S. and D. G. Russell [1967], Pressure Buildup and Flow Tests in Wells, Society of Petroleum Engineers Monograph Volume I, Dallas, Texas.

Orkiszewski, J. [1967], "Predicting Two-Phase Pressure Drops in Vertical Pipe," J. Petroleum Technology, p. 829.

Peaceman, D. W. [1977], "Interpretation of Well-Block Pressures in Numerical Reservoir Simulation," Society of Petroleum Engineers Preprint No. 6893.

Pritchett, J. W., S. K. Garg, D. H. Brownell, Jr. and H. B. Levine [1975], "Geohydrological Environmental Effects of Geothermal Power Production, Phase I," Systems, Science and Software, La Jolla, California, Report SSS-R-75-2733.

Pritchett, J. W., S. K. Garg, D. H. Brownell, Jr., L. F. Rice, M. H. Rice and T. D. Riney [1976], "Geohydrological Environmental Effects of Geothermal Power Production, Phase IIA," Systems, Science and Software, La Jolla, California, Report SSS-R-77-2998.

Pritchett, J. W., S. K. Garg and T. D. Riney [1977], "Numerical Simulation of the Effects of Reinjection Upon the Performance of a Geopressured Geothermal Reservoir," Geothermal: State of the Art, Transactions Annual Meeting of the Geothermal Resources Council, San Diego, California, p. 245.

Ramey, H. J., Jr. [1975], "Pressure Transient Analysis for Geothermal Wells," Proceedings Second United Nations Symposium on the Development and Use of Geothermal Resources, San Francisco, California, Vol. 3, pp. 1749-1757.

Ros, N. C. J. [1961], "Simultaneous Flow of Gas and Liquid as Encountered in Well Tubing," J. Petroleum Technology, p. 1037.

Van Poolen, H. K., E. A. Breitenbach and D. H. Thurnau [1968], "Treatment of Individual Wells and Grids in Reservoir Modeling," J. Petroleum Technology, p. 341.

White, W. A., M. McGraw and T. C. Gustavson [1977], "Preliminary Environmental Analysis of a Geopressured Geothermal Test Well in Brazoria County, Texas," presented at the Third Geopressured Geothermal Energy Conference, University of Southwestern Louisiana, Lafayette, Louisiana, November.

APPENDIX A

DETERMINATION OF EFFECTIVE WELL-BLOCK RADII FOR NUMERICAL RESERVOIR SIMULATIONS

A.1 INTRODUCTION

When modeling a reservoir using a numerical simulator, it is usually impractical to employ zones which are comparable in size to the diameter of a well. The effects of wells are normally represented in such simulations by imposing a prescribed fluid mass extraction/injection rate in the computational zone(s) containing the well. The flow induced in the reservoir by the well may thus be determined.

Sometimes, however, it is desired that conditions at the sandface be predicted by numerical reservoir simulations. Strictly speaking, any such predictions will be erroneous owing to the fact that the well itself is not resolved by the computational grid. As a practical matter, however, it is possible to make reasonable estimates. Consider, in particular, the problem of estimating the sandface pressure from the pressure data given by the numerical simulation. The simulator will provide, at each instant of time, the "well-block pressure"; i.e., the discretized pressure characterizing the computational grid zone containing the well. The problem is, then, to determine the sandface pressure if the well-block pressure is known.

We assume that, on the sub-grid scale, pressures will equilibrate much more rapidly than in the reservoir as a whole; we therefore may treat the sub-grid flow as steady flow. For the particular case of single-phase isothermal flow, mass conservation around the well is expressed by:

$$Q = 2\pi r H \phi \rho u \qquad (A.1)$$

where

r = radius from well axis
H = thickness of layer
ϕ = rock porosity

ρ = fluid density

u = fluid velocity (positive outward)

Q = mass injection rate (mass per unit time); negative for a production well.

Invoking Darcy's law for horizontal radial flow,

$$u = - \frac{k}{\phi \mu} \frac{dP}{dr} \tag{A.2}$$

where

k = rock permeability

μ = fluid dynamic viscosity

P = fluid pressure

we may obtain

$$Q = - \frac{2\pi r H k}{\nu} \frac{dP}{dr} \tag{A.3}$$

where

ν = fluid kinematic viscosity.

Equation (A.3) may be solved for the pressure distribution around the well:

$$P = P_0 - \frac{Q\nu}{2\pi k H} \ln (r/r_0) \tag{A.4}$$

Here P_0 is a specified pressure at some distance from the well r_0; the pressure at the sandface is then:

$$P_w = P_0 + \frac{Q\nu}{2\pi k H} \ln (r_0/r_w) \tag{A.5}$$

where r_w denotes the borehole radius. A similar analysis may be performed for more complicated (i.e., multiphase or multicomponent) flows, but the integration of the general steady flow equations requires numerical techniques. The above simple case will suffice for the present discussion.

Now, if P_0 is taken to be the well-block pressure produced by a numerical simulation, the sandface pressure may be determined from Eq. (A.5), providing that the quantity r_0 (hereafter called the "effective well-block radius") can be determined. Clearly, r_0 should be proportional to the size of the computational zone containing the well; thus, as zone size increases, the disparity between the well-block pressure and the true sandface pressure will likewise increase.

Two cases of interest can be distinguished; the radial or axisymmetric case in which the well occupies the axis of symmetry, and the Cartesian or areal case in which the well is considered to reside in the center of one of the zones in the grid (see Figures A.1 and A.2). In the radial case, the quantity which we require is $r_0/\delta r$, where δr is the radial dimension of the zone adjacent to the axis (Δr_1 in Figure A.1). For the Cartesian case, we also desire $r_0/\delta r$, where δr for the Cartesian case will hereafter be defined as:

$$\delta r = [\Delta x_i \Delta y_j/\pi]^{1/2}$$

that is, the radius of a circle of equal area to that of cell i,j which contains the well.

In the past, many authors (see, for example, van Poolen, et al. [1968]; Coats, et al. [1974]) have attempted to estimate the quantity $r_0/\delta r$ by the following heuristic reasoning. Assume that the simulator-generated well-block pressure may be taken to represent the average pressure in the region of the field represented by the well-block. Since, near the well,

$$P = P_w - \frac{Q}{2\pi kH} \ln (r/r_w) \qquad (A.6)$$

(see Eq. (A.4)), the area-averaged pressure between r_w and δr is:

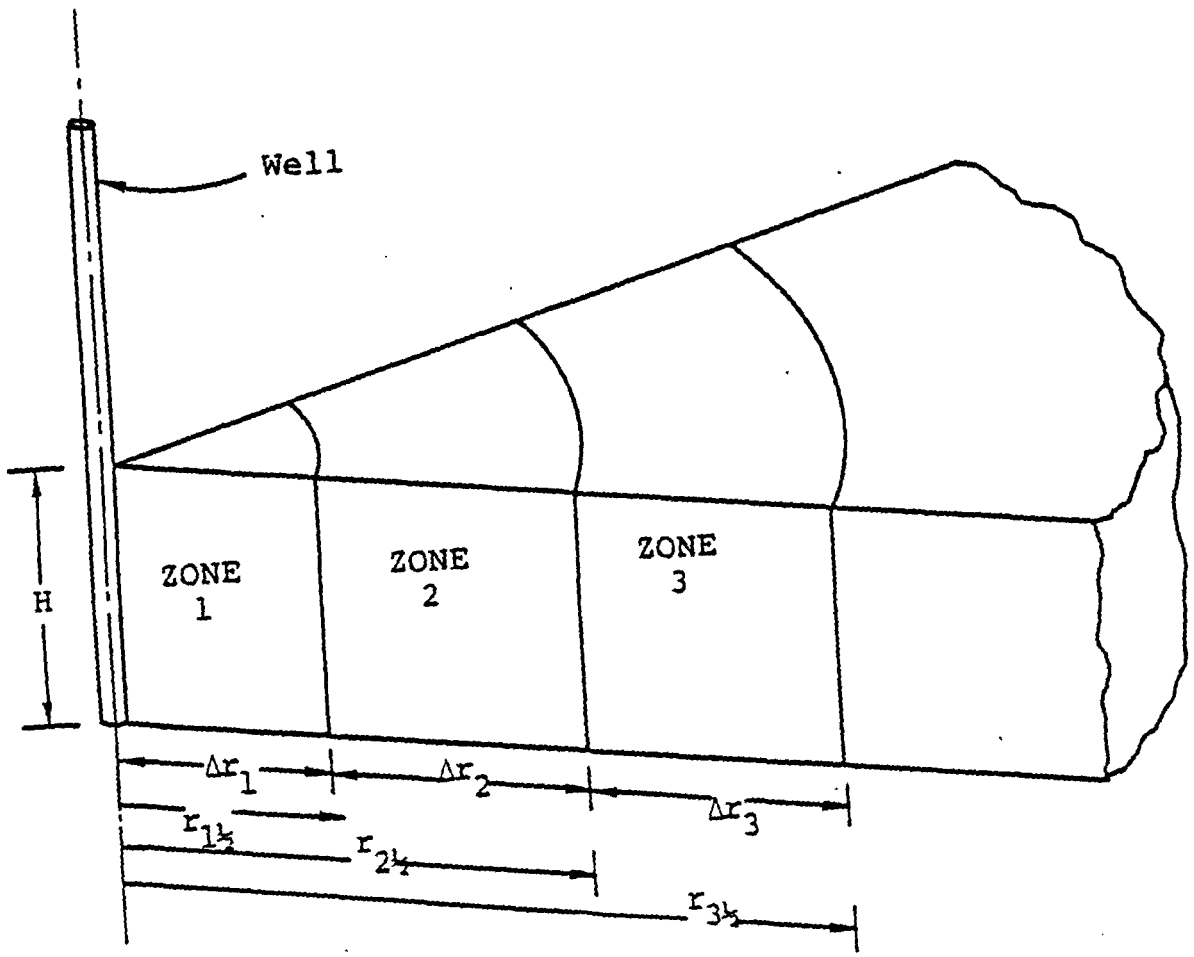

Figure A.1. Computational grid for radial and axisymmetric problems.

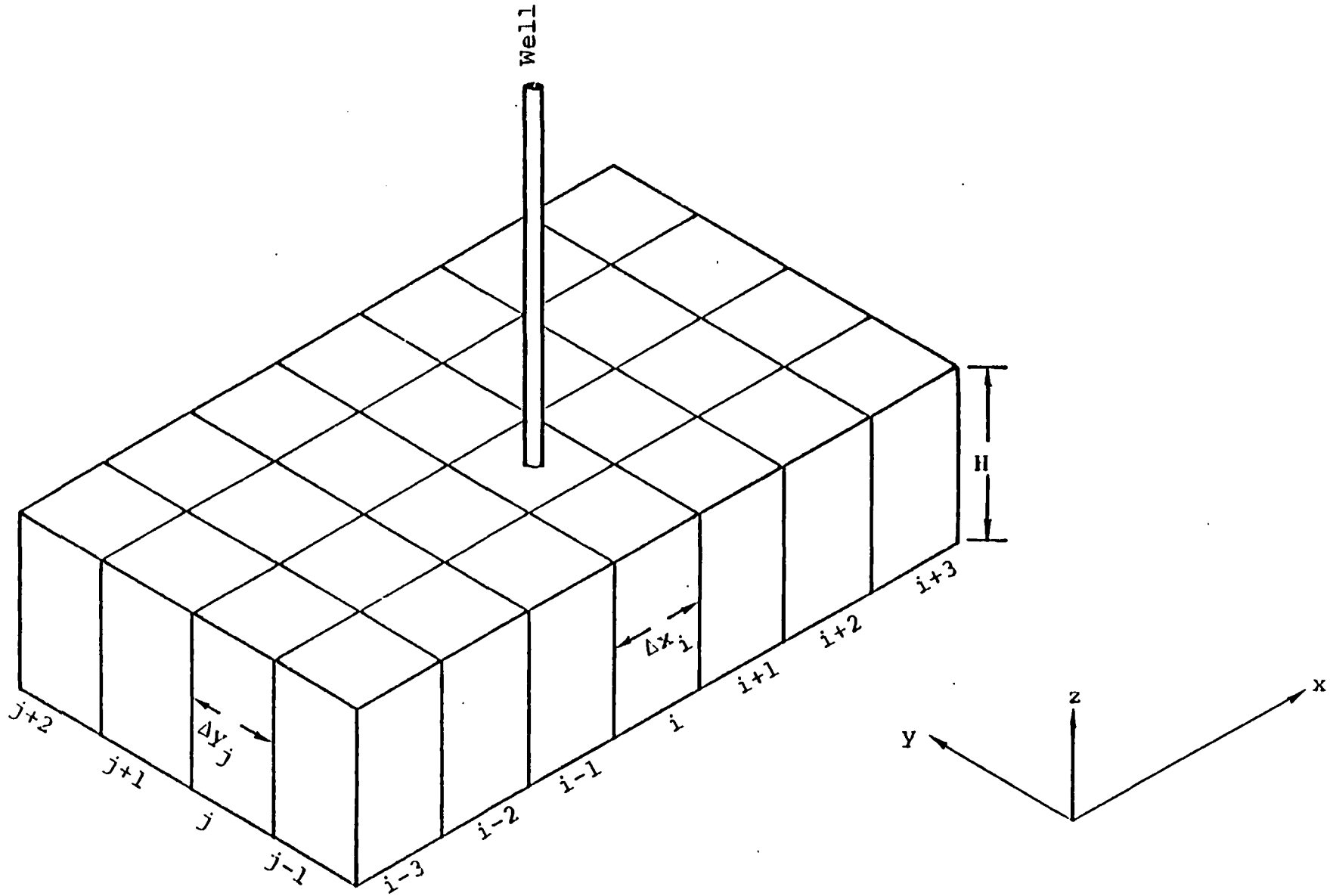

Figure A.2. Computational grid for Cartesian problems.

$$\overline{P} = \int_{r_w}^{\delta r} P\, rdr \Big/ \int_{r_w}^{\delta r} rdr \qquad (A.7)$$

which, since $r_w <<< \delta r$, may be written

$$\overline{P} = P_w - \frac{Q\nu}{2\pi kH}\left[\ell n\left(\frac{\delta r}{r_w}\right) - \frac{1}{2}\right] \qquad (A.8)$$

so that $r_0/\delta r$ is given by substituting (A.8) into (A.6):

$$\frac{r_0}{\delta r} = \exp\left(-\frac{1}{2}\right) = 0.6065 \qquad (A.9)$$

for either Cartesian or axisymmetric geometry.

Recently, Peaceman [1977] presented results for the uniform-grid square-zone Cartesian case which indicated a much smaller value for $r_0/\delta r$; Peaceman's results amount to

$$r_0/\delta r \simeq 0.3513 \qquad (A.10)$$

Instead of merely asserting that the well-block pressure represents a spatially-averaged pressure within the grid block, Peaceman actually solved, numerically, the problem of two-dimensional single-phase flow using grids of various resolutions for the classical steady five-spot injection-production pattern, and then used the numerical well-block pressure obtained to determine the effective value of $r_0/\delta r$ by comparison with the analytic solution for sandface pressure of Muskat [1937] for the five-spot problem.

In the present calculations, the basic method of Peaceman has been employed to determine the appropriate value of $r_0/\delta r$ over a wide range of conditions. The axisymmetric case, which Peaceman did not treat, was first investigated with a uniform radial grid; it was found that the

proper value for $r_0/\delta r$ is quite different in axisymmetric geometry than that for the Cartesian case found by Peaceman. Then, axisymmetric calculations were performed for a non-uniform radial grid, and a first order correction factor for the effect of grid non-uniformity was obtained. Next, the Cartesian case which Peaceman studied was investigated. Three cases were considered; a five-spot pattern with a line from producer to injector lying at 45° to the principal grid lines (i.e., Peaceman's case), a five-spot pattern with a producer-injector line lying parallel to the principal grid lines, and the case of a single well in a circular reservoir with a constant boundary pressure. For well-resolved grids, all three cases produced the same result, which differs from Peaceman's result only in the fourth significant figure. This small difference is a consequence of Peaceman's using only the first two terms in Muskat's analytic solution; we carried the series out to eight terms, which yields ten-place accuracy or better. Finally, in the Cartesian case, the effects of grid non-uniformity and of zone aspect ratio upon $r_0/\delta r$ were investigated, and correction factors to the uniform-square-zone case were determined.

A.2 THE AXISYMMETRIC CASE

Consider a grid such as shown in Figure A.1, containing zones $1 \leq i \leq N$. The radial dimension of zone i is denoted by Δr_i, and the radius of the outer boundary of zone i is $r_{i+\frac{1}{2}}$. The well is located at the axis of symmetry $r_{\frac{1}{2}} = 0$. The finite difference analogue of the mass conservation relation (Eq. (A.3)) may be written as:

$$Q = \frac{4\pi kH}{\nu} \frac{r_{i+\frac{1}{2}}}{\Delta r_i + \Delta r_{i+1}} (P_i - P_{i+1}) = \text{const} \tag{A.11}$$

where P_i is the pressure in zone i. We specify a boundary pressure in the outermost (i=N) zone P_N; P_{N-1} may then be found from (A.11):

$$P_{N-1} = P_N + \frac{\Delta r_{N-1} + \Delta r_N}{r_{N-\frac{1}{2}}} \frac{Q\nu}{4\pi kH} \tag{A.12}$$

Then, given the pressure at i and i+1, the pressure in zone i-1 (P_{i-1}) may be found, for $3 \leq i \leq N-2$, from:

$$P_{i-1} = P_i + \frac{r_{i+\frac{1}{2}}}{r_{i-\frac{1}{2}}} \frac{\Delta r_{i-1} + \Delta r_i}{\Delta r_i + \Delta r_{i+1}} (P_i - P_{i+1}) \tag{A.13}$$

Finally, the pressure in zone i=1 (P_1) may be determined from P_2:

$$P_1 = P_2 + \left(1 + \frac{\Delta r_2}{\Delta r_1}\right) \frac{Q\nu}{4\pi kH} \tag{A.14}$$

The essential question is: where within the various zones i are the pressures generated by the finite difference scheme (A.12)-(A.14) most properly located? If we denote the radius at which P_i should be located by r_i, the analytic solution tells us that:

$$P_i = P_N + \frac{Q\nu}{2\pi kH} \ell n \left(\frac{r_N}{r_i}\right) \tag{A.15}$$

Substituting (A.15) into the finite-difference equations (A.12)-(A.14) gives:

$$r_{N-1} = r_N \exp\left(-\frac{\Delta r_N + \Delta r_{N-1}}{2\, r_{N-\frac{1}{2}}}\right) \tag{A.16}$$

$$r_{i-1} = r_i \left(\frac{r_i}{r_{i+1}}\right)^{G_i} \tag{A.17}$$

where

$$G_i \equiv \frac{r_{i+\frac{1}{2}}}{r_{i-\frac{1}{2}}} \frac{\Delta r_i + \Delta r_{i-1}}{\Delta r_{i+1} + \Delta r_i} \tag{A.18}$$

and

$$r_1 = r_2 \exp\left[-\frac{1}{2}\left(1 + \frac{\Delta r_2}{\Delta r_1}\right)\right] \tag{A.19}$$

We define the boundary pressure P_N to lie at the point

$$r_N = \frac{1}{2}\left(r_{N+\frac{1}{2}} + r_{N-\frac{1}{2}}\right) \tag{A.20}$$

and then the remaining r_i can be determined using Eqs. (A.16)-(A.19). For convenience, we define the variable f_i as:

$$f_i = \frac{r_i - r_{i-\frac{1}{2}}}{\Delta r_i} \tag{A.21}$$

so that Eqs. (A.16)-(A.19) may now be written:

$$f_{N-1} = \frac{1}{\Delta r_{N-1}} \left[\left(\frac{\Delta r_N}{2} + r_{N-\frac{1}{2}} \right) \exp \left(- \frac{\Delta r_N + \Delta r_{N-1}}{2\, r_{N-\frac{1}{2}}} \right) - r_{N-3/2} \right] \quad \text{(A.22)}$$

$$f_{i-1} = \frac{1}{\Delta r_{i-1}} \left[\frac{(f_i \Delta r_i + r_{i-\frac{1}{2}})^{1+G_i}}{(f_{i+1} \Delta r_{i+1} + r_{i+\frac{1}{2}})^{G_i}} - r_{i-3/2} \right] \quad \text{(A.23)}$$

where

$$G_i = \frac{r_{i+\frac{1}{2}}}{r_{i-\frac{1}{2}}} \frac{\Delta r_i + \Delta r_{i-1}}{\Delta r_{i+1} + \Delta r_i} \quad \text{(A.24)}$$

and

$$f_1 = \left(f_2 \frac{\Delta r_2}{\Delta r_1} + 1 \right) \exp \left[- \frac{1}{2} \left(1 + \frac{\Delta r_2}{\Delta r_1} \right) \right] \quad \text{(A.25)}$$

Note that the desired "effective well-block radius" for the zone containing the well (i.e., zone i = 1) is just:

$$\frac{r_0}{\delta r} \equiv f_1 \quad \text{(A.26)}$$

Thus, we desire to find the asymptotic value of f_1 as $N \to \infty$.

In the special case of a uniform grid, i.e.,

$$\Delta r_i = \Delta r = \text{const.} \quad \text{(A.27)}$$

$$r_{i+\frac{1}{2}} = i \Delta r \quad \text{(A.28)}$$

Eqs. (A.22)-(A.25) become:

$$f_{N-1} = \left(N - \frac{1}{2} \right) \exp \left(- \frac{1}{N-1} \right) - (N-2) \quad \text{(A.29)}$$

$$f_{i-1} = \frac{(f_i+i-1)^{1+G_i}}{(f_{i+1}+i)^{G_i}} - (i-2) \qquad (A.30)$$

$$G_i = \frac{i}{i-1} \qquad (A.31)$$

$$f_1 = (1 + f_2)/e \qquad (A.32)$$

These equations may be solved in double precision on a computer; values of f_i for the first few zones obtained in this way for various values of N are listed in Table A.1. Clearly, as N increases, f_1 approaches an asymptotic value; hence, we assert, for axisymmetric or radial geometry with a uniform grid,

$$\frac{r_0}{\delta r} = 0.5615 \qquad (A.33)$$

The general problem of finding $r_0/\delta r$ for a non-uniform grid amounts to an N parameter problem, since the various zone dimensions Δr_i may each be individually specified. We note from Table A.1, however, that by far the greatest change in the value of f occurs between zone 1 and zone 2. This strongly suggests that the most important parameter in the non-uniform grid case is the ratio of Δr_1 to Δr_2, with the more distant zone sizes playing a lesser role. Accordingly, we next consider the case:

$$\Delta r_1 = \Delta r \qquad (A.34)$$

$$\Delta r_i = \eta \Delta r \quad \text{for} \quad 2 \leq i \leq N \qquad (A.35)$$

where η is some specified positive constant. Equations (A.22)-(A.25) become, for this case,

TABLE A.1

AXISYMMETRIC CASE -- VALUES OF f_i FOR VARIOUS VALUES OF N

N	f_1	f_2	f_3	f_4
1	0.50000	--	--	--
2	0.55182	0.50000	--	--
3	0.55783	0.51633	0.50000	--
4	0.55958	0.52109	0.50786	0.50000
5	0.56032	0.52309	0.51116	0.50460
10	0.56120	0.52550	0.51513	0.51014
20	0.56140	0.52604	0.51601	0.51138
50	0.56145	0.52618	0.51624	0.51170
100	0.56146	0.52620	0.51628	0.51175

$$f_{N-1} = \left(N - \frac{3}{2} + \frac{1}{\eta}\right) \exp\left(-\frac{\eta}{1+(N-2)\eta}\right) - \left(N - 3 + \frac{1}{\eta}\right) \qquad (A.36)$$

$$f_{i=1} = \frac{\left(f_i + i + \frac{1}{\eta} - 2\right)^{1+G_i}}{\left(f_{i+1} + i + \frac{1}{\eta} - 1\right)^{G_i}} - \left(i + \frac{1}{\eta} - 3\right) \qquad (A.37)$$

$$G_i = \frac{1 + (i-1)\eta}{1 + (i-2)\eta} \qquad (A.38)$$

$$f_1 = (\eta f_2 + 1) \exp\left(-\frac{1+\eta}{2}\right)$$

This problem has also been solved using the computer, choosing N = 100, for various values of η; the results are listed in Table A.2. As the table shows, as η increases, f_1 decreases; $\eta = 1$ corresponds to the uniform grid case. This data has been fit with the analytic function

$$\frac{r_0}{\delta r}(\eta) = [1 + \eta(0.526199 + 0.0159092 \ln \eta)] \exp\left(-\frac{1+\eta}{2}\right) \qquad (A.39)$$

which fits the data in Table A.2 within 0.007 percent for $0.8 \leq \eta \leq 2$, and is better than 2 percent for all the entries.

TABLE A.2

AXISYMMETRIC CASE -- THE EFFECT OF GRID NON-UNIFORMITY UPON THE EFFECTIVE WELL-BLOCK RADIUS

($\eta \equiv \Delta r_2/\Delta r_1$)

η	$r_0/\delta r$	η	$r_0/\delta r$
0.0	0.606531	1.8	0.484308
0.1	0.606024	1.9	0.473623
0.2	0.604518	2.0	0.462843
0.3	0.602035	2.2	0.441125
0.4	0.598614	2.4	0.419385
0.5	0.594302	2.6	0.397814
0.6	0.589156	2.8	0.376572
0.7	0.583235	3.0	0.355786
0.8	0.576603	3.5	0.306432
0.9	0.569323	4.0	0.261541
1.0	0.561457	5.0	0.186447
1.1	0.553068	6.0	0.129980
1.2	0.544214	7.0	0.089093
1.3	0.534953	8.0	0.060262
1.4	0.525338	9.0	0.040327
1.5	0.515420	10.0	0.026751
1.6	0.505246	∞	0
1.7	0.494862		

A.3 THE CARTESIAN CASE

In two-dimensional Cartesian geometry, mass conservation for horizontal steady single-phase flow is expressed by:

$$\frac{\partial}{\partial x}\left[\frac{k}{\nu}\frac{\partial P}{\partial x}\right] + \frac{\partial}{\partial y}\left[\frac{k}{\nu}\frac{\partial P}{\partial y}\right] = -\dot{m} \qquad (A.40)$$

where $\dot{m}$ represents the local injection rate in mass per unit volume per unit time. If permeability and kinematic viscosity are constant, we may write:

$$\frac{\partial^2 P}{\partial x^2} + \frac{\partial^2 P}{\partial y^2} = -\frac{\nu}{k}\dot{m} \qquad (A.41)$$

Referred to a Cartesian grid as shown in Figure A.2, the finite-difference analogue of Eq. (A.41) is:

$$\frac{1}{\Delta x_i}\left[\frac{2}{\Delta x_i+\Delta x_{i+1}}(P_{i+1j} - P_{ij}) + \frac{2}{\Delta x_i+\Delta x_{i-1}}(P_{i-1j} - P_{ij})\right]$$

$$+ \frac{1}{\Delta y_j}\left[\frac{2}{\Delta y_j+\Delta y_{j+1}}(P_{ij+1} - P_{ij}) + \frac{2}{\Delta y_j+\Delta y_{j-1}}(P_{ij-1} - P_{ij})\right]$$

$$= -\frac{\nu}{k}\dot{m}_{ij} \qquad (A.42)$$

If a well is present in zone i,j, the value of $\dot{m}_{ij}$ will be:

$$\dot{m}_{ij} = \frac{Q_{ij}}{H\,\Delta x_i\,\Delta y_j} \qquad (A.43)$$

where Q_{ij} is the rate at which the well injects fluid into the system, and H is the thickness of the layer. Combining Eqs. (A.42) and (A.43) yields:

$$\frac{\Delta y_j}{\Delta x_i+\Delta x_{i+1}}(P_{ij} - P_{i+1j}) + \frac{\Delta y_j}{\Delta x_i+\Delta x_{i-1}}(P_{ij} - P_{i-1j})$$

$$+ \frac{\Delta x_i}{\Delta y_j+\Delta y_{j+1}}(P_{ij} - P_{ij+1})$$

$$+ \frac{\Delta x_i}{\Delta y_j+\Delta y_{j-1}}(P_{ij} - P_{ij-1})$$

$$= \frac{\nu Q_{ij}}{2\ kH} \qquad \text{(A.44)}$$

We need consider only two sorts of boundary conditions. We may desire to specify the pressure along a boundary; this involves simply demanding that the zones through which the boundary passes have the desired pressure. To specify a symmetry boundary, we impose reflection conditions. For example, if a vertical symmetry boundary along the centers of zones with i = I is desired, we simply set:

$$P_{I-1j} = P_{I+1j} \qquad \text{(A.45)}$$

for all j. For the special case of a uniform grid of square zones, we set

$$\Delta x_i = \Delta y_j = \Delta x, \text{ a constant} \qquad \text{(A.46)}$$

for all i and j, so that Eq. (A.44) becomes:

$$4\ P_{ij} - P_{i+1j} - P_{i-1j} - P_{ij+1} - P_{ij-1} = \frac{\nu Q_{ij}}{kH} \qquad \text{(A.47)}$$

Consider the infinitely-repeating five-spot pattern of production and injection wells illustrated in Figure A.3. Muskat [1937] has shown that the pressure difference between a production well and an injection well will be given by:

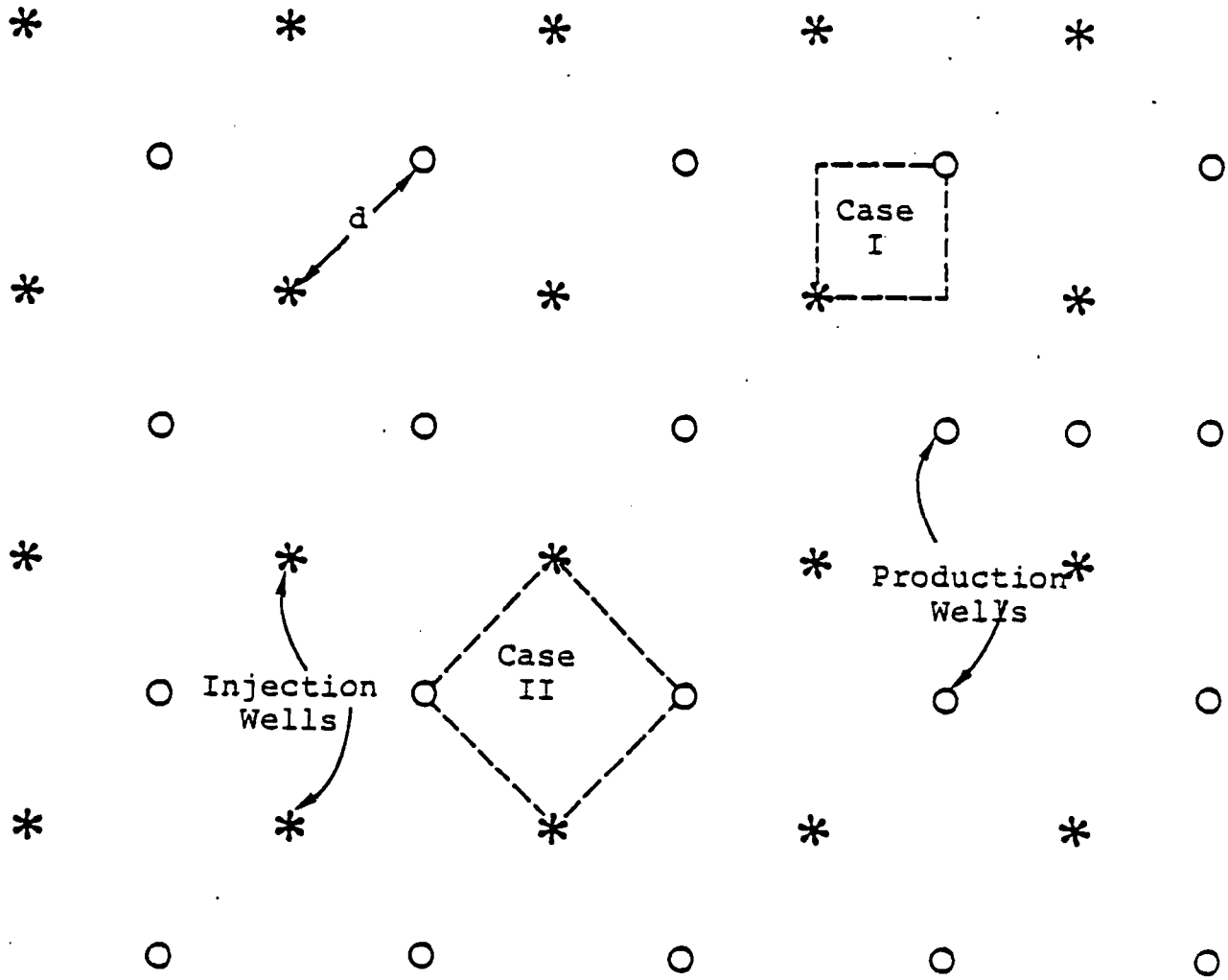

Figure A.3. Five-spot production-injection pattern.

$$\Delta P = \frac{\nu Q}{\pi k H}\left[\ell n\ (d/r_w) - C\right] \tag{A.48}$$

where Q is the mass rate of injection in an injection well (which equals the production rate from a production well), r_w is the well radius (the same for all wells), d is the distance between a production well and an injection well, and C is a universal constant. The value of C must be obtained by summation of a complicated infinite series; Muskat, using the first two terms of the series, obtained

$$C \simeq 0.6190 \tag{A.49}$$

This value was used by Peaceman [1977] in his work. Using a digital computer, evaluting C to any desired precision is straightforward; to ten significant figures

$$C = 0.6172377253 \tag{A.50}$$

This difference is responsible for a slight (fourth significant figure) discrepancy between the value of $r_0/\delta r$ obtained for the five-spot pattern by Peaceman and the results presented here.

The first case we consider is that treated by Peaceman and indicated by "Case I" in Figure A.3. The grid layout is indicated in Figure A.4 for an N by N grid. We set all Q_{ij}'s to zero except as follows:

$$Q_{11} = \frac{kH}{\nu} \text{ (injection well)} \tag{A.51}$$

$$Q_{NN} = -\frac{kH}{\nu} \text{ (production well)} \tag{A.52}$$

We impose symmetry boundaries as follows:

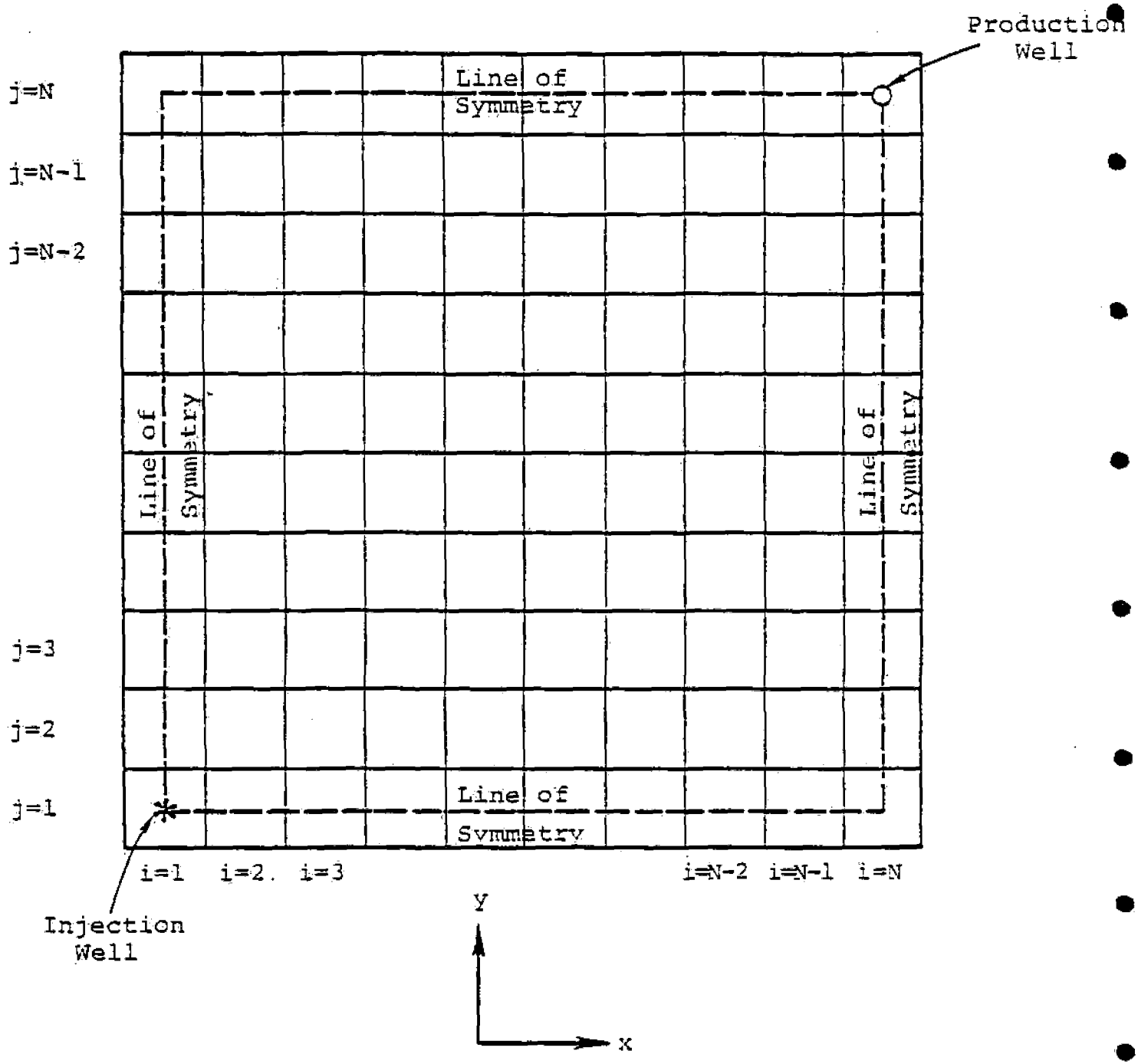

Figure A.4. Grid layout -- Case I.

$$\left.\begin{aligned} P_{0j} &= P_{2j} \\ P_{N+1j} &= P_{N-1j} \end{aligned}\right\} \quad \text{for all } j \quad 1 \leq j \leq N \tag{A.53}$$

$$\left.\begin{aligned} P_{i0} &= P_{i2} \\ P_{iN+1} &= P_{iN-1} \end{aligned}\right\} \quad \text{for all } i \quad 1 \leq i \leq N \tag{A.54}$$

and solve Eq. (A.47) by successive over-relaxation. Now, using Eq. (A.48), if we replace r_w by r_0 (the effective well-block radius), and ΔP by $P_{11} - P_{NN}$, we may determine the value of r_0 from (since $d = \sqrt{2}\ (N-1)\ \Delta x$):

$$\left(\frac{r_0}{\delta r}\right)_{\text{Case I}} = \sqrt{2\pi}\ (N-1)\ \exp\left[-0.6172377253 - \pi\ (P_{11} - P_{00})\right] \tag{A.55}$$

Recall that, for the Cartesian case, δr is defined as

$$\delta r_{ij} = (\Delta x_i\ \Delta y_j/\pi)^{\frac{1}{2}} \tag{A.56}$$

For our second case, we again treat the five-spot pattern, but using a grid oriented 45° to that of Case I; the grid layout for Case II is indicated in Figure A.5. Note that Case II includes four wells; we set

$$Q_{11} = Q_{NN} = \frac{kH}{\nu} \text{ (injection wells)} \tag{A.57}$$

$$Q_{1N} = Q_{N1} = -\frac{kH}{\nu} \text{ (production wells)} \tag{A.58}$$

The symmetry boundary conditions are the same as Case I (i.e., Eqs. (A.53) and (A.54). In Case II, since d is now given by

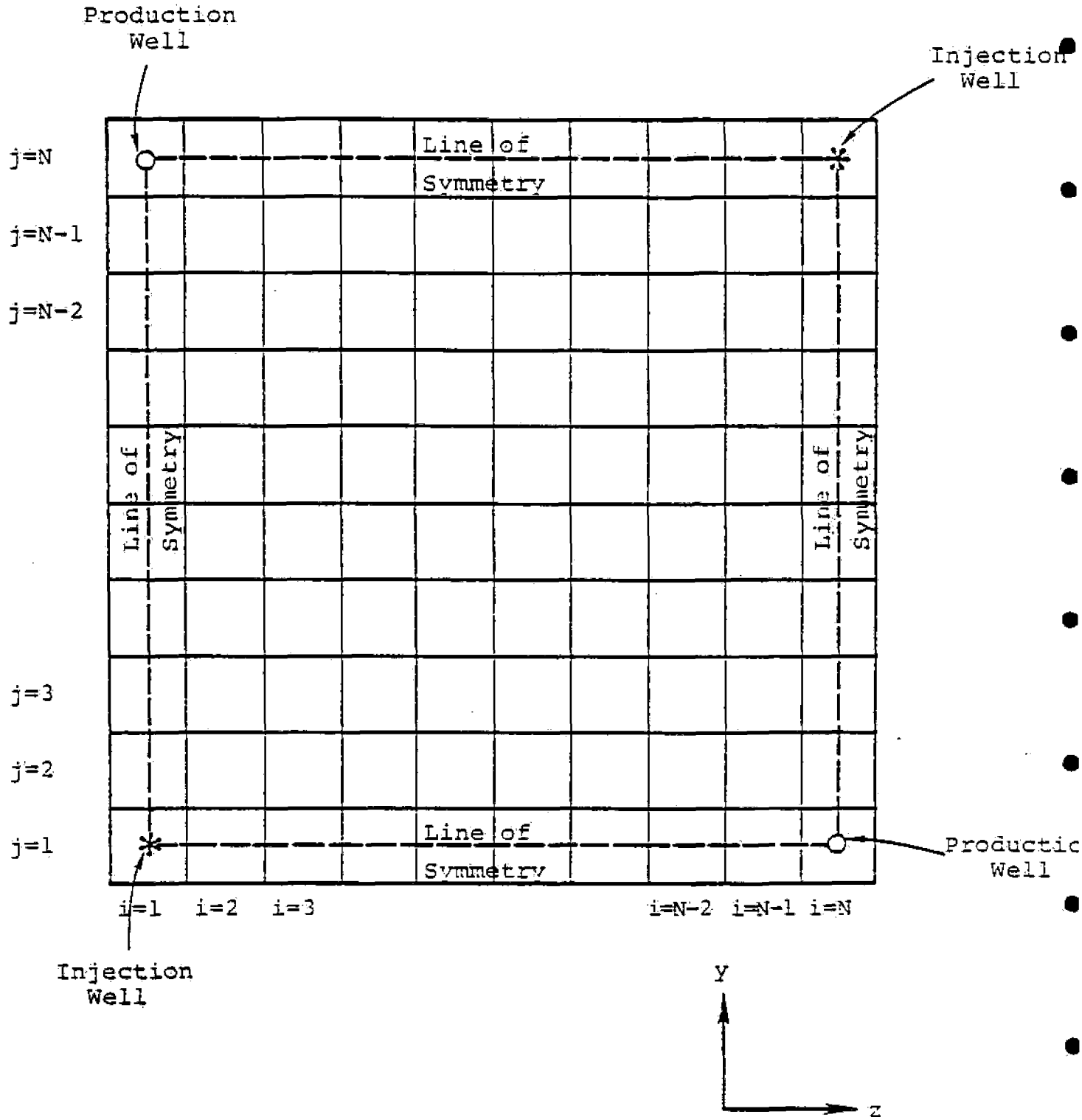

Figure A.5. Grid layout -- Case II.

$$d = (N-1)\ \Delta x$$

we obtain for the effective well-block radius:

$$\left(\frac{r_0}{\delta r}\right)_{\text{Case II}} = \sqrt{\pi}\ (N-1)\ \exp\left[-0.6172377253 - \frac{\pi}{2}\ (P_{11} + P_{NN} - P_{1N} - P_{N1})\right] \qquad (A.59)$$

The third case we will consider is that of a single production well within a circular reservoir with a prescribed boundary pressure. The grid layout for Case III is shown in Figure A.6. As shown earlier, the analytic solution for this problem is:

$$P(x,y) = P_0 - \frac{Q\nu}{2\pi kH}\ \ell n\left[\frac{(x^2 + y^2)^{\frac{1}{2}}}{R_{max}}\right] \qquad (A.60)$$

where the well is at x=0, y=0; R_{max} is the reservoir radius, and P_0 is the boundary pressure. Without loss of generality, we may set our pressure scale such that $P_0 = 0$. In the computational grid, we set $R_{max} = (N-1)\Delta x$, and note that, with the well located in zone i = 1, j = 1, we have

$$x_i = (i-1)\ \Delta x$$
$$y_j = (j-1)\ \Delta x \qquad (A.61)$$

We set the production rate in cell 1,1 by:

$$Q_{11} = -\frac{2\pi kH}{\nu} \qquad (A.62)$$

and impose boundary conditions as follows. Symmetry conditions are maintained along x=0 and y=0 by:

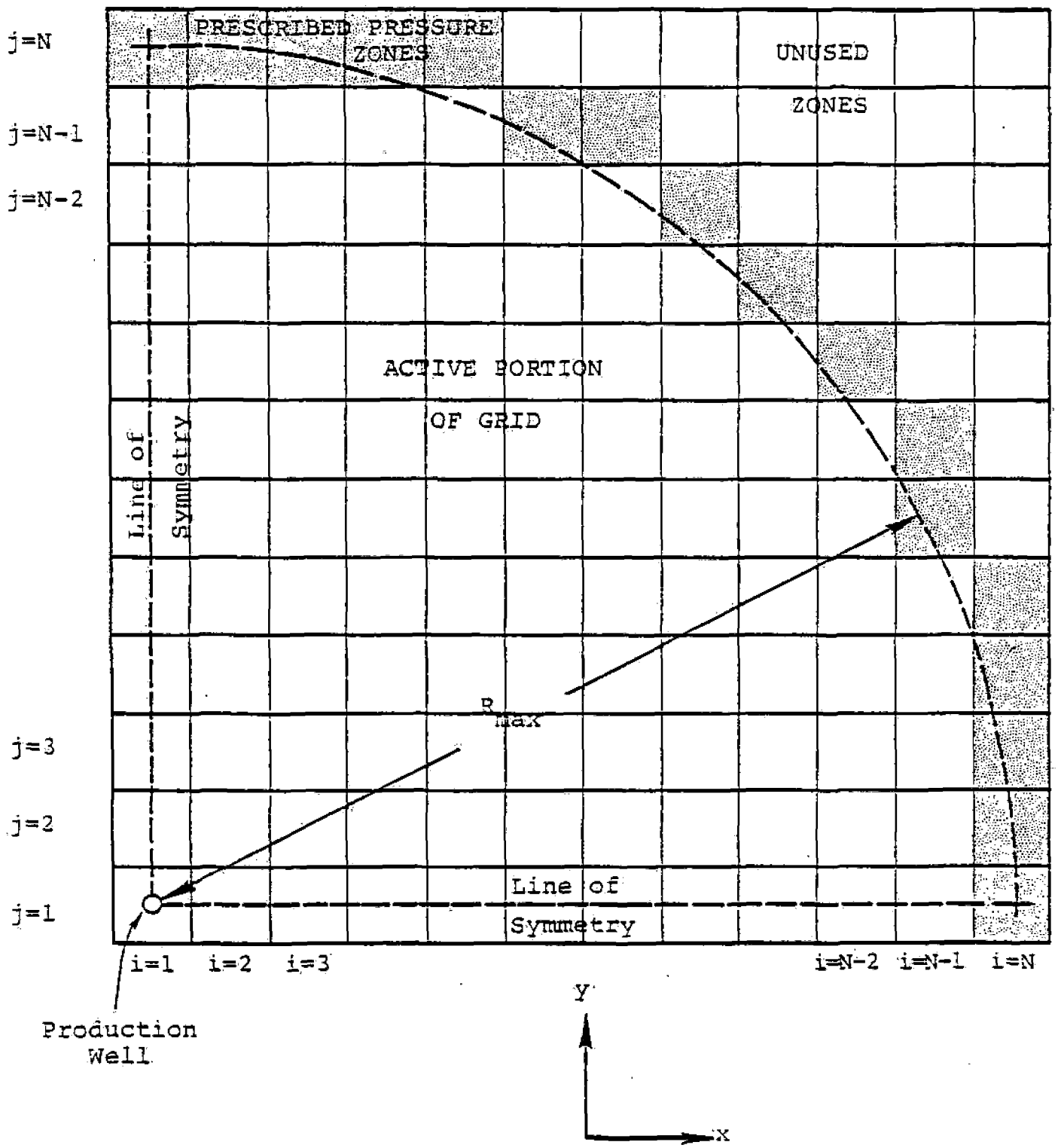

Figure A.6. Grid layout -- Case III.

$$P_{0j} = P_{2j} \quad \text{for all } j \tag{A.63}$$

$$P_{i0} = P_{i2} \quad \text{for all } i \tag{A.64}$$

The outer boundary pressure is maintained by setting and maintaining:

$$P_{ij} = \ell n \left[\frac{(x_i^2 + y_j^2)^{\frac{1}{2}}}{R_{max}} \right] \tag{A.65}$$

in all zones with

$$(i-1)^2 + (j-1)^2 \geq (N-1)^2 \tag{A.66}$$

We then solve Eq. (A.47) for the remaining pressures in the grid. The effective well-block radius for zone i=1, j=1 may then be determined by using Eq. (A.60) to find the radius at which $P = P_{11}$:

$$\left(\frac{r_0}{\delta r}\right)_{\text{Case III}} = \sqrt{\pi}\ (N-1)\ \exp\ (-P_{11}) \tag{A.67}$$

Numerical calculations were carried out for all three cases for various values of N to determine the asymptotic value for $r_0/\delta r$ for each case as N gets very large. The results are listed in Table A.3. Since Case I contains two wells, Case II contains four, and Case III contains only one, Case III reaches its asymptotic value for fairly small N. Case I converges somewhat less rapidly, and Case II is slowest of all. Apart from a slight difference due to Peaceman's use of an inaccurate value of C (see above), the present results for Case I replicate Peaceman's. As Table A.3 shows, all three cases produce the same asymptotic value for $r_0/\delta r$:

TABLE A.3

CARTESIAN CASE -- EFFECTIVE WELL-BLOCK RADIUS AS A FUNCTION OF GRID SIZE

		CASE I		CASE II		CASE III	
N	Number of Zones	$d/\delta r$	$r_0/\delta r$	$d/\delta r$	$r_0/\delta r$	$R_{max}/\delta r$	$r_0/\delta r$
2	4	2.51	0.2811	1.77	0.4359	1.77	0.3685
3	9	5.01	0.3330	3.54	0.3975	3.54	0.3553
4	16	7.52	0.3437	5.32	0.3722	5.32	0.3530
5	25	10.03	0.3473	7.09	0.3625	7.09	0.3522
6	36	12.53	0.3489	8.86	0.3583	8.86	0.3521
7	49	15.04	0.3500	10.63	0.3562	10.63	0.3520
9	81	20.05	0.3508	14.18	0.3543	14.18	0.3519
11	121	25.07	0.3512	17.72	0.3534	17.72	0.3519
13	169	30.08	0.3514	21.27	0.3529	21.27	0.3518
15	225	35.09	0.3515	24.81	0.3527	24.81	0.3518
17	289	40.02	0.3516	28.36	0.3525	28.36	0.3518
19	361	45.12	0.3517	31.90	0.3524	31.90	0.3518
21	441	50.13	0.3517	35.45	0.3523	35.45	0.3518
23	529	55.15	0.3517	38.99	0.3522	38.99	0.3518
25	625	60.16	0.3518	42.54	0.3522	42.54	0.3518
27	729	65.17	0.3518	46.08	0.3521	46.08	0.3518
29	841	70.19	0.3518	49.63	0.3521	49.63	0.3518
31	961	75.20	0.3518	53.17	0.3521	53.17	0.3518
33	1089	80.21	0.3518	56.72	0.3520	56.72	0.3518
35	1225	85.23	0.3518	60.26	0.3520	60.26	0.3518
37	1369	90.24	0.3518	63.81	0.3520	63.81	0.3518

$$\left(\frac{r_0}{\delta r}\right)_{N\to\infty} = 0.3518 \tag{A.68}$$

In the preceeding section on the axisymmetric case, it was observed that the proper value of $r_0/\delta r$ depended to some extent upon $\eta(=\Delta r_2/\Delta r_1)$. It would not be surprising to find an analogous effect in the Cartesian case as well. Furthermore, the effect of zone aspect ratio (i.e., $\Delta x_i/\Delta y_j$) upon $r_0/\delta r$ should be established. To determine these effects, Case III (being the most quickly convergent) was chosen, and a small computer program was written to treat that case with a more general grid, i.e., using Eq. (A.44) instead of Eq. (A.47). The details of this program are straightforward and will not be described in detail.

First, the effect of non-uniform zoning was investigated. If zone i=I, j=J is the zone containing the well, the grid was determined by:

$$\begin{aligned} \Delta x_i &= D_1 \quad \text{for} \quad i = I \\ &= D_2 \quad \text{for} \quad i \neq I \\ \Delta y_j &= D_1 \quad \text{for} \quad j = J \\ &= D_2 \quad \text{for} \quad j \neq J \end{aligned} \tag{A.69}$$

where D_1 and D_2 are constants. For the Cartesian case, the parameter η was defined as:

$$\eta_{ij} = \frac{1}{2}\left\{\left[\frac{(\Delta y_{j+1} + \Delta y_j + \Delta y_{j-1})(\Delta x_{i+1} + \Delta x_i + \Delta x_{i-1})}{\Delta x_i \, \Delta y_j}\right]^{\frac{1}{2}} - 1\right\} \tag{A.70}$$

which is equal to unity for a uniform grid. A number of cases were computed using N = 14, as shown in Table A.4; these results are expressed in terms of the ratio of $r_0/\delta r$ at the particular value of η to that at $\eta = 1$. Also shown is an analytic fit to these results:

$$\frac{r_0}{\delta r}(\eta) = \frac{r_0}{\delta r}(\eta = 1) \times (0.5598 + 0.4402\eta)\exp\left(\frac{3}{4}[1 - \eta]\right) \tag{A.71}$$

As the table shows, the fit is reasonably accurate.

Finally, the effect of the aspect ratio of the zone containing the well upon $r_0/\delta r$ was investigated. The grid was set up as follows:

$$\Delta x_i = \Delta x \quad \text{for all } i$$
$$\Delta y_j = \Delta y \quad \text{for all } j \tag{A.72}$$

where Δx and Δy are specified (and generally unequal) constants. The computed results are listed in Table A.5, along with an analytic fit which is quite accurate for aspect ratios up to four or so:

$$\frac{r_0}{\delta r}(\alpha) = \frac{r_0}{\delta r}(\alpha = 1) \times \sqrt{2}\left\{0.7 + 0.3\exp\left[-1.579\,(\alpha - 1)\exp\left(\frac{1-\alpha}{3.92}\right)\right]\right\} \tag{A.73}$$

where the aspect ratio α is defined by:

$$\alpha_{ij} = \left(\frac{\Delta x_i}{\Delta y_j}, \frac{\Delta y_j}{\Delta x_i}\right)_{max} \tag{A.74}$$

TABLE A.4

CARTESIAN CASE -- EFFECT OF GRID NON-UNIFORMITY ON EFFECTIVE WELL-BLOCK RADIUS

	$\frac{r_0}{\delta r}(\eta)/\frac{r_0}{\delta r}(\eta = 1)$		
η	Numerical Result	Analytic Fit Eq. (A.71)	Difference
0.25	1.167	1.176	-0.009
0.50	1.128	1.135	-0.007
0.80	1.057	1.060	-0.003
1.00	1.000	1.000	0.000
1.25	0.922	0.920	+0.002
1.50	0.840	0.839	+0.001
2.00	0.680	0.680	0.000
3.00	0.414	0.420	-0.006
4.00	0.237	0.245	-0.008
5.00	0.130	0.137	-0.007
7.00	0.036	0.040	-0.004
10.00	0.005	0.006	-0.001

TABLE A.5

THE EFFECT OF ZONE ASPECT RATIO ON EFFECTIVE WELL-BLOCK RADIUS

$$\frac{r_0}{\delta r}(\alpha)/\frac{r_0}{\delta r}(\alpha = 1)$$

α	Grid Size (Zones)	Numerical Calculation	Analytic Fit Eq. (A.73)	Difference
1.1	21 × 23	1.002	1.004	-0.002
1.2	21 × 25	1.008	1.010	-0.002
1.3	21 × 27	1.017	1.019	-0.002
1.4	21 × 29	1.028	1.029	-0.001
1.5	21 × 31	1.041	1.041	0.000
1.75	21 × 36	1.077	1.075	+0.002
2.0	15 × 29	1.118	1.115	+0.003
2.5	15 × 36	1.204	1.201	+0.003
3.0	15 × 43	1.290	1.290	0.000
3.5	15 × 50	1.375	1.379	-0.004
4.0	15 × 57	1.456	1.466	-0.010
4.5	15 × 64	1.535	1.551	-0.016
5.0	15 × 71	1.610	1.634	-0.024
6.0	8 × 43	1.754	1.796	-0.042
7.0	8 × 50	1.887	1.954	-0.067
8.0	8 × 57	2.012	2.113	-0.101
9.0	8 × 64	2.129	2.274	-0.145
10.0	8 × 71	2.240	2.440	-0.200

REFERENCES

Coats, K. H., W. D. George, C. Chu and B. E. Marcum [1974], "Three-Dimensional Simulation of Steam Flooding," Soc. Pet. Eng. J., pp. 573-593, December.

Muskat, M. [1937], The Flow of Homogeneous Fluids Through Porous Media, McGraw-Hill, New York.

Peaceman, D. W. [1977], "Interpretation of Well-Block Pressure in Numerical Reservoir Simulation," SPE Preprint No. 6893.

van Poollen, H. K., H. C. Bixel and J. R. Jargon [1970], "Individual Well Pressures in Reservoir Modeling," Oil and Gas Journal, pp. 78-80, October.